MULTIPHYSICS SIMULATION, ANALYSIS, AND DESIGN OF A

PERMANENT MAGNET EXCITED LIQUID METAL

MAGNETOHYDRODYNAMIC POWER GENERATOR

by

Eva-Marie Cosoroaba

APPROVED BY SUPERVISORY COMMITTEE:

_____

Dr. Babak Fahimi, Chair

_____

Dr. Bilal Akin

_____

Dr. Andrea Fumagalli

_____

Dr. Fatemeh Hassanipour

_____

Dr. Mehrdad Nourani

To my husband and our little family

And

To everyone who puts education before comfort.

MULTIPHYSICS SIMULATION, ANALYSIS, AND DESIGN OF A

PERMANENT MAGNET EXCITED LIQUID METAL

MAGNETOHYDRODYNAMIC POWER GENERATOR

by

EVA-MARIE COSOROABA, BS

DISSERTATION

Presented to the Faculty of

The University of Texas at Dallas

in Partial Fulfillment

of the Requirements

for the Degree of

DOCTOR OF PHILOSOPHY IN

ELECTRICAL ENGINEERING

THE UNIVERSITY OF TEXAS AT DALLAS

December 2017

ACKNOWLEDGMENTS

gave me the confidence to take the next step. Thank you Christine Istrate and Andrea Dumitrescu for not letting me give up in High School and reminding me that I wasn't meant for Philology, even though sometimes I wished I was. Thank you to my Physics teacher Lucian Staroste, who recommended me to study Electrical Engineering when I was completely lost. Look where it got me!

Last, but not least, I would like to thank my family and all of its branches. My deepest gratitude goes out to my "foster family," the Hoque family and Sanjida. You were my haven in this strange new life. I would not have had the strength to venture this far out without you. Thank you to my in-laws Kelly Flint, Susan and Frank Clark. You truly make me feel like a daughter: loved and supported, no matter what. I am much indebted of my parents Gerhild Rudolf and Stefan Cosoroabă, for disregarding gender stereotypes and letting me find my own way. I inherited their love of reading and learning. Both showed me that learning doesn't end with school. I'm proud of you, Mutter, for pursuing your PhD. I know you can do it! Thank you Elisabeth Stanciu, you studied Architecture in Timişoara and paved my way. Thank you Jakob Cosoroabă, you found the internship opportunity at Bosch and reminded me that my education and I always have priority. Thank you Martha Cosoroabă, you are my biggest cheerleader.

Words cannot express how grateful I am to you Adam Clark, my dear husband. Thank you for putting things in perspective and picking up the pieces. Thank you for giving me strength and believing in me when I didn't. Thank you for bringing balance to my life and supporting our little family in every way you possibly can. Thank you, for making coffee at 6 am.

October 2017

MULTIPHYSICS SIMULATION, ANALYSIS, AND DESIGN OF A

PERMANENT MAGNET EXCITED LIQUID METAL

MAGNETIHYDRODYNAMIC POWER GENERATOR

Eva-Marie Cosoroaba, PhD
The University of Texas at Dallas, 2017

Supervising Professor: Dr. Babak Fahimi

Magnetohydrodynamic (MHD) power generation is a method of mechanical to electrical energy conversion, highly researched in the 1960s. Thermal constraints and lack of powerful simulation tools brought advancements in the field to a halt. This dissertation is an attempt to revive MHD, adapting it for renewable energy harvesting and making it thus attractive for inclusion in the energy mix of the near future.

The presented work includes a detailed description of a permanent magnet excited liquid metal (PMLM) MHD generator and its operation, proposing Gallium as the working fluid. Furthermore, multiphysics simulations are used to demonstrate the validity of the analytical derivations of operating characteristics. Experimental measurements of a PMLM MHD generator prototype are provided and used to verify the multiphysics simulation method. A good match between experiments and simulation is observed as well as efficiencies up to 60%, depending on design. Optimal design considerations are included, to demonstrate the feasibility of this mechanical to electrical energy conversion method. Lastly, a case study is presented in which MHD is used for

thermal to electrical energy conversion, harvesting low temperature waste heat. This thermal to electrical energy conversion reaches efficiencies up to 25%, depending on design parameters.

TABLE OF CONTENTS

LIST OF TABLES

LIST OF FIGURES

CHAPTER 1

INTRODUCTION

1.1   Motivation and Objectives

As the demand for renewable energy increases, diversification of these renewable sources becomes imperative to ensure reliability comparable to traditional generation methods. Most renewable energy sources rely on weather patterns and are therefore not ideal and not able to function as standalone solutions. Therefore, a mix is needed to assure the reliability humans have grown accustomed to and which industry needs to sustain.

   With diversification, reliability, and fast reaction time in mind, this work proposes liquid metal (LM) magnetohydrodynamic (MHD) power generation as an additional source to the renewable energy mix of the near future. MHD has been extensively researched in the 1960s and was expected to become a building block of the modern power grid [1], but practical constrains prevented this technology from becoming mainstream. High operating temperatures [2] and at that time costly AC to DC converters [3] are among the reasons research halted. In this work, MHD is resumed and alternative work fluids are considered to improve the older designs, in the hopes of providing a more attractive MHD generator solution.

   An additional reason to resume MHD for power generation is that computer aided simulation has become substantially more powerful since 1960, and the reevaluation of this technology using multiphysics modeling is a possibility. The creation of a customizable model also allows for a sensitivity study to design parameters. Information of parameter impact on generator power output and efficiency is valuable to researchers as well as industry. And lastly, MHD power

generation can be part of a larger system which converts thermal energy to electrical in a renewable and sustainable fashion. When combined with a thermal to mechanical energy converter, MHD has the ability to harvest low temperature waste heat energy from sources such as data centers, HVAC systems, and car and power plant exhaust gases.

Therefore, in accordance to the motivation behind this work described in the previous paragraphs, the following objectives are addressed:

- Study of working fluid and excitation alternatives to provide a low temperature MHD power generation solution, therefore simplifying construction and material constraints.

- Derivation of a mathematical model, to assist the study of the generator.

- Creation of a detailed multiphysics model of the MHD generator, considering electromagnetics, fluid dynamics and heat transfer in a fully coupled interface to provide a realistic simulation tool.

- Study of a LM MHD prototype for validation of the multiphysics modeling process.

- Sensitivity analysis of design parameters in the 3D simulation model and summary of optimal design guidelines to provide a starting point for industrial implementation.

- Proposal of a renewable thermal to electrical energy solution based on LM MHD.

1.2   Brief Introduction to Magnetohydrodynamics in Power Generation

The governing law of a magnetohydrodynamic power generator is Faraday's law of induction. Faraday discovered that a change in magnetic field magnitude with respect to time can induce a voltage into an exposed conductor. Furthermore, it was found that a similar phenomenon of induction occurs when the relative position between the conductor and the field changed over

time. In the case of magnetohydrodynamic power generation, as the name suggests, the conductor is in liquid state. Voltage is thus induced when either the magnetic field to which the fluid is exposed changes over time or the fluid is moving through the field. When the excitation varies but the fluid is not stagnant, a voltage is induced and the generator acts as a transformer. The nature of the MHD generator is therefore that of a mechanical to electrical energy converter only if the fluid is moving. The kinetic energy of the fluid is harvested and used to generate a voltage potential and further an electron flow in the conductor, if the circuit is closed.

From this high level description of the MHD power generation, the main elements can be identified as: the conductive working fluid, the source of magnetic field, electrodes to capture the voltage potential, and lastly, a source of kinetic energy such as a mechanical pump. A mechanical structure, namely a channel, is needed to maintain the fluid contained. Fig. 1.1 depicts a possible ring shaped configuration for the MHD power generator, using liquid metal as the working fluid and permanent magnets as its excitation. Additionally, the cross section of the channel is shown. It is noteworthy that the direction of induced current is always perpendicular to the plane defined by the directions of fluid flow and magnetic excitation. The direction of the current flow depends on the operation of the MHD system, as either a generator (vectors orientation as shown in Fig. 1.1) or a motor, also called accelerator, in which case the current is supplied from an exterior source and the fluid will move.
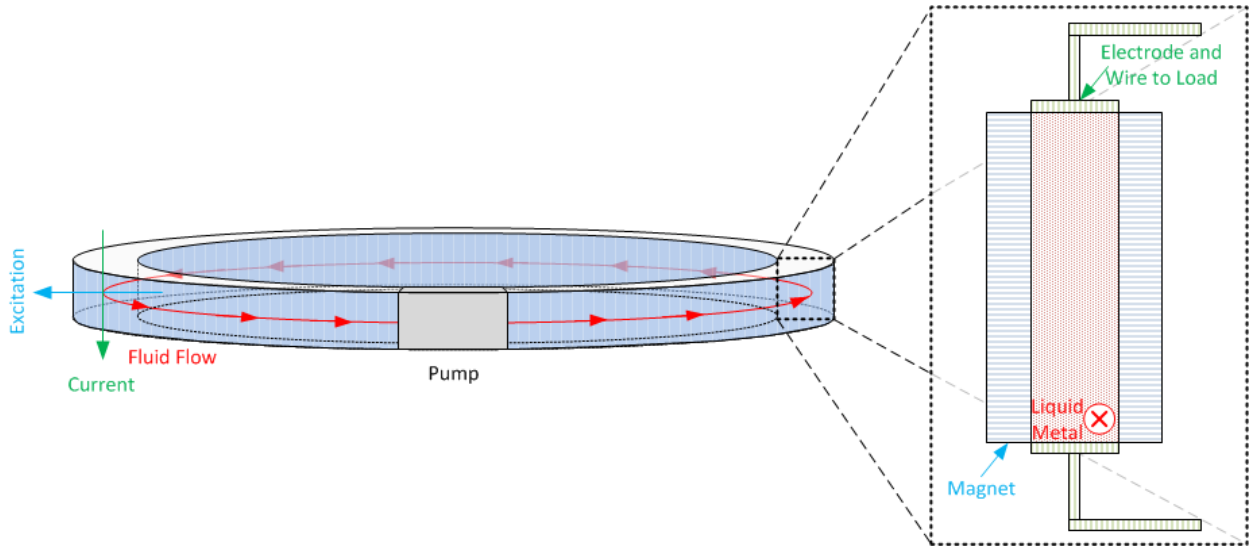
Figure 1.1. Example of a ring shaped MHD power system in generator mode and its cross section.

1.3   History and State of the Art in the Field

Magnetohydrodynamics developed as the science which is at the overlap of electromagnetics, fluid dynamics, and thermodynamics. The initial need for this branch of physics was to study astrological phenomena, specifically the behavior of hot fluids moving on the surface and center of planets. Due to the high temperature, most of these fluids are in a plasma state (i.e. are ionized gases) and are therefore electrically conductive and become susceptive to the phenomenon of induction. Other applications of the MHD principles are sensors and metal pumps.

Research particularly on the power generation application of MHD started with Faradays' experience of the induction phenomenon. He personally attempted to capture the voltage induced by earth's own magnetic field into the river Thames [4]. His readings were inconclusive, as measuring apparatuses were not sufficiently accurate at that time. Nonetheless, this experience is a significant milestone in the history of magnetohydrodynamic power generation.

Efforts to harvest energy from induction into fluid conductors have peaked in the 1960'. Research published during this period [1] [2] [3] and [5] [6] [7] [8] conveys an optimistic view on the industrialization and commercialization of MHD power generators. More contemporary research features a lumped parameter model presented in [9], power generation by a corona jet is investigated in [10], and preliminary experimental results of a supersonic MHD generator are shown in [11]. Research on MHD power generation can be divided into two major sections, depending on the working fluid used. Both plasma [9] [10] [11] [12] and liquid metals [13] [14] [15] [16] are valid candidates for MHD applications, as they are electrically conductive.

The present work aims to expand on the existing research pool, by offering a complete characterization of a permanent magnet excited liquid Gallium MHD generator, through mathematical and computer aided modeling, considering efficient and an application oriented design.

1.4   Dissertation Outline

This dissertation opened with an introduction showing the motivation behind this work. Furthermore, the research objectives were laid out and a high level description of the MHD generator operation was provided. A history of magnetohydrodynamics was included in this introductory chapter as well.

Chapter 2 provides an in depth description of the MHD generator elements mentioned in the introduction. Each physics is treated individually and possible implementation methods as well as their benefits are discussed. Additionally, this Chapter includes the mathematical background of the physical phenomena behind MHD power generation.

After the initial description of the magnetohydrodynamic process, Chapter 3 goes a step further into the subject with a comprehensive derivation of mathematical model of the MHD power generator. Output parameters such as load current and efficiency of the generator can be determined with this model for a known operating point. The sensitivity of this model is briefly studied and thermal influence on the generator outputs is explored.

Chapter 4 describes the process of modeling the MHD generator, considering multiple physics. The multiphysics model is three dimensional (3D), generated in COMSOL, and includes tight coupling between the electromagnetic, fluid dynamic and thermodynamic physics .Micro- and macro-level results are discussed in depth and modeling results are compared to the analytical results obtained in Chapter 3.

Chapter 5 describes the permanent magnet excited liquid Gallium MHD generator prototype. The multiphysics model of Chapter 4 is adapted to accurately represent this generator. Experimental measurement are discussed and compared to the multiphysics modeling results.

After verifying the accuracy of the simulation model, an optimization study is conducted in Chapter 6. The effect of design parameters on the generator output is assessed. The impact of some of these parameters is not considerable in the mathematical model, requiring therefore this modeling approach. Design guidelines are summarized to aid future design projects in the field of liquid metal MHD power generation. Furthermore, to show the applicability of MHD power generation, a case study is presented in this Chapter. The MHD channel is incorporated into a thermal to electrical energy conversion solution targeting waste heat harvesting. The system elements are described and the overall efficiency is determined for various operating points. This

renewable energy system is further compared to a common technology in the field of thermal to electrical energy conversion devices.

Finally, Chapter 8 concludes this work. It provides a summary of the conclusions, outlines the contributions of this body of work and lastly offers an outlook on the future research possibilities related to the here presented work.

CHAPTER 2

MAGNETOHYDRODYNAMIC POWER GENERATION

A brief overview of the components was provided in Chapter 1. In this chapter, each system component will be described individually with its possible variations in implementation. Arguments for and against each selection are discussed. Further, the mathematical description of the generator operation is derived in this Chapter, to provide the theoretical foundation of the generation process.

2.1   System Components

For magnetohydrodynamic power generation to take place, a conductive, moving fluid is exposed to a magnetic field. In addition, the induced voltage needs to be connected to a load, to close the circuit and to provide a path for the current flow. Therefore, the system components discussed are the magnetic excitation, the working fluid, and mechanical components which include passive and active elements. The category of passive mechanical elements comprises of everything needed to render this generator structurally feasible such as the channel holding the fluid and electrodes that capture the electron flow. The mechanical energy input to the generator is considered to be an active mechanical element. This active component will be discussed in Chapter 6 which includes a case study on applied MHD generation.

2.1.1   Magnetic Excitation

The magnetic excitation is a key element of magnetohydrodynamic power generation and can be generated in two ways: by using electromagnets or permanent magnets. Both implementations

bring advantages as well as disadvantages, which are enumerated here to allow an informed decision during the design process, depending on the specific MHD generator design application, operating conditions, and size limitations.

Electromagnets are wound coils used for the purpose of magnetic field generation. Their design (coil shape and power) depends on the application of the electromagnet. The magnetic field generated is adjustable in intensity through the control of the coil current input. This is an advantage of the use of electromagnets in the MHD application, as the voltage output is directly linked to the excitation intensity and orientation, as will be seen in Section 2.2. A further advantage is that electromagnets are able to perform at various temperatures, depending on construction material. It has to be noted that losses in the magnet coils will increase with temperature as the electrical resistivity of the winding increases with temperature. If operated under very low temperatures (close to absolute zero), some electromagnets can be virtually loss less and are able to create fields in the range of 11 to 16.5 T [17]. This type of electromagnets use superconducting materials and are called superconducting electromagnet.

The creation of high magnetic field amplitudes comes with the disadvantage of additional energy cost. This energy cost is seen either as the power to supply common electromagnets or the power to maintain the cooling equipment for superconducting electromagnets. This affects the systems efficiency as well as its size. Therefore, electromagnets are only economically sound solution when building large MHD generators.

Permanent magnets are an obvious choice when a slimmer generator design is sought. As no external power source and no super cooling system are needed, energy cost and design efforts are reduced compared to when electromagnets are installed around the generator. The use of

permanent magnets therefore simplifies the MHD generator setup which is an advantage when prototypes are built.

Arguments against permanent magnets are their low Curie temperature and low flux density created within the fluid channel. Dependent on the type and production method of permanent magnet used, the Curie temperature lays between 310-470°C [18]. At this temperature, the magnet loses its magnetization and becomes thus unable to create the excitation needed by the generator. A consequence of this phenomenon is the limitation set on working fluid selection, as will be seen in 2.1.2.

Both permanent magnets and electromagnets need to be selected (or designed) according to aimed generator performance and geometric shape. The goal is to achieve maximum excitation within the fluid, as this will create maximum power output (this relationship is detailed in 2.2). A selection of maximum strength permanent magnets is therefore obvious, but has to be weighed against cost/benefit. Electromagnets on the other hand, not only introduce high construction cost but also add additional energy consumption in the total energy balance of the generator system. In addition to produced magnetic field strength, the magnets need to fit tightly around the channel which guides the fluid, to provide optimal exposure. Fig. 2.1 shows simulation results of flux density distribution of four different channel/permanent magnets combinations. The average flux densities within the channel are included. It can be noticed that the highest average flux density values are obtained when magnets replicated the channel shape, allowing optimal exposure. This shows the importance of both field strength of the magnet, as well as geometric design optimization of both channel and excitation source.
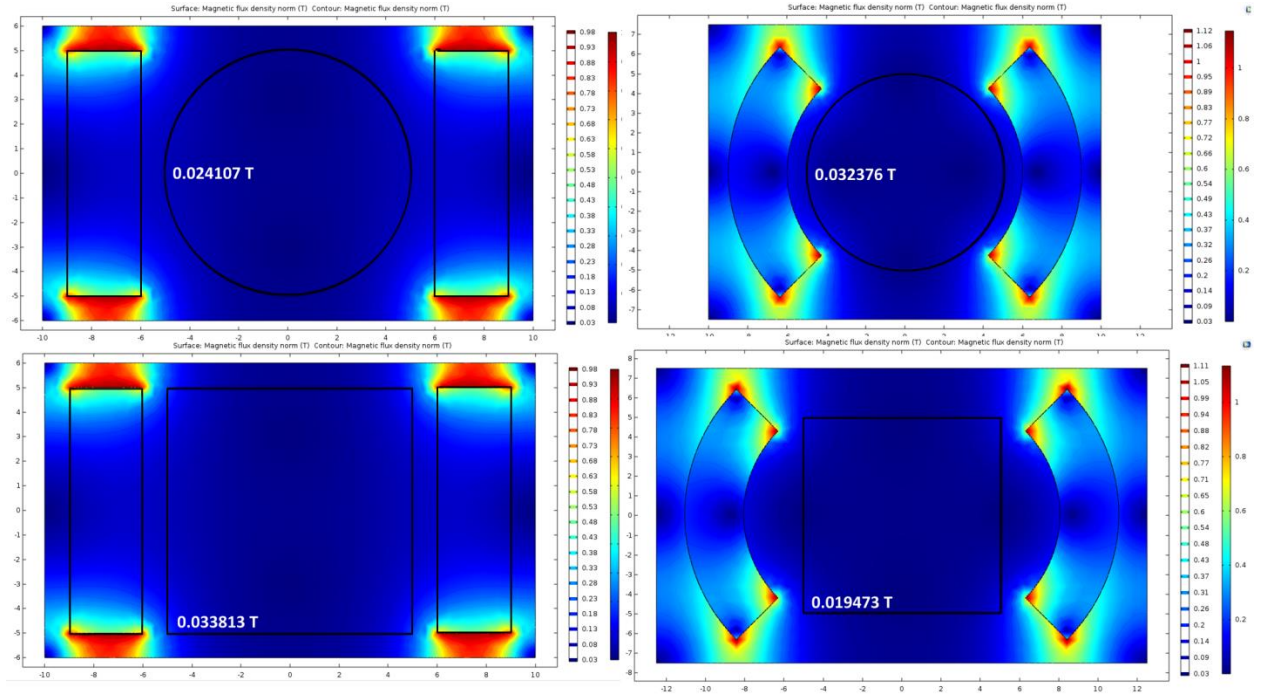
Figure 2.1. Flux density distribution in rectangular and round channels generated by rectangular and circular

The following considerations have been taken in account during the drawing of the model, to assure a fair comparison. The side of the square channel and the diameter of the circular channel are both equal to 10 mm. The magnets remanent flux density is 1.45 T in all cases, with an orientation from left to right. The magnet thickness is 3 mm in all cases. Lastly, the distance between magnets and channel is 1 mm. Where this was not possible due to channel shape, the smallest distance was fixed to 1 mm. Simulations were conducted in 2D Comsol.

2.1.2 Working Fluid

As mentioned in Chapter 1, two types of working fluids can be found in the literature: liquid metal and plasma. These fluids are considered for MHD power generation due to three main properties they possess. Firstly, they are chosen for their state of aggregate. As previously mentioned, a fluid is needed, which includes material in the liquid, gaseous, and plasma state.

Secondly, the selection is further based on their electric conductivity as it is a necessity for the phenomenon of induction. Lastly, the ease of accelerating the fluids needs to be considered when designing MHD generators, as this will affect the energy efficiency of the system as well as the complexity of the generator. Advantages and disadvantages of both are discussed below.

Metals are commonly used in applications where electric conductors are needed, as their electric conductivity is high, resulting in less electrical losses. Aluminum and copper are used in most residential and grid wiring. Gold, silver, and platinum are found predominantly in chip bonding on circuit boards, as they are more costly. High conductivity of metals is a clear advantage but in order to use metals in MHD power generation, high operating temperatures are needed to maintain the metal in its liquid state. Table 2.1 shows melting temperature (m.t.) and conductivity values of common conductors at 20 °C as well as conductivity at each metal's m.t. Although all these metals have high conductivity at room temperatures, their conductivity reduces by roughly one order of magnitude when measured at its melting temperature. This inverse relationship between conductivity and temperature is a disadvantage as elevated temperatures are required to maintain the material fluid.

Table 2.1. Melting temperature and conductivity data for commonly used metals in electrical applications. Data sources: [a] [19], [b] [20] , [c] extrapolated from [21]

Metal	Aluminum	Copper	Gold	Silver
Melting temperature (m.t.) [°C]	660.2 [a]	1083 [b]	1063 [a]	960.5 [a]
Conductivity at 20°C [S/m]	$35.6 \cdot 10^{6}$ [b]	$58.5 \cdot 10^{6}$ [b]	$45.7 \cdot 10^{6}$ [b]	$56.5 \cdot 10^{6}$ [b]
Conductivity at m.t. [S/m]	$5.1 \cdot 10^{6}$ [a]	$1.1 \cdot 10^{6}$ [c]	$3.2 \cdot 10^{6}$ [a]	$5.9 \cdot 10^{6}$ [a]

Another disadvantage of liquid metals is their high density. It is more costly to accelerate one unit volume of liquids than gasses, because kinetic energy is directly proportional to the mass accelerated. Nonetheless, many researchers used metal for MHD purposes, considering various

ways of accelerating the fluid. A common approach is the two-phase flow [13] [22] [23], which consists of mixing the liquid metal with a gas and relying on the gas to propel the phase mixture. Another approach is to use a pump [14] [24] to apply mechanical energy directly to the metal.

Plasma is the aggregate state in which gasses are ionized and electrodes are moving freely within the fluid. This electron availability suggests the fluids potential for magnetohydrodynamic power generation applications. Plasma in MHD is often a gas such as Argon, Neon, Helium, combustion gasses or simply air, seeded with Cesium or Potassium [25] [26] to improve the plasmas electric properties. In some cases gasses are not seeded [12]. Regardless, high temperatures are used to reach the ionization phase, ranging between 1500-4000°K [25] [26] and in some cases up to 9000°K [12], depending on the type of gas used and its ionization temperature. Fig. 2.2 contains electric conductivity data [25] of various seeded gasses within a 2000°K range. A trend of increasing conductivity with temperature can be observed. This can be explained by the increasing degree of ionization caused by higher temperatures. The more molecules in a gas are ionized, the more free electrons are available, thus increasing conductivity. Nonetheless, conductivity values reach between 100 and 1000 S/m. This is significantly lower than the values found for liquid metals, and is therefore considered a disadvantage. An advantage of a working fluid in gaseous state is the ease of acceleration. Nozzles are used to accelerate the fluid to working speeds between 10^2-10^5 m/s [26].
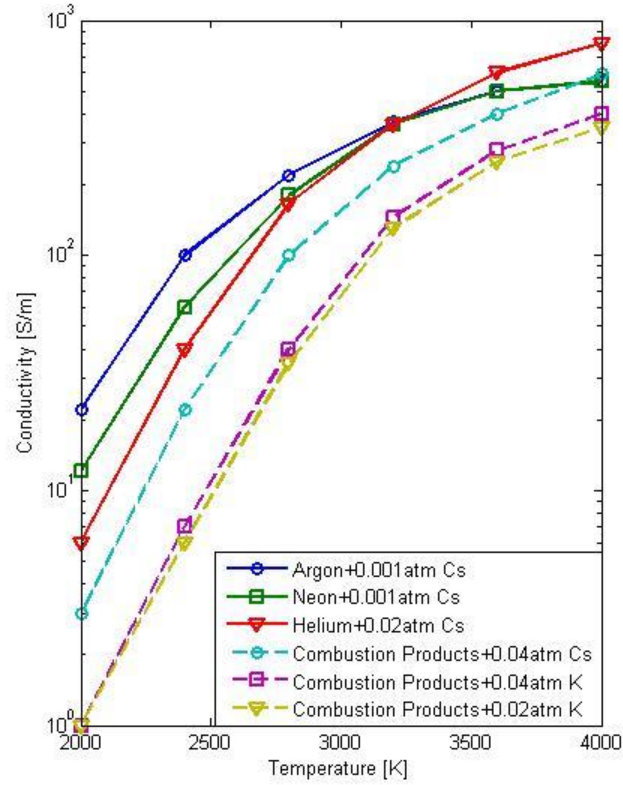
Figure 2.2. Change of electric conductivity of seeded gasses with temperature [25]

In this work, the selection of working fluid fell on the metal Gallium as it has a low melting temperature and high electric conductivity. Table 2.2 includes data on Gallium's conductive properties, as well as other metals with low melting temperature. The conductivity value at its melting point is larger than that of Copper and comparable to that of Gold at their specific melting points. Compared to Sodium and Lithium, conductivity is lower, but so is the melting temperature. Gallium is selected because this permits the low operating temperature of 40°C which simplifies the experimental setup. It furthermore allows the use of permanent magnets in the generator, without the risk of demagnetization (See 2.1.1).

14

Table 2.2. Melting temperature and conductivity data sources: [a] [19] and [b] [20]

Metal	Gallium	Sodium	Lithium
Melting temperature (m.t.) [°C]	29.92 [a]	97.8 [a]	179 [a]
Conductivity at 20°C [S/m]	$6.6 \cdot 10^6$ [b]	$21.3 \cdot 10^6$ [b]	$10.7 \cdot 10^6$ [b]
Conductivity at m.t. [S/m]	$3.8 \cdot 10^6$ [a]	$10.37 \cdot 10^6$ [b]	$4 \cdot 10^6$ [b]

2.1.3 Mechanical Components

Some of the mechanical aspects of MHD generator design have been mentioned in the previous sections: channel shape and fluid acceleration methods, coupled to the generators excitation and working fluid. This section will include more details about these passive mechanical components. Additionally, material selection considerations are laid out.

The generator channel section in which the working fluid passes and through which it is exposed to magnetic excitation is also called active length. An appropriate channel is designed to allow for maximum excitation penetration and should therefore be constructed from nonmagnetic material. Additionally, walls need to be thin to allow for close proximity to the excitation generated by coils or magnets. Sturdiness is required, as excitations placed on both sides of the channel are oriented such that they attract each other. Regarding the channel cross section shape, comments were made in Section 2.1.1, as it depends on the excitation. Besides being nonmagnetic, the channel has to be electrically insulated to prevent shorting the electrodes used to harvest the induced voltage. Lastly, porous materials are not recommended, as this increases friction losses.

The active length is also the area on which electrodes are mounted. The electrodes are placed on opposite sides of the channel, along the current path. Furthermore, electrodes have to be in direct contact with the fluid, without obstructing the flow. The electrode material is chosen to be a good electrical conductor, thereby minimizing the resistive losses. It is also recommended to

verify the chemical compatibility of electrode and fluid, as corrosion can appear. For example: the liquid metal chosen for the application studied in this work, Gallium, is highly corrosive to the common conductor Aluminum. On the other hand, Copper and stainless steels are unaffected by the presence of Gallium [27]. Therefore, an experiment was conducted to asses compatibility with brass, the electrode material used in the experimental verification of this work. A sample of Brass is exposed to Gallium, at the generator operating temperature of 40°C for one week. Microscopic pictures (Fig. 2.3) of the material are taken before and after thermal exposure. A slight discoloration can be detected in the exposed sample. Furthermore, small circular Gallium specks are left on the surface even after cleaning the sample. Nonetheless, no significant depth of these corrosions could be measured. It is therefore concluded that bass electrodes are compatible with a Gallium working fluid.
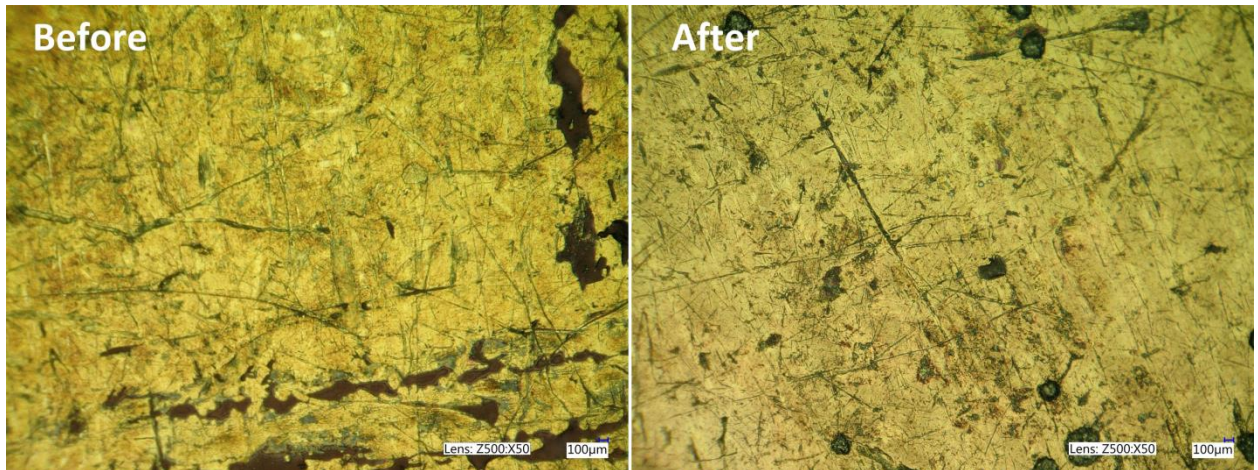
Figure 2.3. Microscopic images of brass, before and after gallium exposure

2.2   Mathematical Description

The influence of the flow and field properties on the generator output is further understood by analyzing the induced electromotive force (EMF) (2.1) from a theoretical point of view. The

EMF along a contour Γ is the negative of the variation of flux Φ in time t through the surface enclosed by Γ, and has two components: the pulsating $u_{e\Gamma p}$ and motional EMF $u_{e\Gamma m}$ (2.2) [28]. The former is dependent on the variation in time of the flux density B through the surface enclosed by Γ (2.3), whereas the latter is considering the effect of the magnetic fields relative velocity v to the system in which the EMF is induced (2.4).

$$u_{e\Gamma} = -\frac{d\Phi_{S\Gamma}}{dt} \tag{2.1}$$

$$u_{e\Gamma} = u_{e\Gamma p} + u_{e\Gamma m} \tag{2.2}$$

$$u_{e\Gamma p} = -\int_{S\Gamma} \frac{\partial \bar{B}}{\partial t} d\bar{s} \tag{2.3}$$

$$u_{e\Gamma m} = \oint_{\Gamma} (\bar{v} \times \bar{B}) d\bar{l} \tag{2.4}$$

To derive the output voltage and power for the MHD generator described in this work, a contour Γ is introduced in Fig. 2.4. The contour is rectangular and the corners are marked with numbers 1 through 4. The illustration shows the orientation of the magnetic flux density B, the fluid flow v, and the direction of the induced electric field relative to the generator channel alongside the integration contour. Direction of unit vectors dl and ds are also marked. As the generator described uses the permanent magnets as excitation, the magnetic field is considered constant with respect to time, thus yielding a pulsating EMF equal to zero. On the other hand, the relative velocity between the magnetic field and flowing liquid metal is equal to the velocity of the fluid, rendering the motional EMF the only type harvested by this generator.

The only segment of the contour contributing to the EMF is between the two electrodes, due to the orientation of unit vectors and because fluid velocity is equal to zero on segments outside the channel. (2.6) finalizes the calculation and (2.7) shows the dependence on the fluid velocity, the

magnetic field strength as well as the length of the segment between the electrodes annotated with *d* of the open load induced EMF. This EMF is constant with respect to time, resulting in an observation that the proposed MHD generator is a DC power generator. The simplification of uniform distribution of velocity and flux density distribution was made for these calculations.
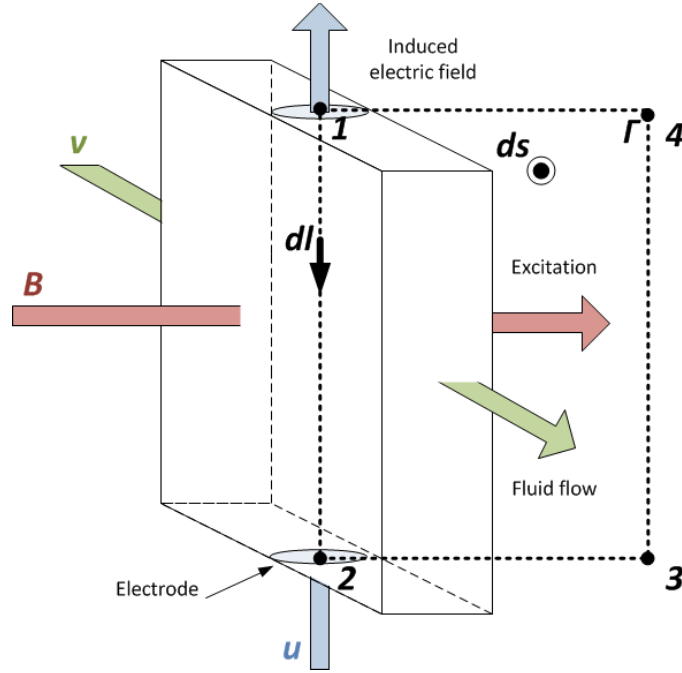
Figure 2.4. Schematic generator channel with integration contour

$$u_{e\Gamma} = \int_2^1 (\bar{v} \times \bar{B})d\bar{l} + \int_3^2 (\bar{v} \times \bar{B})d\bar{l} + \int_4^3 (\bar{v} \times \bar{B})d\bar{l} + \int_1^4 (\bar{v} \times \bar{B})d\bar{l} = \int_2^1 (\bar{v} \times \bar{B})d\bar{l} \quad (2.5)$$

$$u_{e\Gamma} = \int_2^1 (vB \sin \alpha \, \bar{n})d\bar{l}, \quad \alpha = \sphericalangle(\bar{v}, \bar{B}), \quad \bar{n} - unit \ vector$$

$$= vB \int_i^o \cos \beta \, dl, \quad \beta = \sphericalangle(\bar{n}, d\bar{l}) \quad (2.6)$$

$$u_{e\Gamma} = vBd \quad (2.7)$$

It can be observed that the direction of the generated EMF depends on the direction of the fluid flow and the excitation. This observation leads to the fact that AC can be generated if the

direction of flow changes. The frequency of the voltage generated is given by the flow direction change. A direction change in the magnetic field can potentially generate AC as well, but would further induce a pulsating EMF component into the generator, rendering (2.7) invalid for this particular case. An AC implementation of MHD power generation is discussed in [29].

After determining the open load EMF, the behavior of the generator under load is studied. The generator output voltage will now depend on the generator interior and load resistance, R_{Gen} and R_{Load} respectively. For a simple generator-load series circuit the equations are derived as follows. Firstly, because of the series connection, the current through the generator and load, I_{Load} will be equal. Additionally, due to the current flowing through the generator, a voltage drop is present within the generator, reducing the generator output voltage V_{Gen} measured at the electrodes (2.8). Next, the load current can be determined using (2.9). Substituting (2.9) into (2.8) the generator voltage output results to be (2.10). R_{Gen} can be further developed (2.11) and its value depends on generator dimensions and work fluid properties (i.e. electric conductivity σ). l and w represent the length and width of the generator channel respectively.

$$V_{Gen} = u_{e\Gamma} - I_{Load}R_{Gen} \tag{2.8}$$

$$I_{Load} = \frac{V_{Gen}}{R_{Load}} \tag{2.9}$$

$$V_{Gen} = \frac{v\,B\,d}{1+\frac{R_{Gen}}{R_{Load}}} \tag{2.10}$$

$$R_{Gen} = \frac{d}{\sigma\,l\,w} \tag{2.11}$$

2.3　Summary

This Chapter described the main elements of magnetohydrodynamic power generation and discussed the implementation adopted for this work, namely, a low temperature liquid metal MHD generator, with permanent magnets as excitation and Gallium as work fluid. Furthermore, the operation of the generator and interaction between the generator components was detailed by deriving the theoretical voltage output of the generator under no-load and load condition, based on the fundamental equations of the phenomenon of induction.

CHAPTER 3

MATHEMATICAL MODELING OF THE MHD POWER GENERATOR

After describing the fundamental requirements for magnetohydrodynamic power generation as well as the basic physics of the phenomenon, this Chapter introduces a mathematical model. This model offers a macroscopic view of the generator behavior, such as current/voltage characteristics and efficiency for various operating conditions, considering load, generator dimensions, fluid speed, excitation strength, and working temperature. The limitations of this model are also discussed.

3.1   Generator Output

3.1.1   Output Current and Voltage Derivation

The EMF and load voltage of the permanent magnet excited liquid metal (PMLM) MHD power generator were derived in Section 2.2. However these considered an ideal case, with the purpose of explaining the generator operation. In reality, some adaptations are needed to better model the PMLM MHD power generation. Two adaptations are proposed here, which affect the EMF and load voltage equations derived earlier: harness resistance and effective electrode distance.

Harness resistance refers here to the resistance of the electrodes as well as wiring and connectors between generator and load, which cause additional losses in the system. Harness resistance is especially important when the generator's resistive load is small and comparable in value to the generators internal resistance and harness resistance. The circuit model, consisting of the generator in series with the load is similar to the circuit used for derivation as in Chapter 2, is shown in Fig. 3.1. The harness resistance is divided into two parts R_{H1} and R_{H2} and placed one on

each side of the generators, representing loss in the wires from and to the load as well as the top and bottom electrode resistances. The total sum of these resistances is noted with R_H. R_{Load} and I_{Load} are the load resistance and load current respectively. The generator is marked by a dashed box and includes the voltage source $u_{eГ}$ and generator resistance R_{Gen}. The voltage measured between the points A and B is V_{Gen}, the generator voltage output under load conditions.
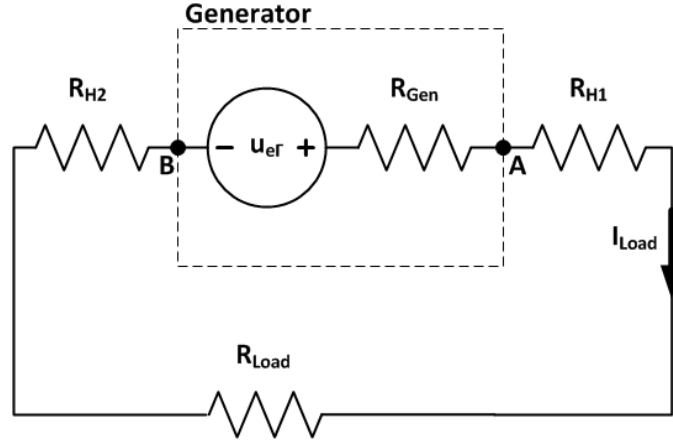
Figure 3.1. Circuit model of loaded MHD generator used for mathematical modeling

The induced voltage $u_{eГ}$ (3.1) is not affected by the introduction of the harness resistor. V_{Gen} on the other hand has to be adjusted. The generator output (3.2) depends in part on the load current, which dictates the internal loss of the generator. As the definition of I_{Load} changes (3.3), due to the addition of R_H in the circuit, V_{Gen} can be expressed using (3.4). Additionally, because of the harness resistances in the circuit, both load current and load voltage will drop. The load voltage V_{Load} (3.5) is now less than the generator output, instead of being equal as it was when harness losses were neglected.

$$u_{eГ} = vBd \tag{3.1}$$

$$V_{Gen} = u_{eГ} - I_{Load}R_{Gen} \tag{3.2}$$

$$I_{Load} = \frac{V_{Gen}}{R_{Load}+R_H} \tag{3.3}$$

$$V_{Gen} = \frac{v\,B\,d}{1+\frac{R_{Gen}}{R_{Load}+R_H}} \tag{3.4}$$

$$V_{Load} = V_{Gen}\frac{R_{Load}}{R_{Load}+R_H} = v\,B\,d\,\frac{R_{Load}}{R_{Load}+R_H+R_{Gen}} \tag{3.5}$$

The second adjustment made to more closely reflect the reality of MHD power generation is the consideration of effective electrode distance $\tilde{d}$. The effective electrode distance will depend on the construction of the MHD channel and its electrode placement, but can be written as (3.6), in which δ represents the height of electrode protruding into the channel (Fig 3.2). Because the electrodes are not flush against the channel walls, the area of moving fluid is reduced. Furthermore, as the electrodes are stationary, no field is induced in these locations. This is reflected in the generator output as seen in (3.7)-(3.10).

$$\tilde{d} = d - 2\delta \tag{3.6}$$

$$u_{e\Gamma} = vB\tilde{d} \tag{3.7}$$

$$V_{Gen} = \frac{v\,B\,\tilde{d}\,(R_{Load}+R_H)}{R_{Load}+R_H+R_{Gen}} \tag{3.8}$$

$$I_{Load} = \frac{v\,B\,\tilde{d}}{R_{Load}+R_H+R_{Gen}} \tag{3.9}$$

$$V_{Load} = \frac{v\,B\,\tilde{d}\,R_{Load}}{R_{Load}+R_H+R_{Gen}} \tag{3.10}$$

To complete this derivation, such that only design parameters are used in the final equations, R_{Gen} can be replaced with (3.11). Thus, (3.8) through (3.10) are replaced with (3.12) through (3.14) respectively. Note that when assigning values equal to zero to δ and R_H (i.e. when neglecting these adaptations), the original equations form Chapter 1 are obtained.
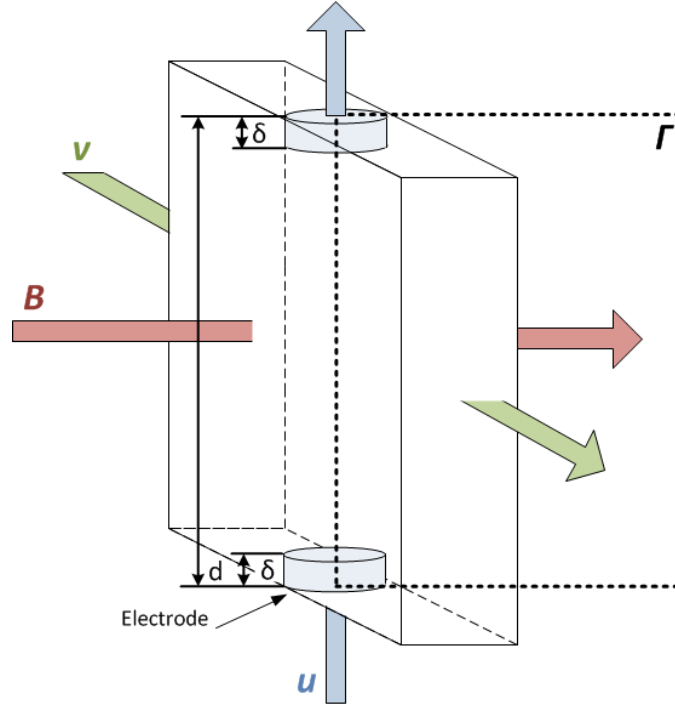
Figure 3.2. MHD generator channel schematic with dimensional electrodes

$$R_{Gen} = \frac{\tilde{d}}{\sigma \, w \, l} \tag{3.11}$$

$$V_{Gen} = \frac{\sigma \, w \, l \, v \, B \, \tilde{d} \, (R_{Load} + R_H)}{\sigma \, w \, l \, (R_{Load} + R_H) + \tilde{d}} \tag{3.12}$$

$$I_{Load} = \frac{\sigma \, w \, l \, v \, B \, \tilde{d}}{\sigma \, w \, l \, (R_{Load} + R_H) + \tilde{d}} \tag{3.13}$$

$$V_{Load} = \frac{\sigma \, w \, l \, v \, B \, \tilde{d} \, R_{Load}}{\sigma \, w \, l \, (R_{Load} + R_H) + \tilde{d}} \tag{3.14}$$

3.1.2 Output Variation with Design Parameters

A study is conducted here to highlight the sensitivity of the generator output to design parameters such as channel dimensions, working fluid material properties, and operating point. Table 3.1 includes the base parameters used in the comparisons. The first comparison made (Fig. 3.3) is between the load voltage and current with and without the adaptations discussed in

24

Section 3.1.1. Note that equating δ and R_H to zero means that the specific adaptation, effective

electrode distance and harness resistance respectively, is not taken into consideration. It can be

seen that both effective electrode distance and harness resistance reduce the load voltage and

current when included in the model. The parameter on the x-axis is fluid speed, which is

evidently directly proportional to the output.

Table 3.1. Base parameter values for voltage and current comparison

d [mm]	δ [mm]	w [mm]	l [mm]	σ [S/m]	R_L [Ω]	R_H [Ω]	B [T]
60	1.4	5	20	$3.6 \cdot 10^6$	0.5	0.1	0.2
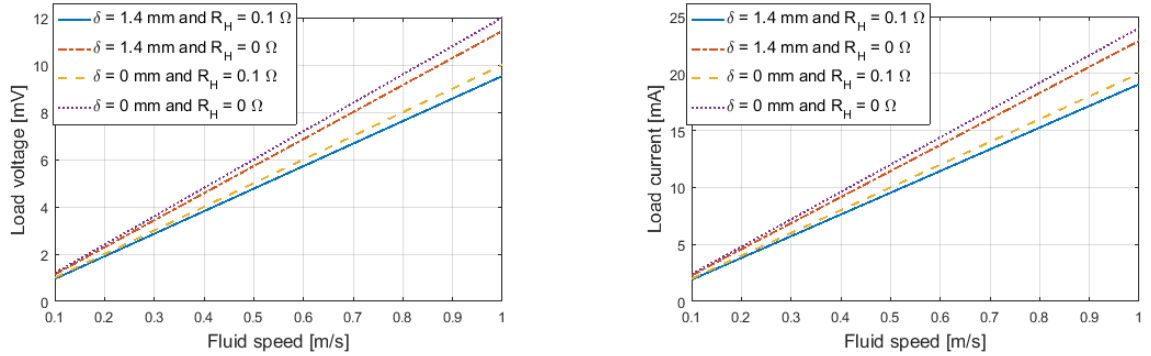
Figure 3.3. Variation of load voltage and current dependent on considered model adaptations

Fig. 3.4 further illustrates the effect on load voltage of other design parameters. The first

observation is that the load voltage increases with all design parameters, except δ and R_H as

mentioned earlier. However, channel width and active length present little impact (Fig. 3.4.b and

c.). Though the load voltage increases with increased width and length, the change in output is

minimal. This is because the already small internal resistance will eventually become negligible.

Once this happens, the load voltage is not able to increase above the induced voltage, minus the

voltage drop on the harness resistance if considered, regardless of the channel dimensions.

Similarly, the load voltage increases with load resistance (Fig. 3.4.e), but once the internal and

harness resistance become negligible in comparison, the load voltage will be equal to the induced

voltage. Taken to an extreme ($R_L \rightarrow \infty$) this becomes the open load condition. Regarding the internal resistance, it can be additionally observed that an increase in electric conductivity increases the load voltage. This is due to the reduced electric losses on the internal resistance of the generator. Lastly, it is noted that an increase in channel flux density and working fluid speed always increases the load voltage, as they directly increase the induced voltage.
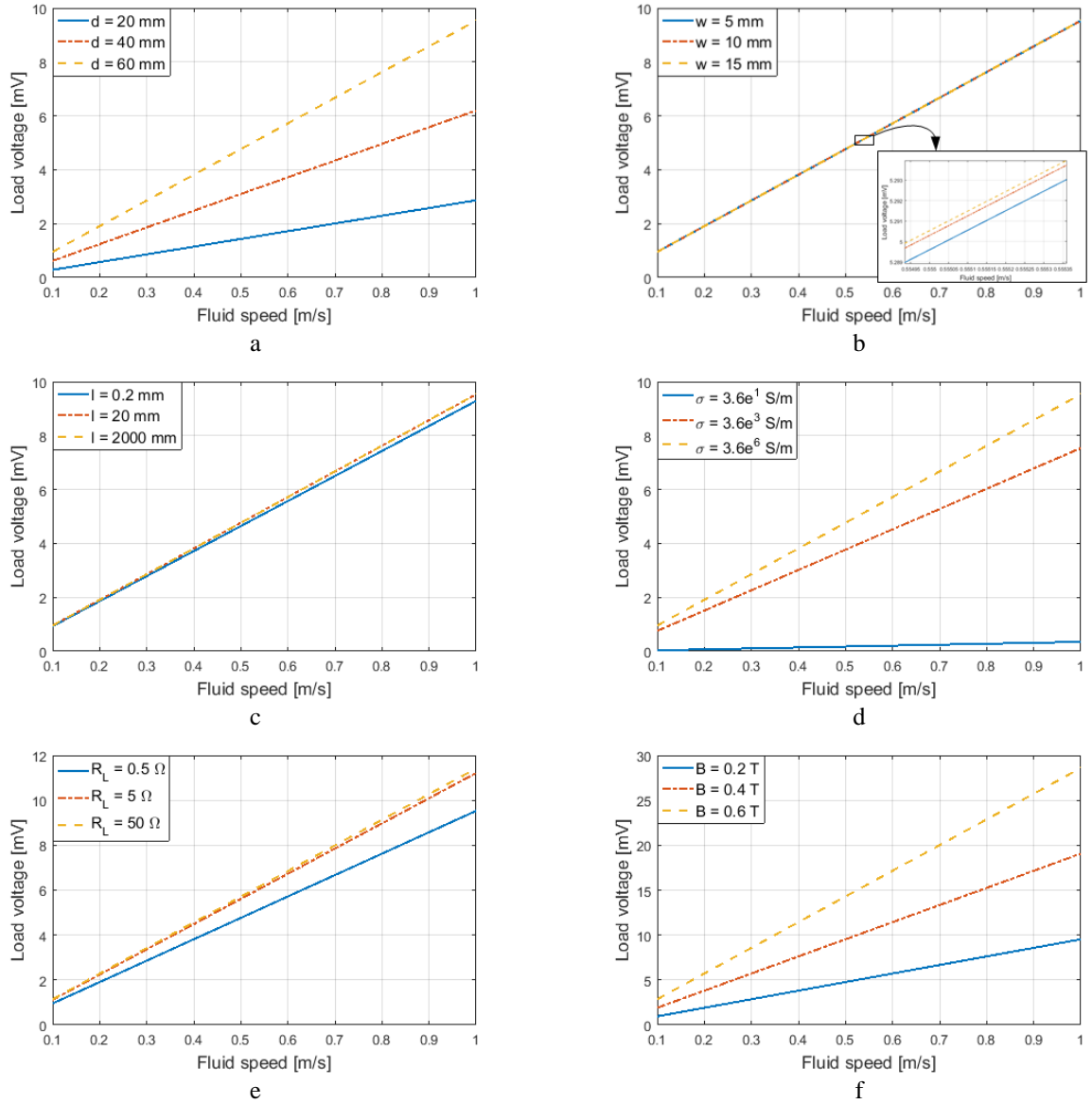
Figure 3.4. Variation of load voltage with a) electrode distance d, b) channel width w, c) active length l, d) electric conductivity σ, e) load resistance R_L, and f) flux density in channel B

3.2   Generator Efficiency

The LM MHD power generator is a mechanical to electrical energy converter, meaning that some of the fluids kinetic energy is harvested and transformed into electricity. Efficiency is a measure of how much of the mechanical input is transformed into useful electrical output. The general equation for power efficiency is (3.15). In this Section, input power P_{IN} and output power P_{OUT} are discusses and mathematically described. Furthermore, losses are analyzed.

$$\eta = \frac{P_{OUT}}{P_{IN}} 100\% \tag{3.15}$$

3.2.1   Mechanical Input and Loss

As stated previously, the input power of this generator is mechanical. This mechanical input can be written as the sum of two elements. These elements are: P_{FL}, the mechanical power of the fluid needed to maintain the fluid velocity in the generator and P_{LO}, the mechanical power needed to overcome the breaking force of the induced current, also known as Lorenz force. It has to be noted that the efficiency calculations presented are considering steady state values for fluid speed and flux density. Therefore, the power needed to overcome the Lorenz force loss has to be added to the mechanical power of the flow (3.16), as the speed used to calculate the kinetic power of the fluid is the speed after the speed drop caused by the mechanical loss has taken effect.

$$P_{IN} = P_{FL} + P_{LO} \tag{3.16}$$

The mechanical power to maintain the fluid speed is derived from its kinetic energy (3.17), divided by the amount of time Δt a unit volume requires to travel from the beginning of the generators active length to its end (3.18). The work fluid mass m is rewritten as (3.19),

considering it as the product of the work fluid density ρ and channel volume *Vol*. This substitution is later helpful for generator design. Furthermore, because this is the kinetic energy of a fluid in a closed channel, the volume is expressed as the product of the area given by the channels hydraulic diameter H_D (3.20) and active length *l*. Finally, the mechanical power of the flow is determined to be (3.21). Note that Q represents the flow rate calculated as (3.22).

$$E_{kinetic} = \frac{m\,v^2}{2} \tag{3.17}$$

$$\Delta t = \frac{l}{v} \tag{3.18}$$

$$m = \rho\,Vol = \rho\,\frac{\pi H_D{}^2}{4}\,l \tag{3.19}$$

$$H_D = \frac{\tilde{d}\,w}{2\tilde{d}+2w} \tag{3.20}$$

$$P_{FL} = \frac{E_{kinetc}}{\Delta t} = \frac{\rho\pi\tilde{d}^2 w^2 v^3}{32(\tilde{d}+w)^2} = \frac{\rho\,Q\,v^2}{2} \tag{3.21}$$

$$Q = \pi\frac{H_D^2}{4}\,v \tag{3.22}$$

The power needed to overcome the Lorenz force is equal to the electrical induced power P_{IND}, as they are rooted in the same phenomenon. Therefore, P_{LO} can be written as (3.23). Substituting (3.7) and (3.9), the electromechanical power is given by (3.24). The generators internal resistance can be expressed using material properties and generator dimensions (3.11), to reduce all equations to the base design parameters.

$$P_{LO} = P_{IND} = u_{e\Gamma}I_{Load} \tag{3.23}$$

$$P_{LO} = \frac{\left(v\,B\,\tilde{d}\right)^2}{R_{Load}+R_H+R_{Gen}} \tag{3.24}$$

The overall mechanical input is thus written as (3.25), solely dependent on generator geometry, working fluid properties, and operating conditions. It can be observed that an

increased operating velocity of the work fluid requires an increase in the mechanical input power. Furthermore, lower density fluids are easier to accelerate, requiring less kinetic power. Lastly, a higher load on the generator would cause less Lorenz force losses, because the overall current generated will be smaller.

$$P_{IN} = \frac{\rho \pi \tilde{d}^2 w^2 v^3}{32(\tilde{d}+w)^2} + \frac{\sigma \, w \, l \, v^2 B^2 \tilde{d}^2}{\sigma \, w \, l \, (R_{Load}+R_H)+\tilde{d}} \qquad (3.25)$$

3.2.2 Electrical Output and Loss

The output of the MHD generator is useful electric power. This can be calculated as (3.26), by subtracting the generators resistive losses (3.27) from the induced power (3.23) or by directly calculating the power consumed by the load using (3.28). The final result is the same (3.29). Again, R_{Gen} is re-introduced, bringing the equation to its final form in (3.30).

$$P_{OUT} = P_{IND} - P_{Rez} \qquad (3.26)$$

$$P_{Rez} = (R_H + R_{Gen})I_{Load} \qquad (3.27)$$

$$P_{OUT} = V_{Load}I_{Load} \qquad (3.28)$$

$$P_{OUT} = \frac{(v \, B \, \tilde{d})^2}{(R_{Load}+R_H+R_{Gen})^2} \, R_{Load} \qquad (3.29)$$

$$P_{OUT} = \left(\frac{\sigma \, w \, l \, v \, B \, \tilde{d}}{\sigma \, w \, l \, (R_{Laod}+R_H)+\tilde{d}}\right)^2 R_{Load} \qquad (3.30)$$

On first sight it can be noted that high velocity and high flux density within the channel increase the absorbed power by the load. On the other hand, harness resistance reduces it, as this additional resistance absorbs some of the generated power. Furthermore, output power will decrease with an increase in load.

29

3.2.3 Overall Efficiency and Variation with Design Variables

Knowing all the elements, the efficiency can be written as (3.31). Fig. 3.5 illustrates the variation of efficiency with generator dimensions, working fluid material properties, and operating conditions. Where not otherwise specified, the values from Table 3.2 were considered as base design parameters. The x-axis for all figures is average flux density within the active length of the generator.

$$\eta = \frac{P_{Load}}{P_{FL}+P_{LO}}\,100\% = \frac{\left(\frac{\sigma\,w\,l\,v\,B\,\tilde{d}}{\sigma\,w\,l\,(R_{Laod}+R_H)+\tilde{d}}\right)^2 R_{Load}}{\frac{\rho\pi\tilde{d}^2 w^2 v^3}{32(\tilde{d}+w)^2}+\frac{\sigma\,w\,l\,v^2 B^2 \tilde{d}^2}{\sigma\,w\,l\,(R_{Load}+R_H)+\tilde{d}}}\,100\% \tag{3.31}$$
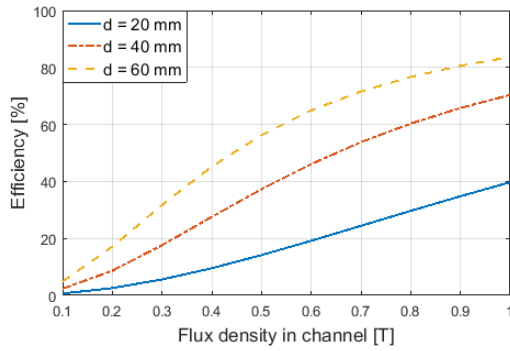
a
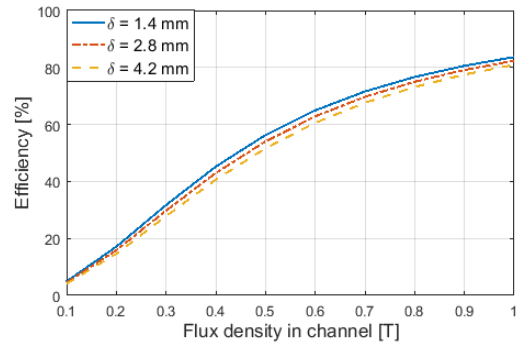
b
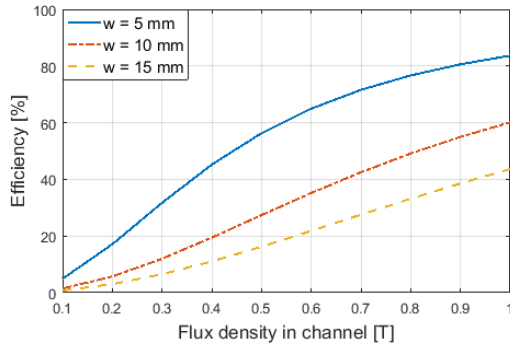
c
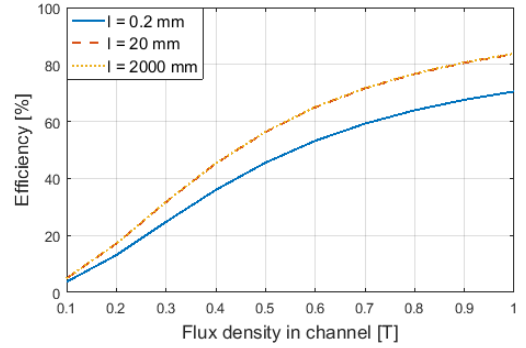
d
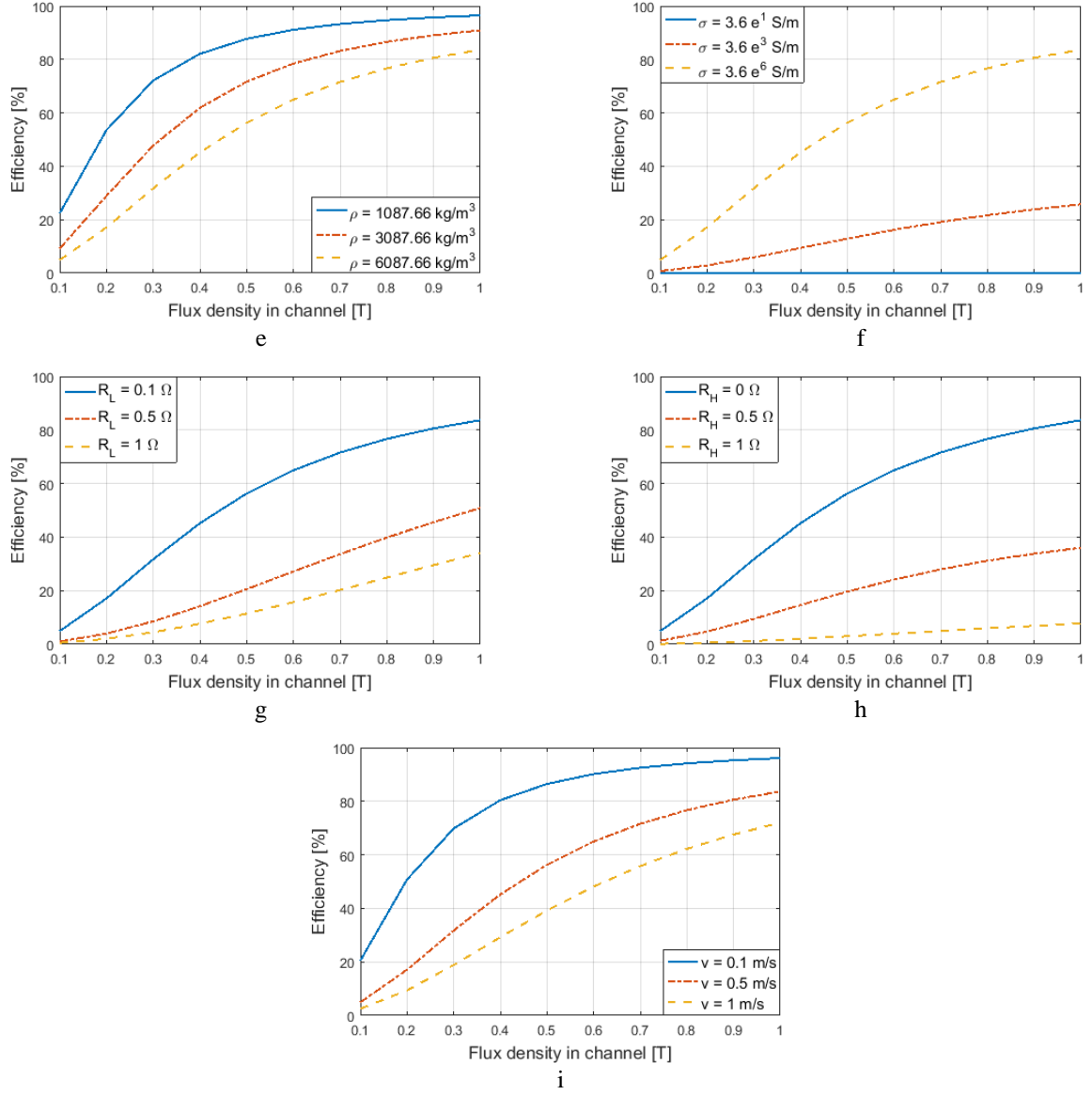
Figure 3.5. Efficiency vs flux density for the PMLM MHD power generator, with changing: a) electrode distance d, b) electrode height δ, c) channel width w, d) channel length l, e) fluid density ρ, f) fluid electric conductivity σ, g) generator load R_L, h) harness resistance R_H, i) working fluid speed v

Table 3.2. Base parameter values for efficiency comparison

d [mm]	δ [mm]	w [mm]	l [mm]	ρ [kg/m³]	σ [S/m]	R_L [Ω]	R_H [Ω]	v [m/s]
60	1.4	5	20	6087.66	$3.6 \cdot 10^6$	0.1	0	0.5

With the help of the derived equation and the figures created using the model, the following trends can be noticed. For electrode distance d, generator length l, electric conductivity σ, and flux density B only, an increase in value results in an efficiency boost. For all the other parameters studied an increase in value in reflected in a reduction in generator efficiency. Further it can be noted that the increase in active length (Fig. 3.5.d) has less of an impact on efficiency. This is due to its role in determining the internal resistance of the generator: a smaller value l results in a larger internal resistance, further leading to lower efficiency. Inversely, the longer the channel becomes, the smaller the internal resistance, but after a certain threshold, which dependent on w and d, the resistance becomes negligible and the overall efficiency does not change significantly. Additionally, Fig. 3.5.f illustrates how electric conductivity affects efficiency through internal resistance. The kinetic power of the fluid does not change, but more useful power is harvested as conductivity increases.

When studying the other two resistances in the system (Fig. 3.5.g and h), it can be observed that both an increase in R_L as well as R_H result in a reduction in efficiency. This is because the induced voltage remains constant but the load current drops. Naturally, efficiency experiences a larger decrease when R_H is increasing than in comparison to R_L increasing, because the power absorbed by the load is the power considered useful in the efficiency equation. An increase in R_H only results in losses.

Lastly, the observation is made that an increase in fluid velocity as well as density decreases efficiency. Although a higher power output can be expected with a higher fluid speed, the power to overcome the Lorenz force increases as induced currents increase. Furthermore, the power

needed to maintain the specified fluid speed increases. Latter is also increased as density increases, thus reducing efficiency.

3.3   Thermal Considerations

Temperature affects efficiency directly and indirectly. The direct way is through the energy needed to maintain the metal in its liquid state to assure continuous operation. This highly depends on the working material, ambient temperature, and operating point. Indirectly, the efficiency is affected by the metal temperature through material properties which change with temperature, as will be seen below.

Because the metal has to be maintained above a specific temperature to remain in its liquid state, it will need an external thermal energy source when the melting point temperature is higher than the ambient temperature. Therefore, the efficiency is directly affected through the addition of a thermal related input term P_{IN_TH} to (3.15), resulting in (3.32). P_{IN_TH} represents the thermal power used to keep the metal molten. In the case of Gallium, this term can often be neglected as the melting temperature is 29.92 °C. Regardless, P_{IN_TH} is equal to the power dissipated by the generator during operation through convection minus the resistive loss within the channel which transforms into heat. This means that under certain operating conditions, the internal resistance may be sufficient to maintain the metal liquid, even if the ambient temperature is lower than the metal's melting temperature. In (3.33) h represents the convection coefficient, ΔT is the difference in temperature between metal and ambient, and $l(2w+2d)$ represents the generator surface exposed to the ambient environment. A P_{IN_TH} different from zero will affect the Gallium temperature inside the generator. A surplus of heat (negative P_{IN_TH}) for instance, created by the internal resistance, is stored by the Gallium through an overall increase in metal temperature.

The degree difference ∂T between the current and future metal temperature (which is different from ΔT) can be determined with (3.34), where c represents the specific heat capacity of the working fluid.

$$\eta = \frac{P_{OUT}}{P_{IN}+P_{IN\_TH}} \, 100\% \tag{3.32}$$

$$P_{IN\_TH} = h \, \Delta T \, l \, (2w + 2d) - R_{Gen} I_{Load}^2 \tag{3.33}$$

$$\partial T = \frac{P_{IN\_TH}}{c \, \rho \, d \, w \, v} \tag{3.34}$$

The second way in which temperature affects efficiency is indirectly through temperature depended material properties such as electric conductivity and density. Generally, both electric conductivity and density decrease with temperature. In Section 3.2.3 the observations were made that a decrease in electric conductivity reduces efficiency and a decrease in density increases efficiency. Therefore, it is specific to the work fluid how efficiency is affected by thermal induced material changes. Table 3.3 includes Gallium material property data for five different temperatures θ and the efficiencies calculated using (3.31) are shown in Fig. 3.6. Note that base parameters from Table 3.2 were used. The material property data from Table 3.3 is obtained from [19] and was interpolated where necessary. Regarding the change in efficiency, it can be noted that efficiency increased by less than 2% when comparing them at 30°C and 500°C operating temperatures. Note that the efficiency equation (3.32) was used which neglects P_{IN_TH}. This is possible when environment and metal measure the same temperature θ °C.

Table 3.3. Changing material properties with temperature

θ [°C]	ρ [kg/m³]	σ [S/m]
30	6094.7	$3.679 \cdot 10^6$
40	6087.7	$3.579 \cdot 10^6$
100	6045.7	$3.077 \cdot 10^6$
200	5975.7	$2.494 \cdot 10^6$
500	5765.7	$1.590 \cdot 10^6$
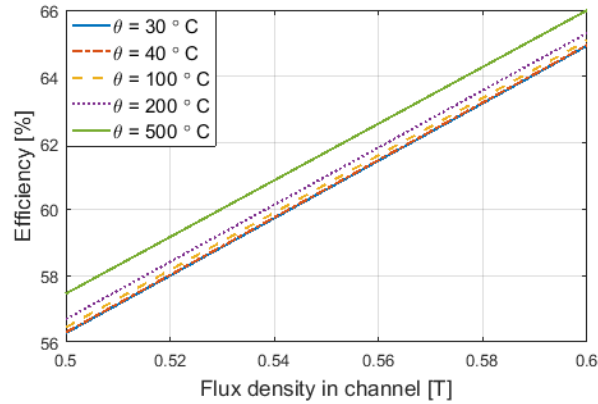
Figure 3.6. Efficiency vs flux density with changing metal and ambient temperature

3.4   Limitations

As with every model aiming to capture the behavior of real phenomenon, the mathematical model presented in this Chapter has certain limitations. These limitations are assumptions and simplifications made which need to be kept in mind when using this model to estimate efficiency and conduct optimal design in the future.

Firstly, the assumption was made that the distribution of flux density and fluid velocity is uniform throughout the channel. This does not happen in reality. Flux density distribution is non-uniform, exhibiting higher values in the center of the excitation source, and smaller towards the rims of the magnet. More regarding the actual distribution will be discussed in Chapter 4. Similarly, the flow profile is in reality non-uniform, as it is bound to the no-slip condition. This condition limits the fluid velocity of the liquid that is in direct contact with the channel walls to

be equal to zero. Furthermore, the distribution of the flow speed depends on the liquids viscosity, which is a temperature dependent parameter and not taken into consideration in this model. Again, simulation results in Chapter 4 will illustrate the flow profile in detail.

Another simplification made to obtain the efficiency model was placing the focus solely on the active length of the generator and not the length of the complete metal circuit. When looking at the entire generator system, changes in pipe diameter and corners for instance, can lead to pressure drops which further increase the mechanical losses. These are not considered in the model derived here.

3.5   Summary

In this Chapter, a mathematical model for the permanent magnet excited liquid metal magnetohydrodynamic power generator was derived, which helps to determine the generators current and voltage output as well as efficiency based on generator channel dimensions, working fluid material properties, and operating conditions. The changes in efficiency caused by different ambient and working fluid temperatures are discusses. Furthermore, the limitations of this model are detailed, providing a full image of the capabilities of this model.

CHAPTER 4

MULTIPHYSICS MODELING OF THE MHD POWER GENERATOR

In the previous Chapter, a mathematical model was proposed, which has one major limitation, namely the inability to provide a micro-level image of the generator behavior. Fluid density and velocity were considered uniform throughout the generator and only macroscopic values such as current/voltage output and efficiency could be determined. Here, a 3D multiphysics model is created which will overcome these deficiencies. Model users will be able to study excitation and flow distributions alongside with induced electric field, current density and Lorenz force within the working fluid. These are determined in addition to the macro-level generator behavior. This Chapter describes the modeling process in detail and provides a comparison to the mathematical model.

4.1   Multiphysics Simulation and COMSOL

Multiphysics finite element (FE) analysis was developed in response to the need of bringing the results of FE model closer to reality. In the study of electric machines for instance, the main physic studies is of electromagnetic nature. However, a more accurate model would also include thermal analysis, because the electromagnetic behavior of a machine is affected by changes in temperature through changes in material properties. Resistive losses in the windings introduce additional heat, thereby increasing the electrical resistance of the coil, further increasing resistive losses. This takes a toll on efficiency which can only be accurately modeled if multiphysics analysis is used.

Magnetohydrodynamic power generation is a phenomenon rooted in the interaction of multiple branches of physics: electromagnetics, fluid dynamics, and heat transfer (thermodynamics). Therefore, it is necessary to build and study a multiphysics FE model, for an accurate estimation of generator behavior. In this work, the modeling is completed in the multiphysics software COMSOL (Version 5.2). This software includes multiple physics, a meshing tool, and solver in the same interface making the modeling process very flexible and highly suitable for modeling the interaction of different physics. Because all physics are in the same interface, universal variables can be declared easily and physics can affect each other though these variables. Additionally, users can input their own equations, using variables from multiple physics, providing another inter-physics connection. These two methods are illustrated in the following subsection.

4.2   Modeling Process

The modeling process is as follows. The model geometry is drawn, either inside of COMSOL or outside and imported into the user interface. Then, materials are assigned to each geometry element. Next, physics are attributed to the elements, including initial and boundary conditions. Physics refer to the set if mathematical equations the properties of a geometric section of the model have to obey. The following step is meshing, the process by which the entire geometry is divided into small triangular regions. The last step is the post processing, in which the results are displayed. The Subsections 4.2.1 to 4.2.6 describe the main modeling steps used for the study presented in this work.

4.2.1 Geometry and Materials

The geometry (Fig. 4.1) is drawn directly in the COMSOL user interface representing the targeted MHD generator. It includes a rectangular channel between a magnet pair. A 1 mm airgap is left between channel and magnets on each side to account for generator wall thickness. Electrodes are placed on the top and bottom of the channel and a block of air contains the 3D simulation model. One electrode contains two elements: the electrode head, placed inside the channel, and electrode stem, outside the active length of the generator. The dimensions of each geometry element are listed in Table 4.1.
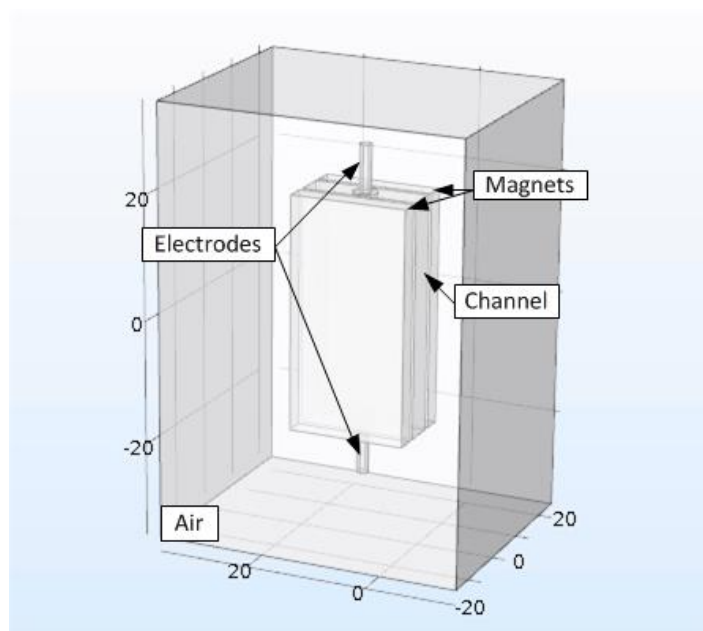
Figure 4.1. Geometry of simulated PMLM MHD generator

Table 4.1. Geometry dimensions

	Height	38.1 mm
Channel	Width	5 mm
	Length	19.05 mm
	Height	38.1 mm
Magnets	Width	3.175 mm
	Length	19.05 mm

Air box	Height	70 mm	
	Width	40 mm	
	Length	50 mm	
Electrode head	Height	1.4 mm	
	Diameter	4 mm	
Electrode stem	Height	7.6 mm	
	Diameter	2 mm	

Three types of materials are assigned to this geometry: air, brass, and Gallium. Air is assigned to the air box and the permanent magnets. Latter is possible because the relative permeability of air and permanent magnets is the same. It is a method often used in FE for electric machine simulations. Brass is assigned to the electrodes, because it is a solid electrical conductor which withstands the corrosiveness of Gallium. Finally, the material Gallium is assigned to the geometry element representing the channel.

Both air and brass have predefined material properties provided by the software. Gallium on the other hand requires manual input. Firstly, the metal is defined as a liquid. Secondly, material properties that vary with temperature are defined as such. The linear equations (4.1)-(4.4) are used to define the thermal dependency for dynamic viscosity μ, electric conductivity σ, density ρ, and thermal conductivity k of Gallium. These are derived from data points provided by [19] and [30]. T is a global variable for temperature in Kelvin.

$$\mu(T) \; [Pa\ s] = \frac{-0.003486(T-273.15)+2.08}{1000} \tag{4.1}$$

$$\sigma(T) \; \left[\frac{S}{m}\right] = \frac{10^6}{0.75949(T-273.15)+248.987} \tag{4.2}$$

$$\rho(T) \; \left[\frac{kg}{m^3}\right] = -0.69987(T-273.15) + 6115.66 \tag{4.3}$$

$$k(T) \; \left[\frac{W}{m\ K}\right] = 0.0481\ T + 11.815 \tag{4.4}$$

The thermal dependency of material properties is one of the earlier mentioned methods of interconnecting the physical branches in a multiphysics simulation. When temperatures vary throughout the geometry of the model, physics such as fluid dynamics (via dynamic viscosity and density) and electromagnetics (through electric conductivity) are inevitably considerate of these changes. This means that the 3D model is able to reflect the reality of the physical phenomenon within the generator more closely.

4.2.2   Magnetic Fields

The physics of magnetic field are applied to all geometry elements, as the magnetic field permeates all of them. The boundary condition for this physics is magnetic insulation on all sides of the air box and is defined by (4.5), with n being the normal direction to the boundary surface and A the magnetic vector potential. This allows for the magnetic fields to be contained within the simulation volume. As the initial condition, the magnetic vector field is considered zero throughout the entire geometry.

$$n \times A = 0 \tag{4.5}$$

An additional definition is applied solely to the permanent magnets, as it is the source of excitation. The magnet strength is given by its remanent flux density B_r and is defined by (6). μ_0 and μ_r are the permeability of vacuum and the relative permeability of the material respectively. The magnets B_r is oriented such that a field is generated perpendicular to the channel. Fig. 4.2 illustrates the resulting flux density distribution alongside the center of the generator channel for magnets with 1.35 T B_r. It is evident that the field is non-uniform, giving the simulation approach more accuracy than the mathematic model described in Chapter 3.

$$B = \mu_0 \mu_r H + B_r \tag{4.6}$$
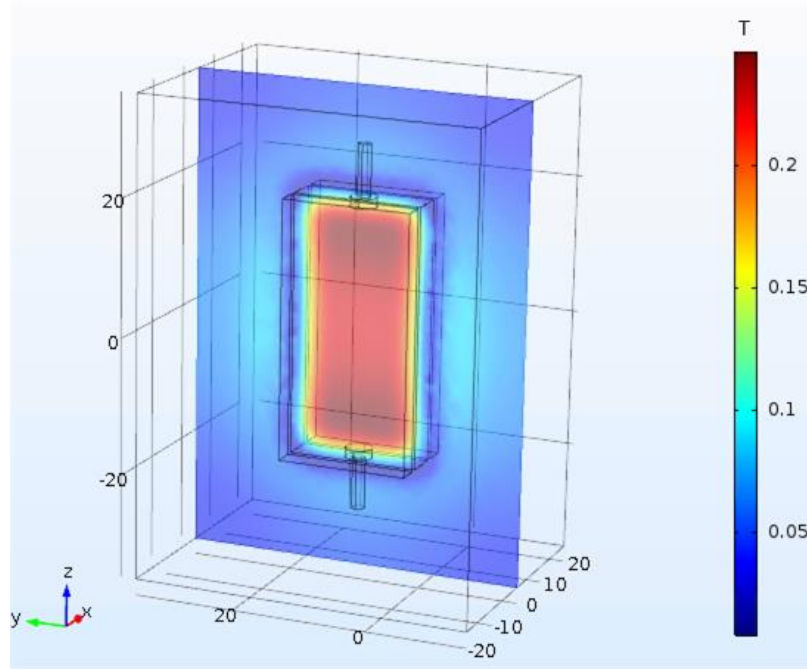
Figure 4.2. Flux density distribution along the channel center plane

4.2.3 Electric Currents and Electrical Circuit

The physics of electric currents is applied only to the electrodes and the channel filled with Gallium. This is because these two elements are electrically insulated from the magnets and the ambient (air box in the case of a model). The boundary condition of this physics (electric insulation) is applied to all sides of the electrodes and channel, except their contact surface. This insulation is described by (4.7). J represents current density. As initial condition, an electric potential equal to zero is provided to the selected geometry elements.

$$n \cdot J = 0 \tag{4.7}$$

An external current J_e density is defined and assigned to the channel in order to model the induced current density. The user-defined equation is reproduced in (4.8). x, y, and z represent

the vector directions relative to the geometry. This equation represents a bridge between the material properties, magnetic fields, fluid dynamics, and electrical currents physics. In this way, the second method of interconnecting multiple physics is implemented.

$$J_e = \begin{cases} \sigma_x \left(B_z\, v_y - B_y\, v_z \right) \\ \sigma_y \left(B_x\, v_z - B_z\, v_x \right) \\ \sigma_z \left(B_y\, v_x - B_x\, v_y \right) \end{cases} \tag{4.8}$$

Besides electrical insulation, two additional boundaries are defined, in order to connect a load to the generator by using the electrical circuit interface. The bottom stem face of the bottom electrode is defined as an electrical ground, meaning that the vector potential is constrained to zero. The top face of the top electrode is defined as a terminal, providing voltage potential information to the electrical circuit. This allows the generator to act as a voltage source in an external electric circuit. The load resistor is connected in series with this generator. Additionally, a second resistor is included to model harness resistance. In this case, because the electrodes are already included in the 3D model, this theoretical harness resistance only includes the resistance of wires leading from and to the generator.

Fig. 4.3 shows the electric vector potential distribution within the center of the channel. Firstly, it is noted that only the electrode and channel show results. This is due to the fact that only these geometry elements are defined as part of this physics. Voltage potential can only be displayed for physics that solve for this parameter. Therefore, no results are available for other parts of the geometry. Secondly it is observable that the bottom face of the bottom electrode was indeed constrained to be an electric ground as in the solved electric vector potential this is respected.
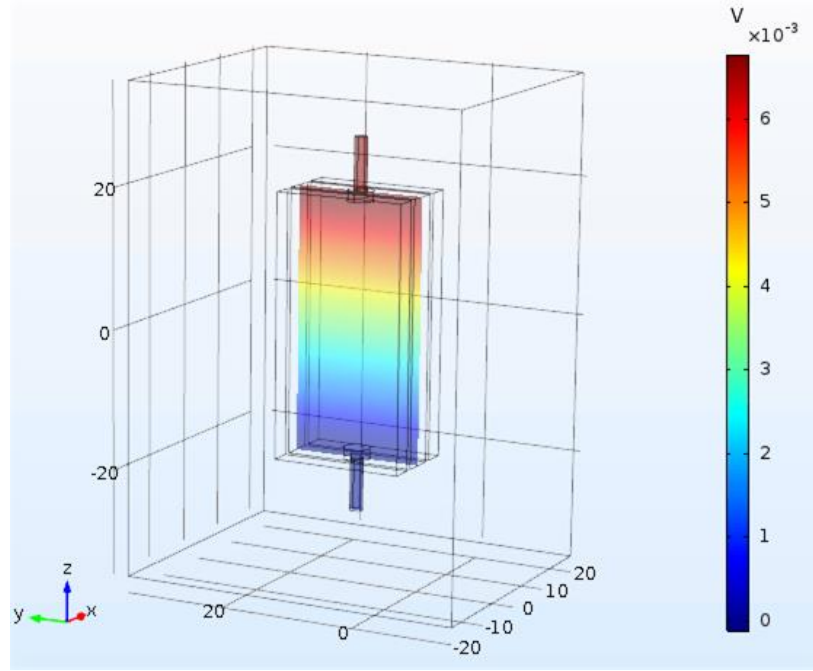
Figure 4.3. Voltage potential distribution along the channel center plane

4.2.4 Laminar Flow

The physics of laminar flow is assigned only to the channel geometry, as the aim is to study the Gallium's flow. Laminar flow is chosen to describe the fluid dynamics of the metal, because the channel dimensions as well as fluid properties in this case suggest laminar behavior according to its Reynolds number. The Reynolds number is a value that describes a fluid dynamics problem and if this value is smaller than 2300, the flow is assumed to be laminar. Values over 3000 suggest turbulent flow behavior. For a 1 m/s average fluid speed at 40°C the Reynolds number can be calculated with (4.9) to be 11.81.

$$R_e = \frac{\rho\, Q}{\mu} = \frac{\rho\, v\, \pi\, H_D^2}{4\, \mu} \tag{4.9}$$

Another number describing quantifying the expected behavior of the flow simulation is the Grashof number *Gr*. This number is at the overlap of flow and heat transfer physics and illustrates how buoyancy forces compare to viscous forces. Buoyancy forces become negligible when *Gr/Re²*<<1, and *Gr* can be calculated using (4.10) [31]. In this equation, fluid material properties such as density ρ, viscosity μ, thermal expansion coefficient β play a role, as do gravitational acceleration *g*, temperature difference between fluid and boundary temperature *Δt* as well as the hydraulic diameter H_D of the channel. In this particular simulation, as the temperature gradient is very small (as will be seen in Section 4.2.5), the effects of buoyance on the flow are neglected.

$$Gr = \frac{\rho g \, H_D^3 \beta \, \Delta t}{\mu} \tag{4.10}$$

The boundary condition used to contain the flow is the so called no-slip condition. It refers to the phenomenon that fluids in direct contact with solids (walls) do not flow/slip. This is expressed in (4.11) and applies to the four side walls of the channel (two facing the magnet and one on top and bottom each) as well as the surfaces of the electrode immersed in the fluid. The inlet and outlet of the channel are constrained in a different manner. The inlet is set up to provide a laminar inflow of a specified average velocity. The outlet provides zero opposing pressure to the flow. General initial conditions are zero fluid velocity and zero pressure throughout the channel. In addition to these conditions, a body force term *F* is defined in (4.12) to simulate the force opposing the fluid flow: the Lorenz force. As can be seen, this force is depends on the induced current and the excitation and therefore represents another multiphysics term. Note that the effect of gravity on the flow is ignored.

$$v = 0 \tag{4.11}$$

$$F = \begin{cases} -J_z\,B_y + J_y\,B_z \\ -J_x\,B_z + J_z\,B_x \\ -J_y\,B_x + J_x\,B_y \end{cases} \quad\quad (4.12)$$

The resulting flow profile can be seen in Fig. 4.4. It is noticeable that it exhibits a non-uniformly distribution and that the no-slip condition is respected. Fluid along the walls and electrode surface is stagnant. Furthermore, a small pocket of stagnant fluid is built behind the electrode. The highest velocities are found in the center of the channel.
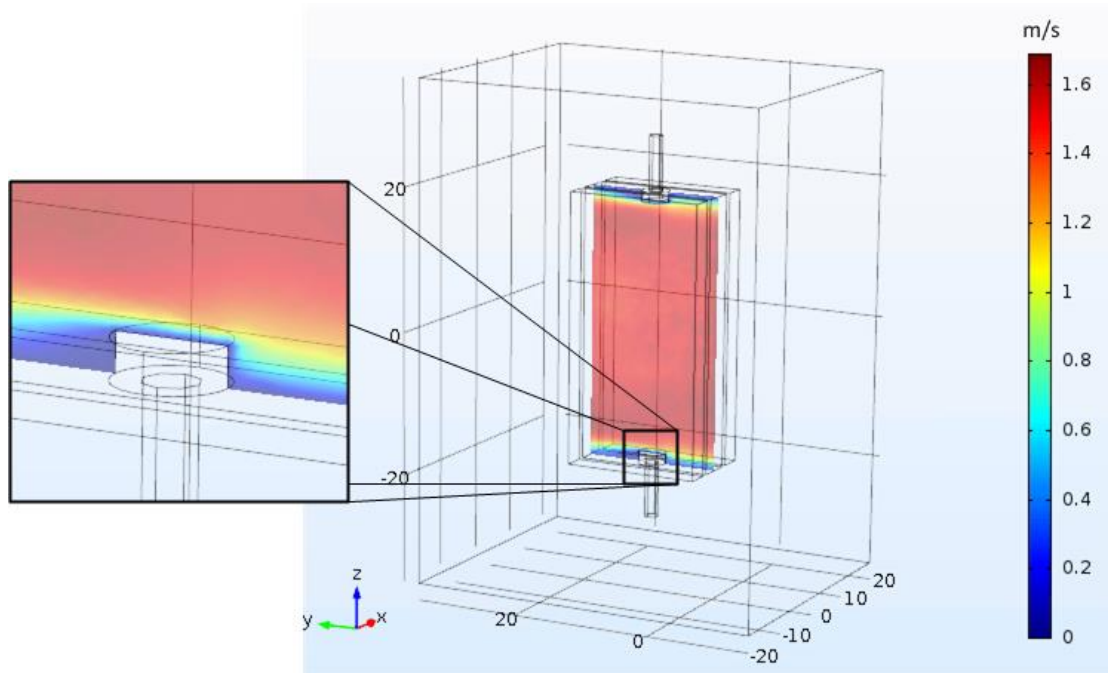
Figure 4.4. Flow speed distribution along the channel center plane

4.2.5 Heat Transfer

The heat transfer physics is applied to all elements in the geometry. A distinction between heat transfer in solids and fluids is made in the software, and properties are assigned accordingly. The boundary condition (4.13) represents thermal insulation of the system and is applied to all sides of the air box. q stands for exchanged heat. Initial values for temperature throughout the

geometry are set to the simulated operating temperature of the generator, in this case 40°C (313.15°K). A heat source is defined within the channel, to simulate the thermal effects of the resistive losses in the generator. The amount of heat is provides by the electrical current physics interface. This is another way in which the physics interact with each other in this simulation model.

$$-n \cdot q = 0 \tag{4.13}$$

Fig. 4.5 shows the resulting temperature distribution along the center of the model. The temperature gradient is small. The maximum Gallium temperature is 313.1501635°K whereas the minimum is 313.1501617°K. Remembering that the initial temperature of the model was 313.15°K, it results that resistive losses are small in this generator. The metals high electric conductivity and low values of generated current are the cause. At other operating points, higher temperatures are reached (Table 4.2). It can be seen that both increase is fluid speed and increase in excitation (remanent flux density) produce a rise in the systems overall temperature, as higher currents are induced and therefore more loss is present to generate additional heat. However, regardless of its amplitude, the inclusion of temperature and its effects on material properties are important to provide a realistic multiphysics model.

4.2.6 Meshing

The most finely meshed area of the model is the channel. This is because this is the location in which all physics interact and where the electromechanical energy conversion takes place. All the other model regions are subjected to less complex phenomenon. In the channel, the mesh element size is between 0.179 and 1.65 mm. Meshing between 1 and 5 mm is applied on the electrodes and 1.26 to 7 mm on the magnets and air box. These size limits for the mesh were

obtained after a brief study into the effect of mesh size on volumetric average flux density in the channel and simulation time. Fig. 4.6 illustrates the mesh of the model as well as a close-up on the mesh size in the channel. Note that three sides of the air box are hidden from view to enable a better view on the meshing of the magnets, channel, and electrodes.
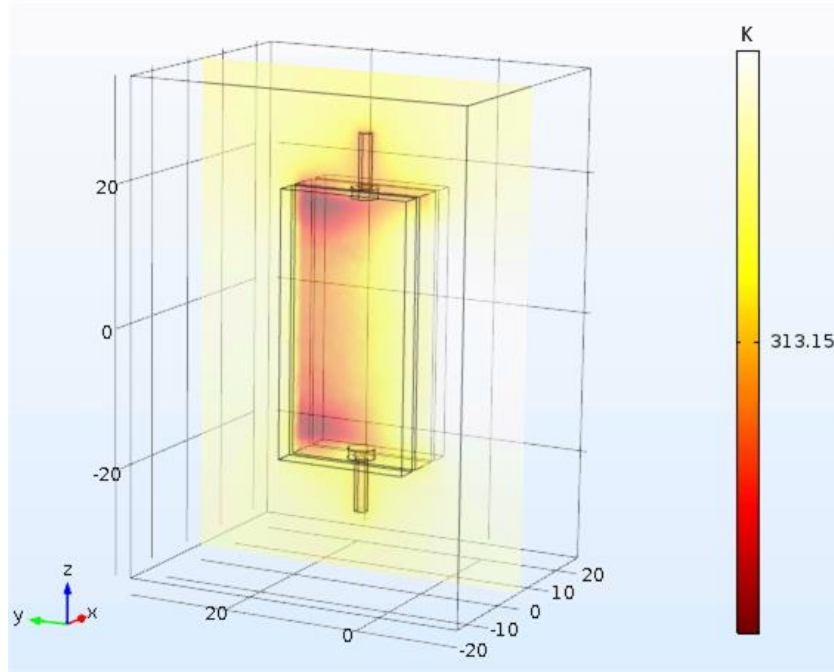
Figure 4.5. Temperature distribution along the channel center plane

Table 4.2. Maximum and minimum Gallium temperatures for different operating points

Speed [m/s]	Remanent flux density [T]	Maximum temperature [°K]	Minimum temperature [°K]
1	1.35	313.1501635	313.1501617
1	6.75	313.1582774	313.158232
1	13.5	313.1834877	313.1833064
5	1.35	313.151135	313.1511212
5	6.75	313.1692954	313.1689505
5	13.5	313.2701209	313.2687428
10	1.35	313.1526508	313.1526196
10	6.75	313.1887162	313.1879392
10	13.5	313.3620472	313.3589351
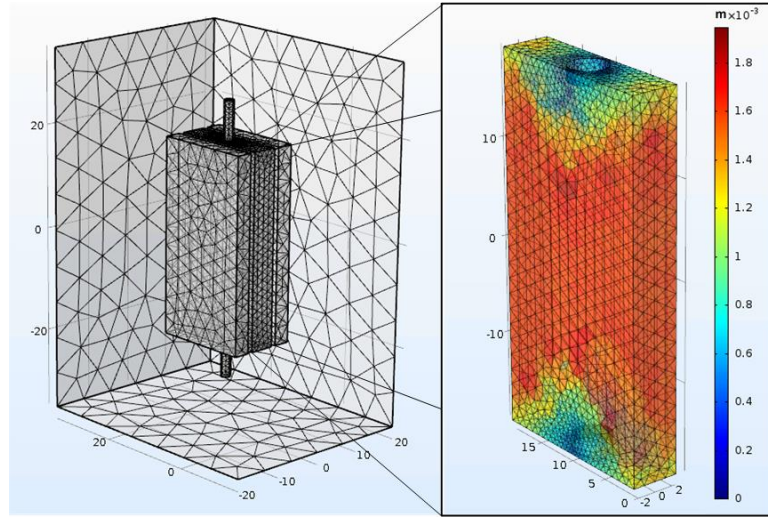
Figure 4.6. Meshing of the model

4.3   Micro-level Simulation Results

Some results were shown in the previous Section to illustrate the effect of boundary conditions on the simulation. Here, more detailed results are provided alongside commentary, to illustrate the interaction between all branches of physics integrated in this model. For this purpose, an imaginary line between the centers of the two electrodes is drawn as seen in Fig. 4.7. The orientation of this electrode axis line is from bottom to top electrode.

   Fig. 4.8 and 4.9 show the flux density, fluid velocity, electric field and voltage potential along the electrode axis line. Three remanent flux densities and three fluid velocities are selected for the analysis in this Section: 1.35 T, 6.75 T, 13.5 T and 0.1 m/s, 0.5 m/s, 1 m/s respectively. Peaks can be noticed in the flux density distribution along the electrode axis line around the 4 and 31 mm point. Because the fluid flow is not fully developed and exhibits a rather flat profile along the axis, these peaks are noticeable in the electric field distribution as well. In the first and last millimeter of the electrode distance, a flat region can be noticed in the voltage potential. This is

49

due to the very slow and stagnant fluid which touches the electrode, constrained by the no-slip boundary condition. No voltage potential is induced in these motionless fluid regions.
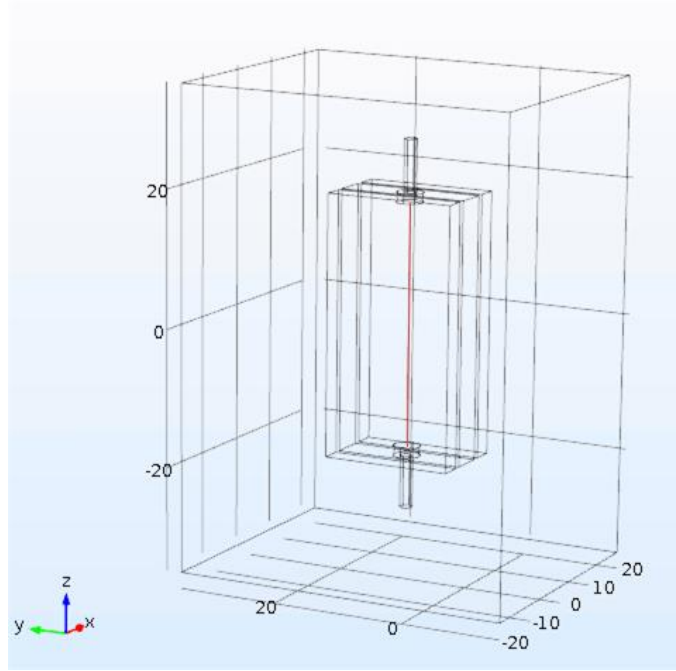
Figure 4.7. Electrode axis line
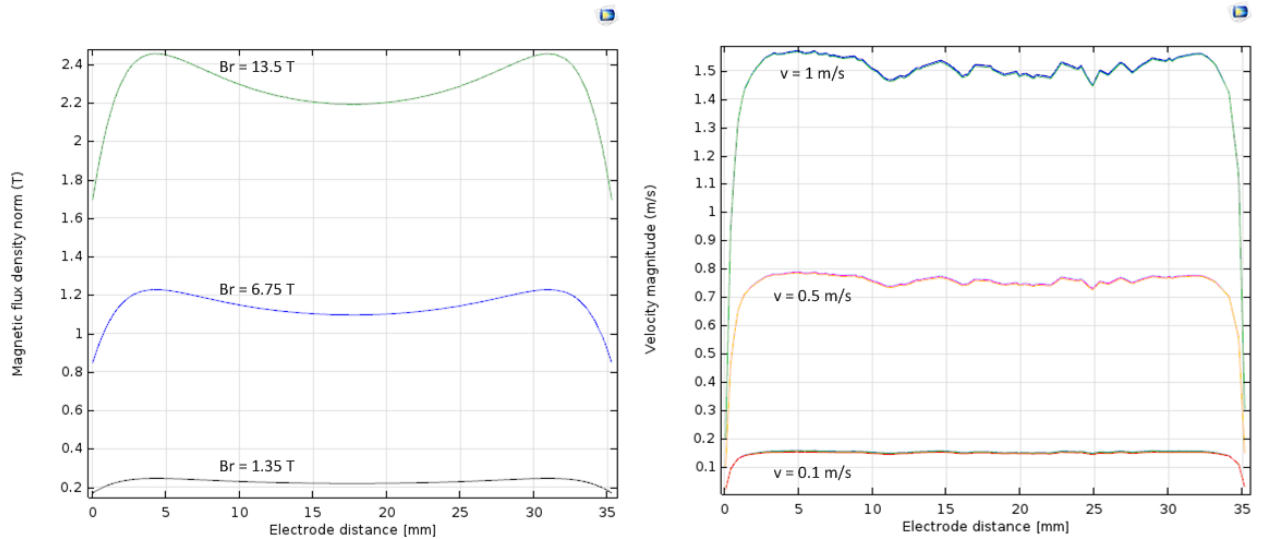
Figure 4.8. Flux density distribution and fluid velocity magnitude along the electrode axis line
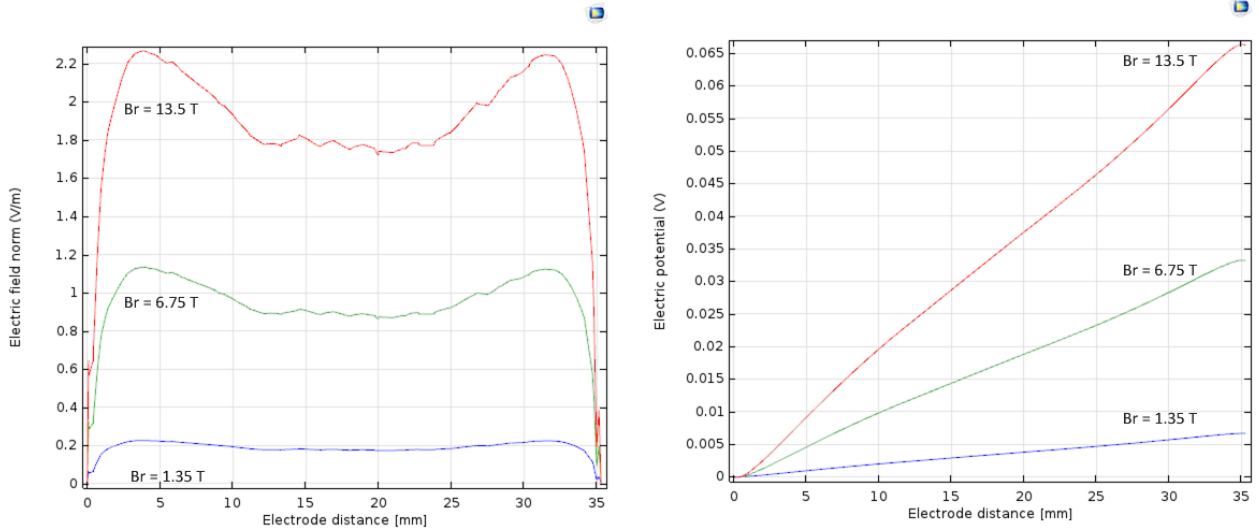
Figure 4.9. Electric field and electric potential at $v = 1$ m/s along the electrode axis line

Fig. 4.10 shows the distribution along the electrode axis line of the current density y component and the Lorenz force z component. The current density and Lorenz force are simulated with the help of the user-input equations (4.8) and (4.12). For current density, the z component represents the harvested currents, as it is oriented along the electrode axis center line. It can be seen that an increase in remanent flux of the excitation increased the induced and harvested current density. For the Lorenz force, the y component is of interest, as this is the direction of the fluid flow. As illustrated in the figure and (4.12), the force is negative in sign and proportional to the fluid and current density. A negative sign indicates that the force is opposing the direction of fluid flow. Peaks in force are noticed around the 5 and 30 mm marks and are due to the peaks in the flux density.

It has to be pointed out that not all currents induced are harvested. Some result in eddy currents as can be seen in Fig. 4.11, which shows the stream lines the current density forms within the generator. It is divided in two components for a better view on the phenomenon. One

51

part is harvested and removed through the electrodes and further guided to the external circuit. The second part remains trapped in the generator, forming closed loops in the Gallium. Because of the close relationship between Lorenz force and induced current density, these eddy currents have a notable effect on the force distribution. Fig. 4.12 illustrates the distribution of the force's y component on the center plane of the channel. It is noticeable that the values along the electrode axis line are negative, thus opposing the flow. Towards the inlet and outlet on the other hand, positive values, thus assisting the fluid flow, are detected. The positive orientation of forces is due to the eddy currents and their orientation in the channel. Therefore, to accurately assess the impact of Lorenz forces in the fluid flow, a study along the electrode axis line is not sufficient. Table 4.3 provides the volumetric average of the Lorenz force y component for all studied operating points. It is clear that, although the amplitude reduced by roughly one order of magnitude compared to Fig. 4.10, the overall trend of the force is to oppose the flow.
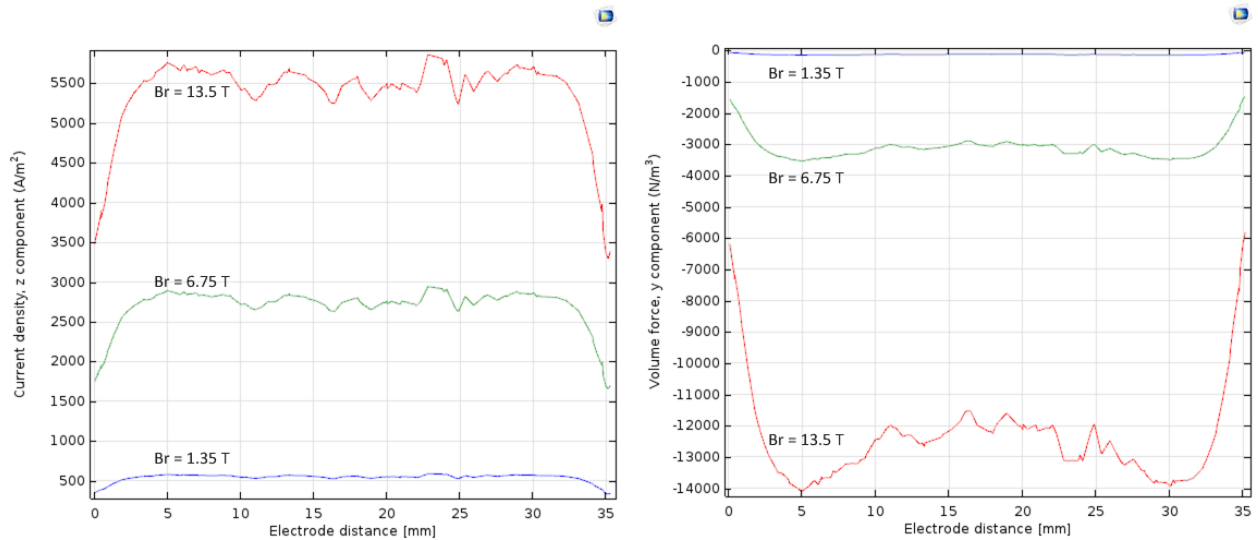
Figure 4.10. Z component of current density and y component of Lorenz force at $v = 1$ m/s along the electrode axis line
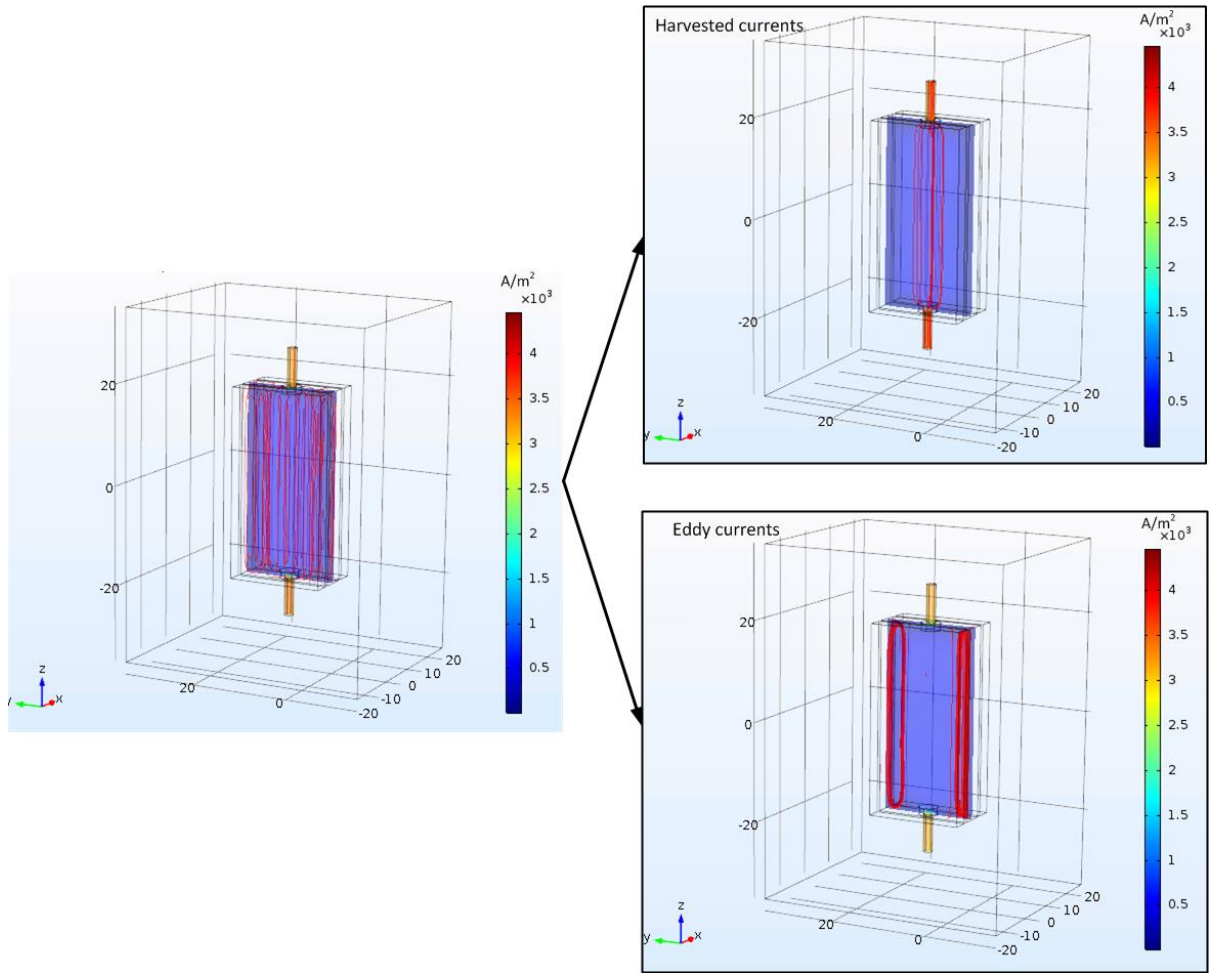
Figure 4.11. Current density and stream lines of harvested and eddy currents for $v = 1$ m/s and $Br = 1.35$ T

Lastly, Fig. 4.13 and 4.14 show the other components of current density and Lorenz force to complete the micro-level study of the generation process. Generally, and as seen in this case, the values of current density in directions other that the harvesting direction (z), are negligible, as their magnitude is small in comparison to the z component. Nonetheless, these stray current in the x and y components have as a result the generation of forces in x and z direction (Fig. 4.14) alongside the y direction. These forces are also small in amplitude, compared to the y component of force (Fig. 4.10), but can cause disruptions in flow patterns as seen in Fig. 4.8. Instead of a

smooth flow profile, small turbulences are detected, even though the Reynolds number of the

system is very small.
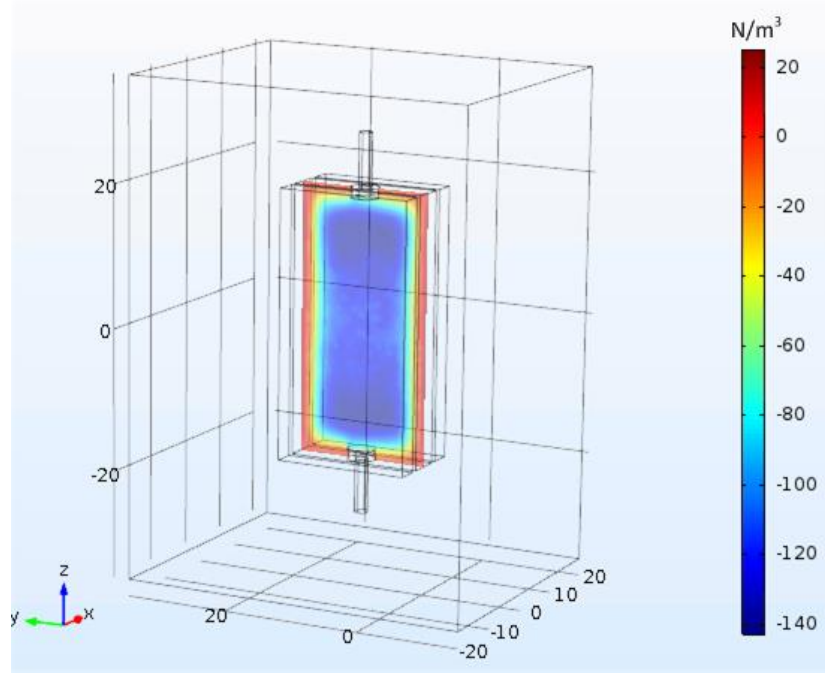
Figure 4.12. Lorenz force, y component distribution along center plane for $v = 1$ m/s and $Br = 1.35$ T

Table 4.3. Volumetric average of the Lorenz force y component which opposes flow for multiple operating points

Speed [m/s]	Remanent flux density [T]	Volumetric average of Lorenz force, y component [N/m^3]
0.1	1.35	-2.20942
0.1	6.75	-54.9465
0.1	13.5	-216.157
0.5	1.35	-11.0326
0.5	6.75	-275.514
0.5	13.5	-1098.28
1	1.35	-22.0349
1	6.75	-550.567
1	13.5	-2198.45
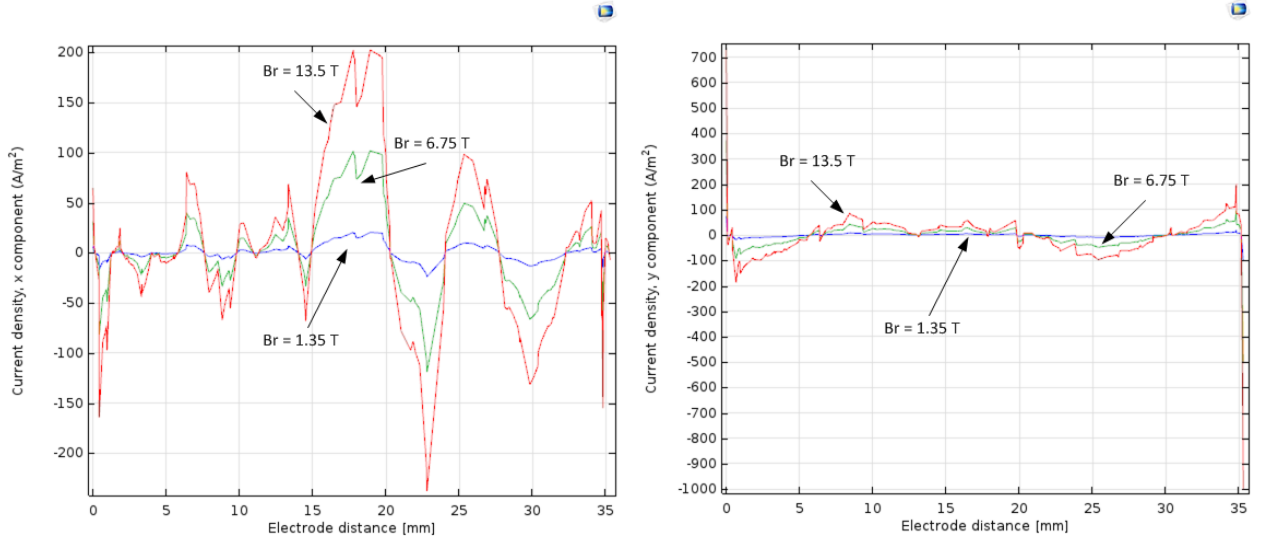
Figure 4.13. X and y component of current density at $v = 1$ m/s along the electrode axis line
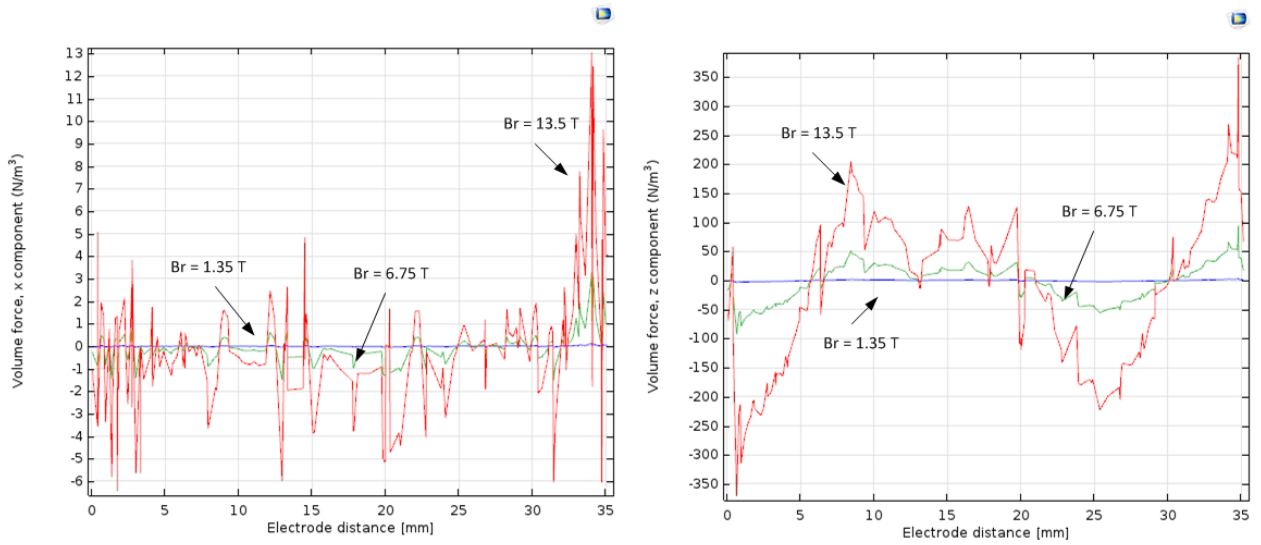
Figure 4.14. X and z component of Lorenz force at $v = 1$ m/s along the electrode axis line

4.4   Macro-level Simulation Results and Comparison to the Mathematical Model Results

Macro-level results refer to the load current/voltage and efficiency of the generator. These are metrics that can be estimated with the mathematical model derived in Chapter 3. In this Section, the macro-level results of the 3D multiphysics simulation and the mathematical model are

compared. Because the mathematical model uses only one value for fluid speed and flux density within the channel and not a distribution that is location dependent, for this comparison, the mathematical model will use volumetric average values of fluid velocity and excitation in the channel to estimate the generator output and efficiency. Table 4.4 contains the volumetric averages determined for each of the studied operation points. It can be seen that the volumetric average of speed changes not only with the average input speed but also with the excitation. An increase in excitation results in higher Lorenz force opposing and thus slowing down the fluid flow. The volumetric average of the flux density is unaffected by speed.

Table 4.4. Volumetric averages of speed and flux density inside the generator channel

Speed [m/s]	Remanent flux density [T]	Volumetric average of speed [m/s]	Volumetric average of flux density [T]
0.1	1.35	0.0994	0.2131
0.1	6.75	0.0990	1.0656
0.1	13.5	0.0978	2.1311
0.5	1.35	0.4968	0.2131
0.5	6.75	0.4964	1.0656
0.5	13.5	0.4951	2.1311
1	1.35	0.9926	0.2131
1	6.75	0.9922	1.0656
1	13.5	0.9909	2.1311

Using the volumetric average data for flux density and flow as well as 0.61 Ω load and 0.137318 Ω harness resistance at 40°C, the mathematical model load current is calculated and noted in Table 5. The harness resistance is determined as the sum of wire resistance of 0.137 Ω, which is also used in the 3D multiphysics model and two times the electrode resistance. The electrode resistance is determined mathematically considering the electrode geometry used in the 3D model (Table 4.1) and the electric conductivity of Brass which is $15.9e^6$ S/m. It can be seen that the mathematical model overestimates the simulation results at every operating point.

Calculating the error e_i using (4.14) it is evident that the error is systematic, varying only slightly between 12.18 and 12.56%. Error increases as speed and remanent flux density increase. The main cause for this discrepancy between results is the simplification of the velocity and flux density distribution within the channel. Another reason is the underestimation of the internal resistance of the generator in the mathematical model. As can be seen in Fig. 4.11, the harvested current is not distributed throughout the generator geometry, but more focused between the two electrodes. This will result in a higher internal resistance as cross section area of the current stream is smaller than the area assumed in the mathematical model. It is not possible to determine this cross section area accurately without simulation.

$$e_i = \frac{I_{math} - I_{sim}}{I_{sim}} \ 100 \ \% \tag{4.14}$$

Table 4.5. Load current comparison

Speed [m/s]	Remanent flux density [T]	Mathematical model load current [mA]	3D multiphysics model load current [mA]	Error [%]
0.1	1.35	1.0004	0.8918	12.18
0.1	6.75	4.9824	4.4393	12.23
0.1	13.5	9.8436	8.7548	12.44
0.5	1.35	5.0000	4.4472	12.43
0.5	6.75	24.9825	22.2153	12.46
0.5	13.5	49.8317	44.3011	12.48
1	1.35	9.9900	8.8781	12.52
1	6.75	49.9347	44.3697	12.54
1	13.5	99.7339	88.6081	12.56

Efficiency can be calculated from simulation results in a similar fashion as the efficiency in the mathematical model. The useful generated electrical power is divided by the sum of the mechanical inputs. To determine the value of the power used by the load, the load current is squared and multiplied by the load resistance. The kinetic power of the fluid, also called hydraulic power, is calculated by multiplying the flow rate by the average pressure difference

57

between the inlet and outlet of the channel. Lastly, the power needed to overcome the opposing Lorenz forces is approximated with the induced electrical power, as in the mathematical model. In order to obtain the induced power from the simulation, the load current is multiplied with the result of the line integral of the electric field along the electrode axis line. The resulting efficiencies and comparison to the mathematical model results can be seen in Table 4.6. The error e_{Eff} is calculated using (4.15).

Table 4.6. Efficiency comparison

Speed [m/s]	Remanent flux density [T]	Mathematical model efficiency [%]	3D multiphysics model efficiency [%]	Error [%]
0.1	1.35	5.0799	6.1201	-17.00
0.1	6.75	51.0055	52.1907	-2.27
0.1	13.5	71.0786	68.1745	4.26
0.5	1.35	1.0697	1.3653	-21.65
0.5	6.75	20.3577	23.8635	-14.69
0.5	13.5	46.6273	49.1779	-5.19
1	1.35	0.5389	0.6684	-19.37
1	6.75	11.6353	13.8003	-15.69
1	13.5	32.6227	35.7470	-8.74

$$e_{Eff} = \frac{Eff_{math} - Eff_{sim}}{Eff_{sim}} \ 100 \ \% \tag{4.15}$$

In the case of efficiency, the 3D multiphysics model provides higher yields. This can be again attributed to the simplification of using the volumetric average in the mathematical model. As seen in Table 4.5, the load current resulted in higher values for the mathematical model. As the mechanical power is fluid speed dependent and the induced power is flow and flux density dependent, these also yield higher results, finally leading to overall efficiency ratio to be smaller than in the case of the simulation.

4.5   Summary

This Chapter illustrates the need for multiphysics simulation due to the complexity of the MHD power generation process and the intertwinement of distinct branches of physics. It further provides a detailed account of the model simulation setup. The modeling results are studied, in particular the results where physics overlap such as electric field, induced currents (harvested and eddy currents) and Lorenz forced. Lastly, the current output and efficiency of a generator with a 0.61 Ω load is found and compared to the mathematical model results. This study reveals that the mathematical model overestimates the current yield, because of the simplification of flow and field distribution as well as internal resistance calculation. Efficiency on the other hand, because of the dominance of hydraulic power in the equation, is underestimated by the mathematical model.

CHAPTER 5

EXPERIMENTAL VALIDATION OF THE 3D MULTIPHYSICS SIMULATION

Chapter 4 addressed the 3D multiphysics modeling process in a detailed manner and provided a comparison to the mathematical model of the liquid metal MHD power generator. In this Chapter, the model is adapted to match the realities of a PMLM MHD power generator prototype and simulation results are compared to experimental measurements. This comparison will validate the simulation approach taken in this study and prove that multiphysics simulation is the tool of choice in the analysis and design of magnetohydrodynamic power generators.

5.1   Prototype and Testbed Description

The permanent magnet excited liquid metal magnetohydrodynamic power generator prototype is built out of a nonmagnetic and non-electrically conductive bloc of acetal (also known as polyoxymethylene). The channel for the Gallium is carved out as well as pockets for 10 permanent magnet pairs. The permanent magnets are placed into pockets to prevent their displacement caused by their magnetic forces between them. The magnets are oriented in the pockets in such way that they attract each other across the channel. Additionally, all magnet pairs are oriented in the same manner to provide a uniform flux density orientation (perpendicular to the flow) as well as direction. Magnet orientation is shown in Fig. 5.1. A transparent lid made from polycarbonate is placed on top to contain the liquid metal in the channel and to secure the magnets. Both lid and generator block provide support to electrodes. There are 39 equidistant electrode pairs placed along the channel: three pairs along each magnet pair and one electrode between two adjacent magnet pairs. Ten of these electrode pairs are considered main electrode

pairs. These are the electrodes centered to each magnet. Lastly, an inlet and outlet are installed into the generator block, allowing the connection of pipes to the channel, and completing the generator prototype. Table 1 contains the generator blocks main dimensions.
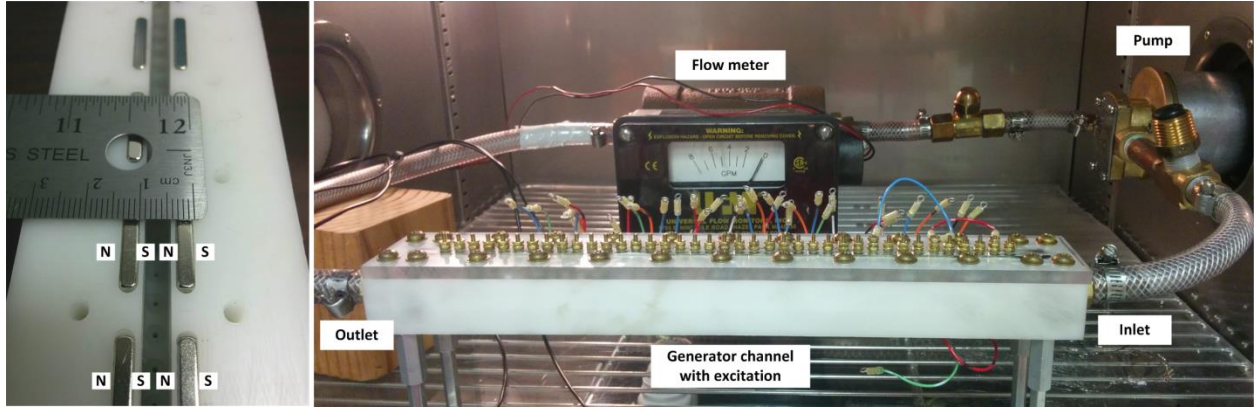
Figure 5.1. Detail of generator block with channel and excitation and testbed setup inside of thermal chamber

Table 5.1. Generator block geometry dimensions

Channel	Height	19.05 mm
	Width	5 mm
	Length	260 mm
	Wall thickness	1 mm
Magnets	Height	19.05 mm
	Width	3.175 mm
	Length	19.05 mm
	Distance between pairs	6.35 mm
Electrode head	Height	1.4 mm
	Diameter	4 mm
	Distance between pairs	6.35 mm
Electrode stem	Height	7.6 mm
	Diameter	2 mm

Fig. 5.1 also illustrates the complete experimental generator system comprising of the generator block, a pump providing the mechanical energy of the fluid at the inlet and a flow meter at the outlet of the generator. The entire flow circuit is placed inside a thermal chamber, to

provide a controlled ambient temperature to the experiments. It further allows maintaining the Gallium liquid at all times. The wiring to the load and for flow meter data collection exits the thermal chamber through a window, which is thermally insulated with foam. Fig. 5.2 depicts the exterior testbed setup. This includes data collection devices such as an oscilloscope for current readings and a digital multimeter for the flow meter output. Additionally, power sources are provided for the pump as well as the flow meter. The load is constructed out of three resistors connected in parallel, which are quick-release, to allow a smooth transition between operating points. The harness resistance, representing the wires from the generators output electrodes to the load is measured to be 0.137 Ω. The experimental results are discussed in Section 5.4.2.
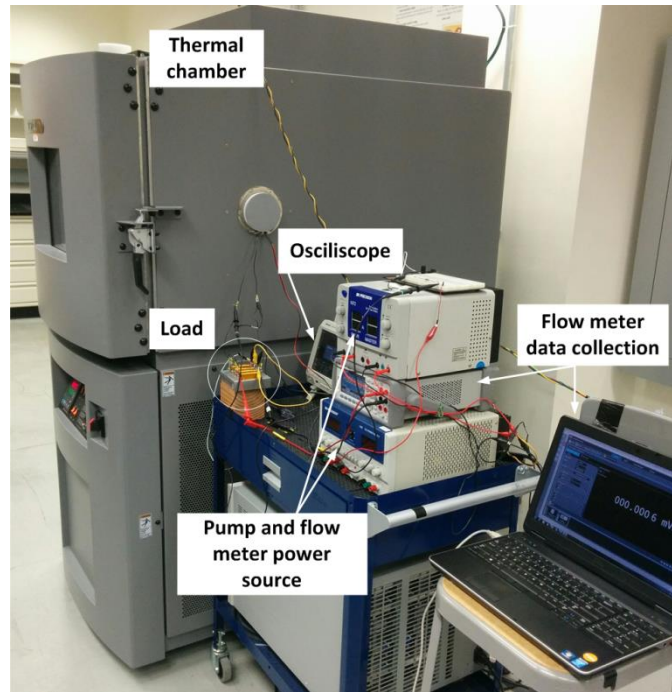
Figure 5.2. Testbed setup outside of the thermal chamber

5.2   Simulation Model Adaptations

The overall 3D multiphysics simulation process follows the same steps as described in Chapter 4. The differences and subsequent adaptations made to reflect the reality of the PMLM MHD prototype are of two types: mechanical and electromagnetic. Under the umbrella of mechanical adaptations, geometry details and flow specifications are considered. From an electromagnetic point of view, changes in excitation due to thermal exposure are studied. All these adaptations are necessary to generate a multiphysics model that is able to predict the prototypes performance as accurately as possible.

5.2.1   Adaptations of Mechanical Nature

First and foremost, the generator channel dimensions, magnet and electrode number, location and distribution are adapted to follow the prototypes, as prescribed in Table 5.1. The simulated geometry is shown in Fig. 5.3. This figure also includes red circles marking the 10 main electrode pairs, which are located in the center of each magnet pair. Adding all electrode pairs to the model geometry has two reasons. On one hand, because it changes the effective electrode distance, which was proven important in Chapter 3 in the derivation of the mathematical model. On the other hand, even electrodes that are not connected to a load affect the flow profile of the metal in the channel and must therefore be included to provide an accurate reflection of reality in the simulation. Another geometry addition that was not included in the generator model of Chapter 4, are the inlet and outlet of the generator channel. It is necessary to include these elements because they have a direct influence on the flow profile in the channel. In this case,

through pressure drops which occur when the flow diameter changes. Note that these attachments are slightly off centered form the generator axis.
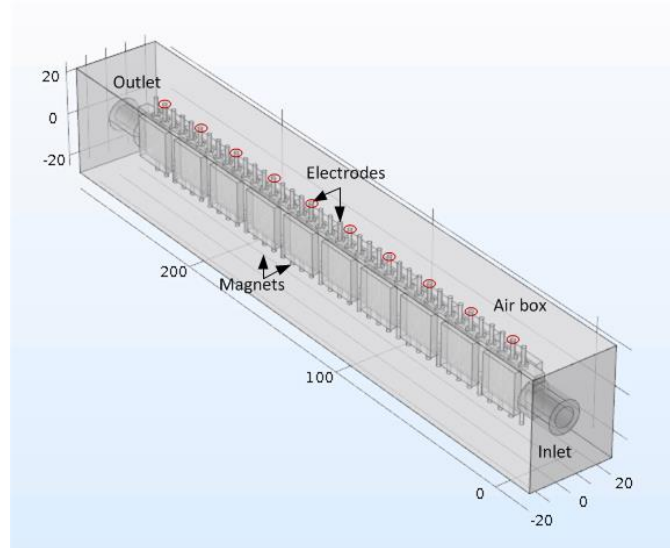
Figure 5.3. Generator block geometry drawing used in simulation including marks for the 10 main electrode pair locations.

To verify if the settings of the fluid dynamics module of the multiphysics simulation still apply to the present context, the Reynolds number has to be calculated for all experimentally verified points. The studied flow rates are 1.3023, 1.4387, and 1.6978 GPM (gallons per minute), leading to Reynolds numbers of 25.8, 30.6 and 33.57 respectively. These are well below the threshold for laminar flow. Therefore, the main physics description remains unchanged. Furthermore, the no-slip condition is as well maintained. One way in which the simulation differs is the inlet and outlet boundary conditions. Because of the generators position in the system, the flow meter reading represents the flow rate at the output of the generator channel. Therefore, the boundary condition of the outlet is constrained to adhere to this flow meter reading, prescribing a fixed output flow rate. The inlet is set to provide zero pressure to oppose the outlet. Additionally, it has to be noted that the flow meter has a ± 2 FS (full scale) accuracy,

which can lead to ±0.16 GPM offset in the flow rate measurements. This is considered later on in the simulation and experiment result comparison, as fluid velocity directly impacts the generator voltage and current output.
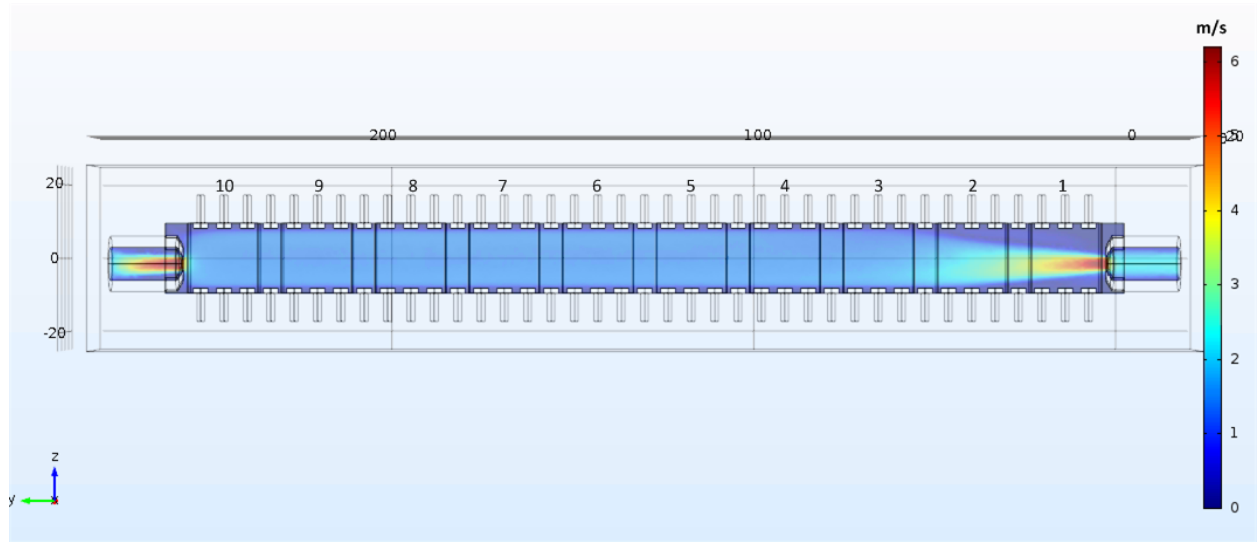
Figure 5.4. Flow velocity distribution in the channel for a 1.6979 GPM output flow rate

To illustrate the effect of all the mentioned adjustments in geometry and flow simulation specifications, Fig. 5.9 is given below. This figure shows the velocity distribution of the Gallium in the channel. The inlet acts like an accelerator for the fluid, but after a certain length, the velocity becomes more evenly distributed and reduced. The flow becomes stable roughly after the 4th main electrode, counting from the inlet on the right hand side of the figure. In this figure, the offset of the inlet and outlet fittings compared to the channel center becomes clear. This offset leads to an asymmetrical flow profile in the first third of the generator. Due to the no-slip condition and the laminar nature of the flow, pockets of stagnant fluid form between the electrode pairs. This reduces the overall volume of fluid that is moved through the channel. This fact justifies the use of effective electrode distance in the calculation of the hydraulic diameter in

the mathematical model. Stagnant fluid can also be found in the corners of the generator, but more pronounced at the inlet side due to the jet-like inflow of Gallium. This stationary fluid does not contribute to power generation because no voltage is able to be induced, as velocity is zero.

5.2.2 Adaptations of Electromagnetic Nature

Two adaptations are completed here. On the electrical side: the previously measured harness resistance of the prototype wires connecting the generator to the load (0.137 Ω) is added. No representative harness resistance is placed in the exterior electric circuit to represent the electrode resistance, because the electrodes are modeled together with the generator.

On the magnetic side of magnetic adaptations, an experiment is conducted to verify the magnitude of thermally induced demagnetization of the permanent magnets used as excitation. It is known that the performance of permanent magnets is sensitive to the ambient temperature in which they are placed. If the temperature of the magnet passes specific critical temperature, the magnet can become irreversibly demagnetized. This temperature is specific to the material of the permanent magnets and is called Curie temperature. The magnets used for the prototype construction are NdFeB magnets, for which a typical Curie temperature lays between 310 and 470°C [18]. Because of the Gallium melting temperature and the resulting possibility of a low temperature operation of the generator, irreversible demagnetization is not an issue. Nonetheless, demagnetization is not a sudden phenomenon, it appears gradually.

Therefore, the following experiment is conducted to determine the extent of the reduction in remanent flux density of the permanent magnets. Fig. 5.5 illustrates the experimental setup. In a MHD channel replica, which follows the same dimensions as the prototype but is missing the flow inlet and outlet connections, flux density measurements are taken in 10 key locations. The

magnets used in this replica are from the same batch as the one used in the prototype. The location of measurement is the center of the electrode axis line for all of the 10 main electrode pairs. The middle point is chosen because it is robust to slight measurement position variation. Fig. 5.6 illustrates the simulated flux density distribution along the line which connects all 10 measurement points.
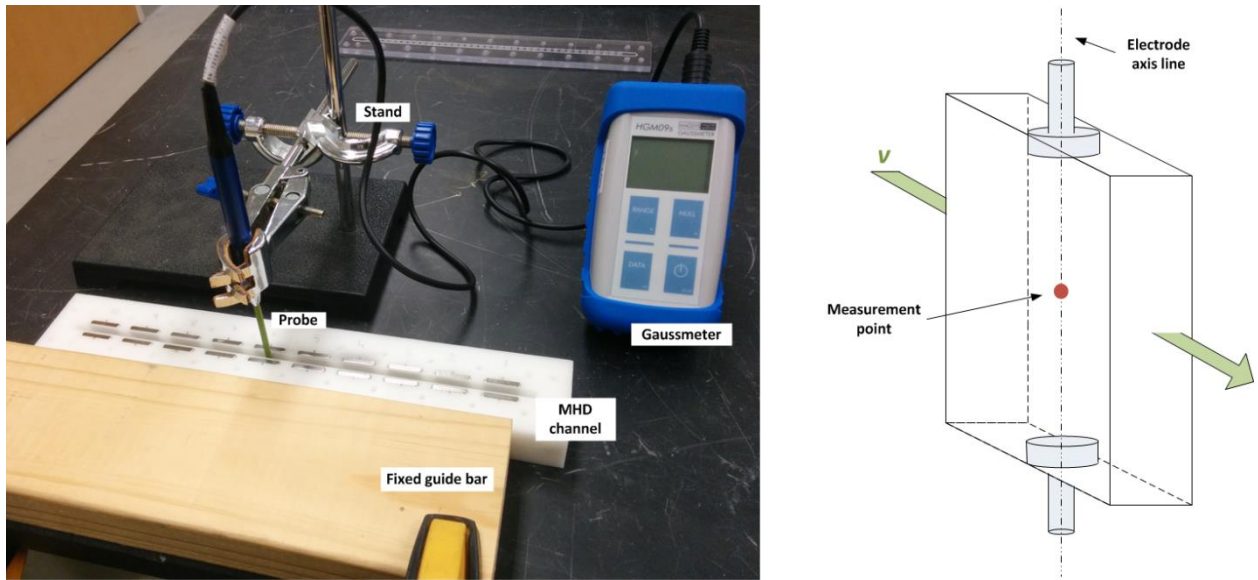
Figure 5.5. Measurement setup and sketch of measurement point location

The flat sections in the flux density are where the measurement points are located and this is what provides the robustness to the measurement. The measurement tool is a handheld HGM09s gaussmeter with a flat, pen style probe. Using the stand the probe is fixed in place to maintain the same probe height in the channel for all measurements. To shift from one electrode pair to the other, the generator block is moved along the fixed guide bar. This prevents misalignment of the probe in the channel. Note that the bar and clamp are nonmagnetic (wood and plastic respectively) to avoid any possible magnetic field distortion.
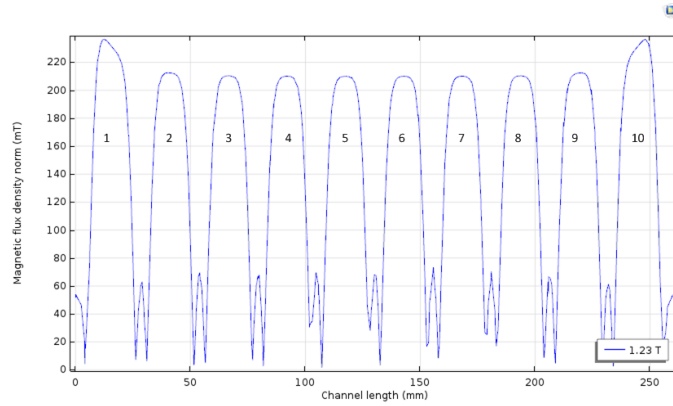
Figure 5.6. Flux density in the channel along the 10 measurement point and in between for magnets with 1.23 T remanent flux density

The flux density measurements are taken five times for all 10 of the main electrodes and averaged to reduce possible error even further. The results can be seen in Fig. 5.7. Even though the measurements are taken as accurate as possible, the intensity of field created by the magnets differs. This is also visible in the simulation (Fig. 5.6) but only for the magnet pairs 1 and 10, which are at the end of the channel. The other measurements (2 – 8) are affected by the inherent discrepancy in properties of the individual magnets. After this set of measurements, the generator replica is placed into the thermal chamber at 40°C, which is the temperature used all experimental measurements of power generation. The measurements taken after 25 days of continuous thermal exposure are also found in Fig. 5.7. Two things are immediately visible. Firstly, the end measurements, for electrode axis 1 and 10, are more evidently higher than the values for electrode pairs 2 – 9 for the measurement after thermal exposure. Secondly, the rate of demagnetization varies from pair to pair. The average of the demagnetization sensed in the channel flux density is 38.5 mT.

68
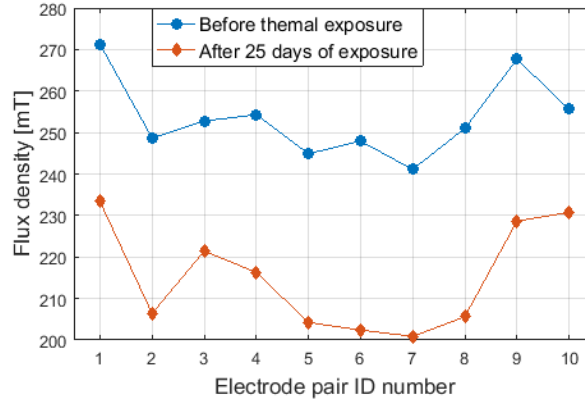
Figure 5.7. Experimental measurement before and after thermal exposure

In order to determine the remanent flux density which should be used in the simulation, the measurement points taken after thermal exposure are fitted with a second order polynomial curve (5.1). x represents the main electrode number and *f(x)* the fitted flux density. Fig. 5.8 shows the measurement data overlaid with the fitted data. To determine the average of flux density in the channel, the average is made of the fitted values between electrode pair 3 and 8, because 1, 2, 9 and 10 exhibit higher values in simulation than the rest. The average results to be 212.37 mT. In a simulation containing only the magnetic physics, and no Gallium, the remanent flux densities for the permanent magnets is swept. From this simulation it is notable that, in order to generate a flux density equal to the average of the measured results in the channel, the remanent flux density of the excitation has to be 1.23 T.

$$f(x) = 1.324\,x^2 - 14.54\,x + 244 \tag{5.1}$$

Fig. 5.9 illustrates the flux density distribution throughout the center plane of the simulated geometry, using a 1.23 T remanent flux density. This represents the generator reality after a 25 day exposure to operating thermal conditions. Here again it can be noticed that the intensity of

69

the field is higher at the inlet and outlet of the channel (electrode pairs 1, 2, 9 and 10). Another observation can be made, which is also valid for the result in Fig. 5.6, and that is the fact that the lowest flux density values are found in between two magnet pairs. Due to the flux density distribution, the magnet centered electrodes are considered to be the main electrodes, as the excitation is more concentrated here. When reflecting on the mathematical description of the power generation process, higher induced electric fields can be expected between the main electrode pairs than at the electrode pairs placed between magnet pairs.
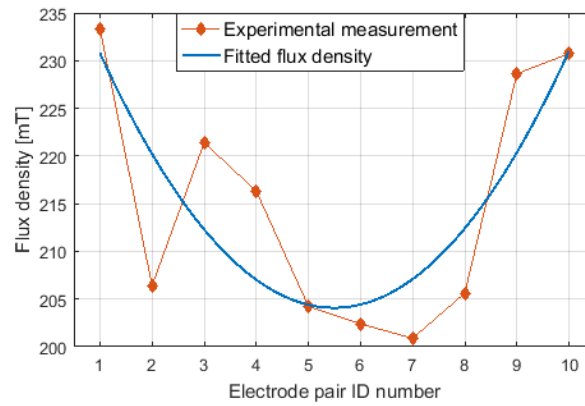
Figure 5.8. Experimental measurement after thermal exposure and fitted curve
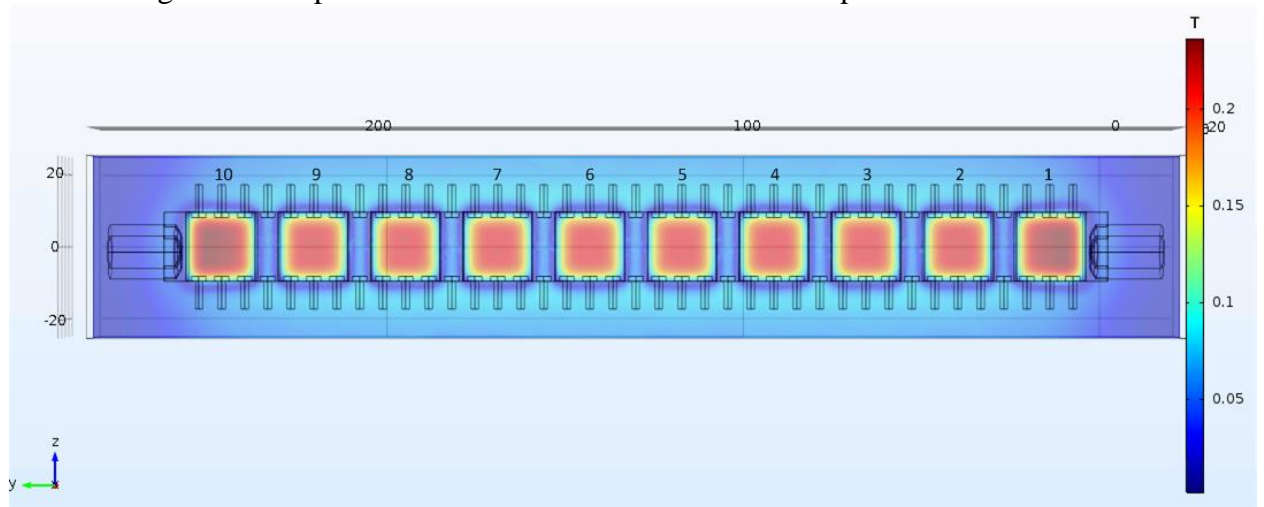
Figure 5.9. Flux density distribution within the generator center plane

5.3 Simulation Results and Comparison to Experiments

As in the previous Chapter, the simulation results are divided in two: micro-level and macro-level results. Micro-level refer to the simulations of phenomena within the generator channel, such as current and force density distribution. This type of results is included to offer better insight and understanding of the generator simulation results. Macro-level results such as load currents and efficiency. In this Section simulated and experimentally measured load currents are compared to validate the simulation method.

The simulations are conducted under the same operating conditions as the experiment. This entails a 40°C ambient temperature for the generator block. Measurements are taken for 0.45, 0.61 and 1.1 Ω load for 1.3023, 1.4387, and 1.6978 GPM flow meter readings at the outlet of the generator. The electrode pair used to connect the generator to the load is main electrode pair number 5. This electrode is selected because simulation results for flow and field have shown that a certain length of channel is needed to provide a stable and generator representative velocity distribution and flux density profile.

5.3.1 Micro-level Simulation Results

The micro-level results for fluid velocity distribution and flux density distribution can be seen in Fig. 5.4 and 5.9. It is observed that both flow and flux vary with location in the channel. Higher speeds are at the inlet, where the fluid is transitioning from a smaller to a larger hydraulic diameter, and flux density is more elevated at the first and last magnet pair due to their proximity to only one other magnet pair instead of two. From these results, the induced electric voltage potential can be predicted to be more intense at the inlet of the generator. Fig. 5.10 confirms this

prediction. It can also be noticed that the main electrode pairs are in position to harvest more power than the electrode pairs placed in between two magnet pairs.
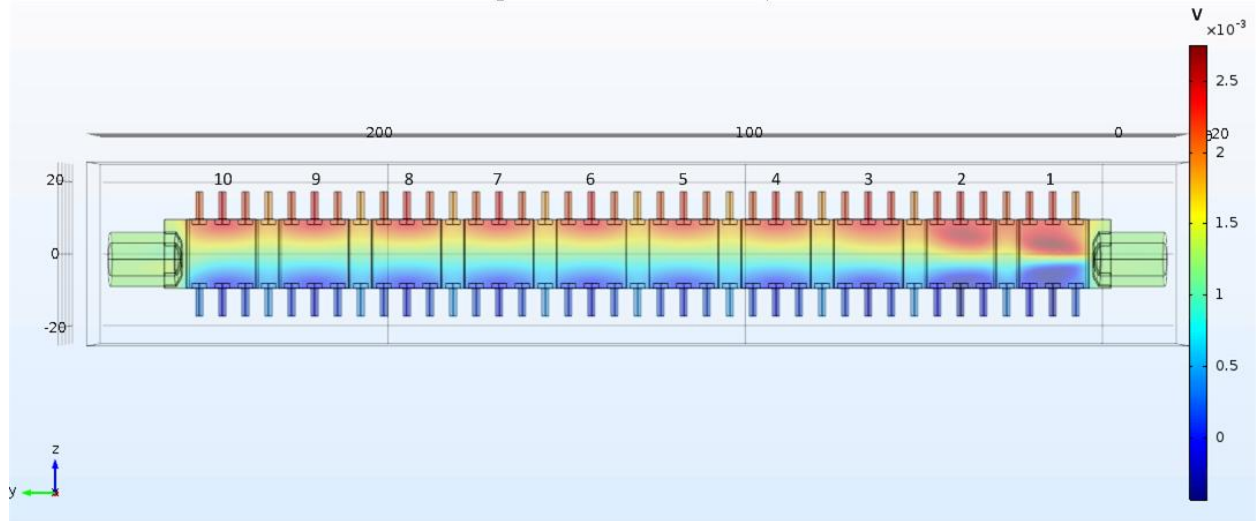
Figure 5.10. Electric voltage potential distribution within the generator center plane

Another way to visualize the induced voltage potential is through the line integral of electric field. Fig. 5.11 illustrates these integral results along the axis of each of the 10 main electrode pairs. Again, it can be seen that voltages are higher at the 1-3 electrode, due to increased velocity and flux density. The values resulting from the line integrals calculated for electrode pair 9 and 10 are also higher but not as profound. What can be observed additionally to the comments made for Fig. 5.11 is that electrode pairs 4, 6, 7 and 8 are giving the same voltage readings regardless of load, only changing with flow rate. On the other hand, it can be noted that the integral values resulting from electrode 5 are distinct for every single operating point simulated. Because the load is connected at this pair, the current drawn from the generator has its impact on the induced voltage through the internal resistance voltage drop. The largest drop is always observed for the 0.45 Ω resistances, because the current drawn is higher, as will be seen later. Higher currents yield higher voltage drops on the internal resistance. Therefore, the voltage resulting from the

integration at this specific pair, does not represent the induced voltage anymore, it represents the generator output voltage. The induced voltage at this point is comparable to the ones at pairs 4, 6, 7 and 8.
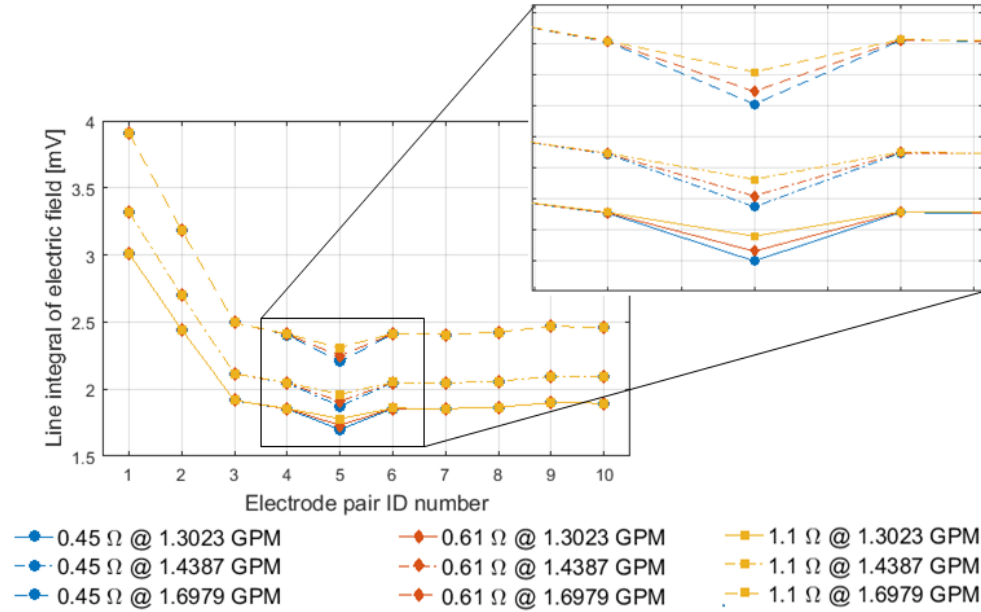
Figure 5.11. Line integral of electric field along each main electrode's axis line

The study of micro-level results is continued by looking at the induced current density. Fig. 5.12 contains the x and y component of the current density along the electrode axis of pair number 5. It can be seen that the current amplitudes are small and that the values are not significantly influenced by change in load. This is because these currents represent eddy currents, and not harvested currents due to the direction of the components. The z direction component on the other hand, oriented along the path prescribed by the induced electric field, can be seen in Fig. 5.13.
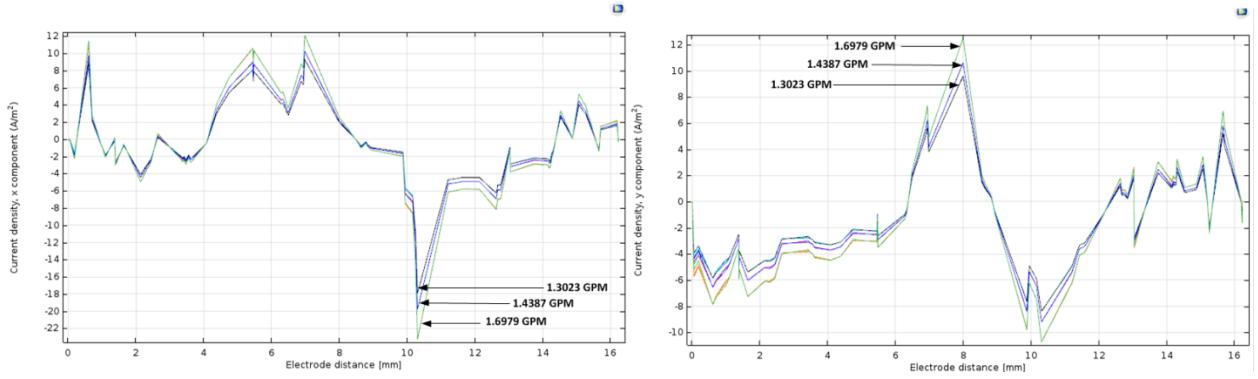
Figure 5.12. Current density components x and y plotted along the electrode axis of pair 5
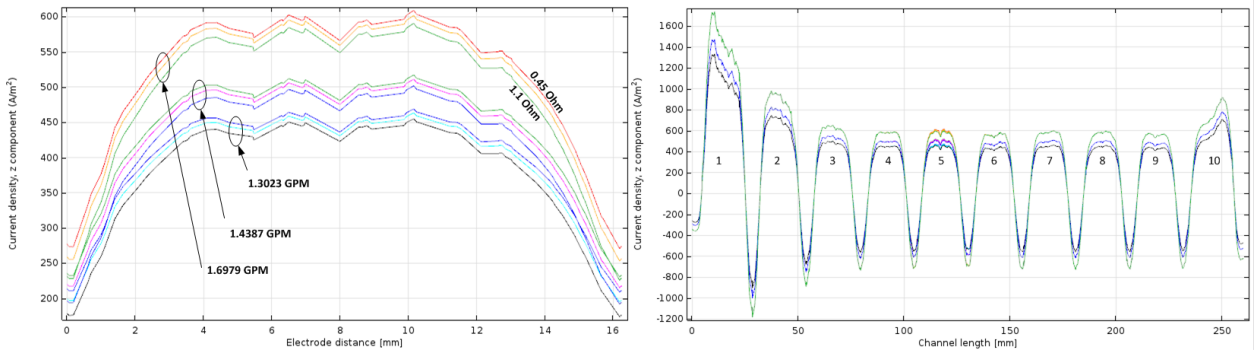
Figure 5.13. Current density component z plotted along the electrode axis of pair number 5 and the longitudinal center line of the generator

The z component of current density changes with speed and load and is between 10 and 30 times larger than the other components of the current density. This figure also illustrates the z component of the current density along the length of the channel. It can be observed that only in the region of fifth magnet pair, the current density changes with load, showing clearly at which electrode pair the load is connected. It can be concluded that the difference between pair 5 and 6 is the harvested current, meaning that the current density observed under the magnet pair 1 – 4 and 6 – 7 are solely eddy currents. Additionally, when studying the current density plot along the channel length (Fig. 5.13), negative currents can be noticed between the magnet pairs. These regions show that the eddy current loops close.

74
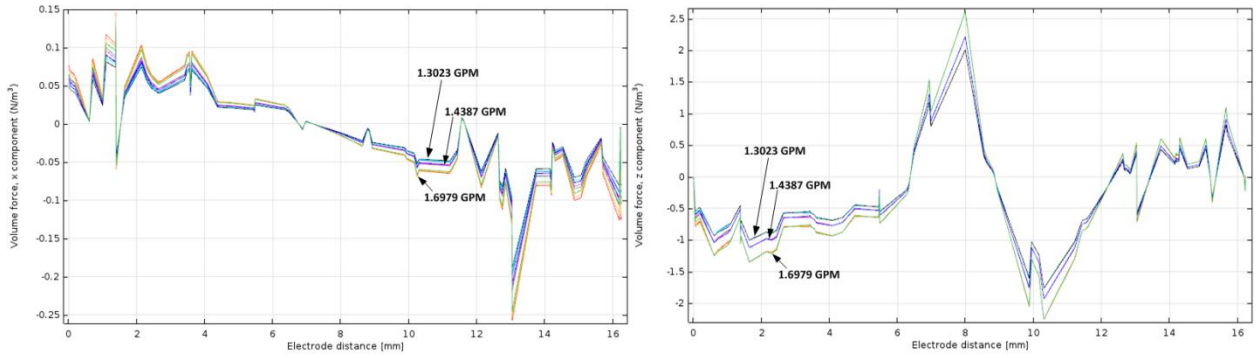
Figure 5.14. Lorenz force density component x and z plotted along the electrode axis of pair number 5.
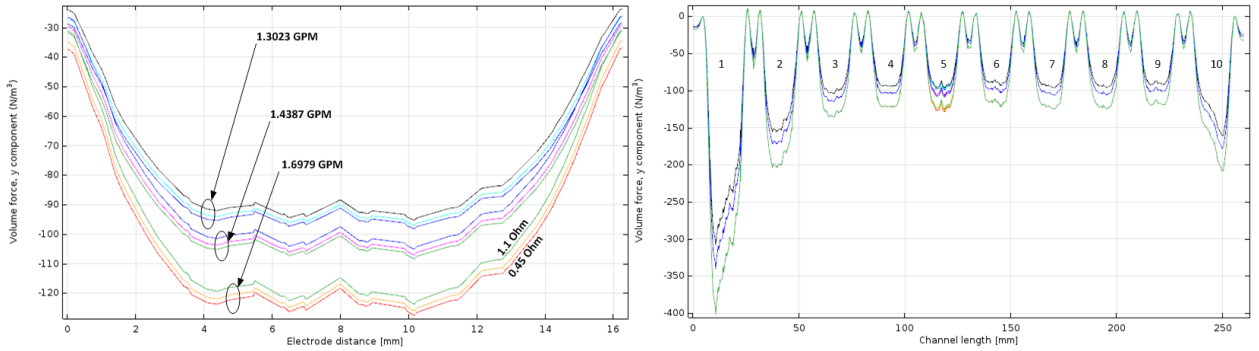
Figure 5.15. Lorenz force density component y plotted along the electrode axis of pair number 5 and the longitudinal center line of the generator

The next step of the analysis is addressing the changes in Lorenz force due to the current density changes. Figures 5.14 and 5.15 illustrate the force density components within the channel. It is obvious, at noted in Chapter 4 that the highest values are in the y direction. This is also the direction of flow, resulting that, if a negative sign in present, the Lorenz force opposed the fluid flow. Some change with load is noticeable in all force density components, but more so in the y component. As larger and load sensitive currents are induced in the z direction, both the x and y components reflect this to a certain extent, due to their relationship given by (4.12). In all three of the components, positive and negative force density values are present. Particularly the

75

areas between magnets are of interest, as this is where the eddy currents form closed loops and the direction of the current density reversed, reversing the Lorenz force direction with them.

From a thermal point of view, the same behavior is seen here as in the model presented in Chapter 4. No steep temperature gradient is detected in the simulation results (Table 5.2), as absorbed power levels are low, and resistive losses in the channel are minimal due to low currents. Fig. 5.16 shows the temperature distribution on the generator center plane. Two observations can be made. Firstly, the highest temperature can be found at the generators inlet, where induced voltage potential is the highest. Higher induced electric field results in a higher density of eddy currents (Fig. 5.13) and therefore more resistive losses are generated in this region. Secondly, the fluid behaves like a coolant to the generator. Because of its velocity, the moving fluid is cooler than the rest of the generator. Only very slow and stagnant portions of the Gallium are heating up.
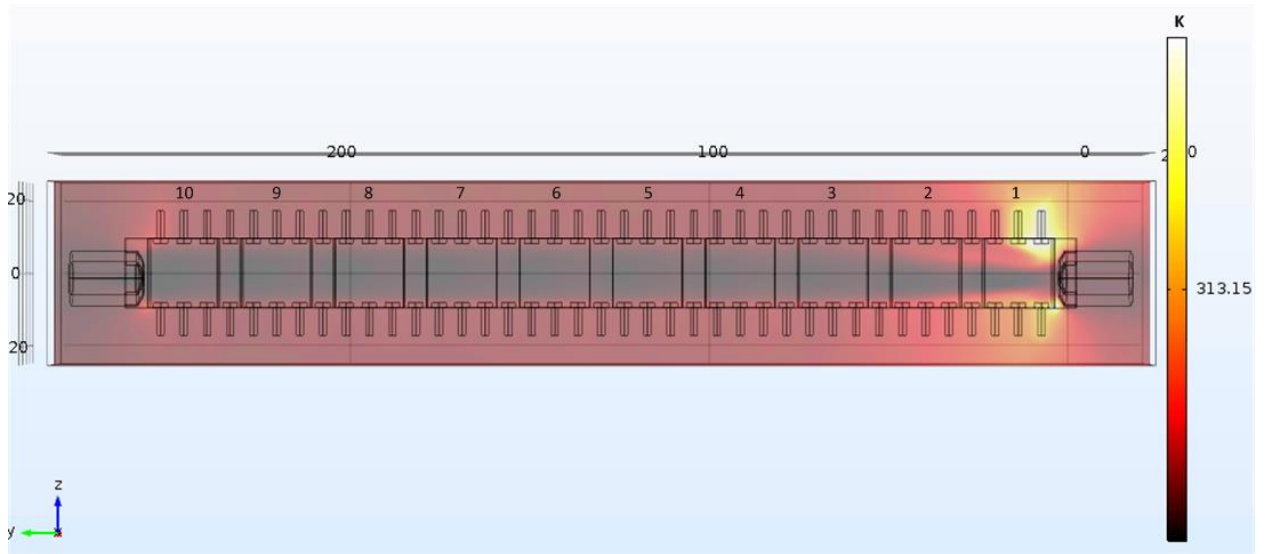
Figure 5.16. Temperature distribution for the MHD generator with a 0.45 Ω load and 1.6979 GPM

Table 5.2. Maximum and minimum Gallium temperatures for different operating points

Load [Ω]	Flow rate [GPM]	Maximum temperature [°K]	Minimum temperature [°K]
0.45	1.3023	313.1500302	313.1500192
0.45	1.4387	313.1500321	313.1500197
0.45	1.6979	313.1500335	313.1500184
0.61	1.3023	313.1500424	313.1500315
0.61	1.4387	313.1500293	313.1500169
0.61	1.6979	313.1500443	313.1500292
1.1	1.3023	313.1500384	313.1500274
1.1	1.4387	313.1500406	313.1500283
1.1	1.6979	313.1500422	313.1500271

5.3.2 Macro-level Simulation and Experimental Results Comparison

Fig. 5.17 represents the oscilloscope reading of the experimental measurement of load current over the three experimental resistors mentioned earlier as well as the three studied flow rates. The trend observed from the mathematical model stands true: an increase in fluid velocity (equivalent to an increase in flow rate, as generator diameter is not modified) results in an increase in load current. This is explained by the increase in induced electric field, as fluid velocity increases. Additionally, an increase in load resistance decreased the current output, as the induced electric field remains unchanged.

The offset of the captured data is removed and the information is filtered. After averaging the data points for each operating condition, the results are compared to the load currents obtained through the simulation process described in Chapter 4 with adaptions detailed in this Chapter. Fig. 5.18 overlays the experimental and simulation results. Two simulations are completed: one assuming that the flow meter operates with perfect accuracy (0 FS error) and a second one considering a reading with a -2 FS accuracy. Table 5.3 records the error for both situations using

(5.2). It can be seen that the results are in good agreement. The simulation is overestimating the experiment by roughly 5 to 36% in the first case, and -5 to 27% in the second. The points affected most by error are the lower speed operating points. Additionally, the accuracy loss causes the highest reduction in value to the 0.45 Ω simulation results, dropping in absolute value roughly 0.4 mA in comparison to the 1.1 Ω simulation, which dropped only 0.1 mA. This suggests that high loading conditions are more robust to flow meter reading inaccuracy.
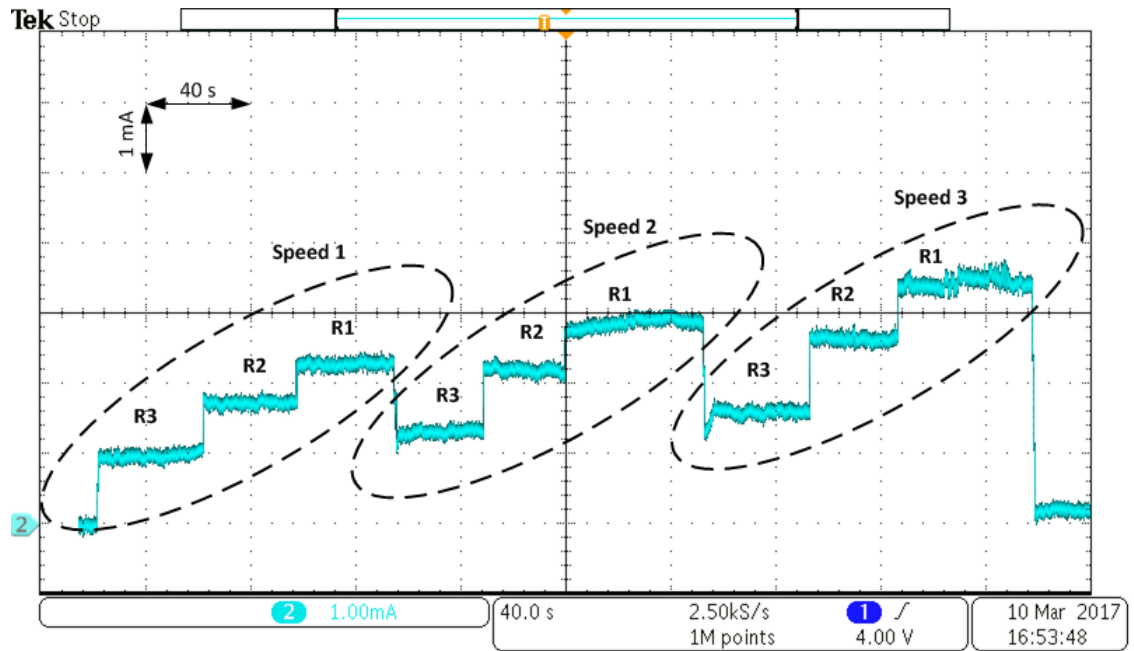
Figure 5.17. Experimental load current reading

$$e = \frac{I_{exp} - I_{sim}}{I_{sim}}$$

(5.2)
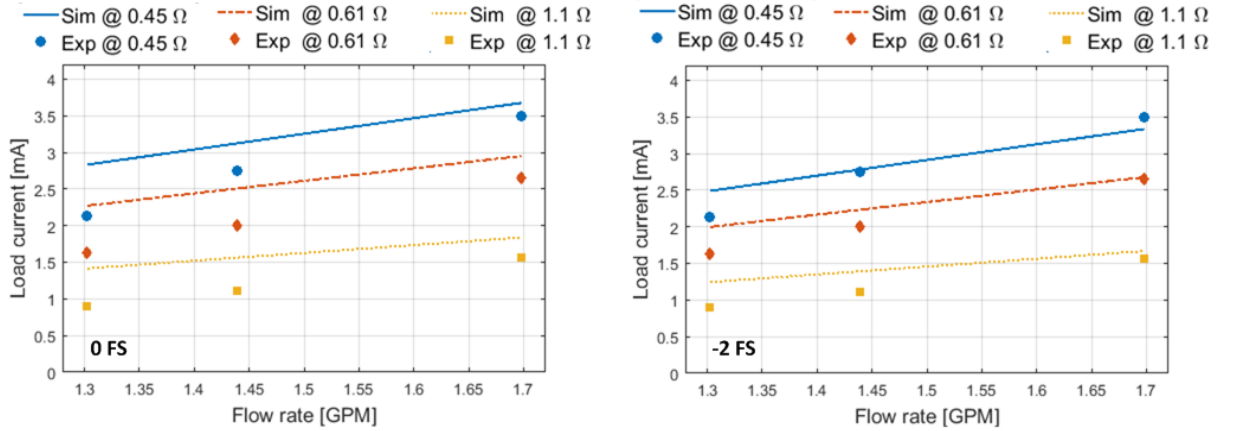
Figure 5.18. Experimental and simulation current for 0 FS and -2 FS flow meter accuracy

Table 5.3. Error

		1.3023 GPM	1.4387 GPM	1.6979 GPM
0.45 Ω	*e %*	*-24.72*	*-11.99*	*-4.81*
	e % @ -2 FS	**-14.34**	**-1.16**	**+4.92**
0.61 Ω	*e %*	*-28.15*	*-19.91*	*-10.31*
	e % @ -2 FS	**-18.25**	**-10.05**	**-1.14**
1.1 Ω	*e %*	*-35.89*	*-28.70*	*-14.99*
	e % @ -2 FS	**-27.06**	**-19.92**	**-6.30**

As no micro-level results are available for the experiment, efficiency cannot be determined accurately. Nonetheless, a rough approximation can be made. Instead of the induced power, which is obtained in the simulation by integrating the electric field, the electric output power can be used. An issue arises when trying to determine the hydraulic power of the fluid. The fluid power can be equated to the electric input power of the pump used to accelerate the Gallium, but this is an overestimation of the fluids kinetic power. The pump efficiency is unknown. Additionally, there are pressure drops throughout the Gallium flow circuit which are not considered in the simulations such as bends in the pipes, diameter changes from piping to flow meter, flow meter to pipe, and pipe to pump. Furthermore, the length of the circuit is longer and therefore the volume of gallium moved is larger in reality than in the simulation, where only the

79

generator block was modeled. Nonetheless, experimental efficiency is calculated using the input power of the electric pump as the hydraulic power of the fluid, for an estimated compassion. Again, it has to be kept in mind that this experimental efficiency is not representative due to the inaccuracies mentioned. Table 5.4 contains the data in comparison. The efficiency of the simulated generator is calculated considering 0 FS accuracy of the flow meter, using the method outlined in Chapter 4.

Table 5.4. Hydraulic power and efficiency for simulation and experiment

Load [Ω]	Flow rate [GPM]	Hydraulic Power [W]		Efficiency [%]	
		Simulation	Experiment	Simulation	Experiment
0.45	1.3023	10.46	27.12	3.45e-5	7.53e-6
0.45	1.4387	14.08	37.8	3.12e-5	8.99e-6
0.45	1.6979	23.09	58.4	2.63e-5	9.43e-6
0.61	1.3023	10.46	27.12	3.01e-5	5.99e-6
0.61	1.4387	14.08	37.8	2.72e-5	6.50e-6
0.61	1.6979	23.09	58.4	2.30e-5	7.31e-6
1.1	1.3023	10.46	27.12	2.11e-5	3.34e-6
1.1	1.4387	14.08	37.8	1.91e-5	3.61e-6
1.1	1.6979	23.09	58.4	1.61e-5	4.60e-6

Although of the same order of magnitude, the electric input power is roughly 3 times larger than the simulated hydraulic power. Again, this can be explained by the pump efficiency as well as pressure drops in the system outside the simulated generator section. It can be observed that for both simulated and experimental results, the efficiency drops as load increases at constant flow rate.

5.4   Summary

The purpose of this Chapter was to generate a 3D Multiphysics model, which accurately represents the prototype PMLM MHD power generator. Needed adaptations were discussed as

well as their implementation. These include mechanical adaptations such as geometry considerations and flow meter accuracy but also modifications of electromagnetic nature, such as the inclusion of the measured harness resistance and consideration of the thermally induced reduction in remanent flux density of the excitation. Micro-level results are discussed in detail. Lastly, macro-level simulation results are compared to the experimental results of load current, and a good agreement is found. Efficiency values are also compared and similarities in trends were detected.

CHAPTER 6

OPTIMAL DESIGN CONSIDERATION AND LM MHD APPLICATION

Variation of output with design parameters was discussed in Chapter 3. A drawback of this discussion was that it is based on the mathematical model derived in the same Chapter, but is nonetheless a fair indicator of variation trends. The use of the mathematical model results in an inaccuracy in values compared to the prototype. Additionally, this model has the limitation of the inability to predict flux density in the channel, when channel width or magnet thickness change. This is because flux density in the channel is considered an input variable in the mathematical model.

Therefore, this Chapter analyzes trends in current and efficiency output variation using the 3D multiphysics model. Besides being more accurate in its representation of the PMLM MHD phenomena, it is also able to consider the remanent flux density of the permanent magnets as an input variable, providing a more realistic method to model the excitation. This Chapter provides sensitivity studies of the generator behavior with changing design parameters as well as a summary of observed trends and recommendations for future designs of permanent magnet excited liquid metal magnetohydrodynamic power generators.

Additionally this Chapter offers details on a possible application for the liquid metal magnetohydrodynamic power generation: thermal to electrical energy conversion. Needed conditions and additions to the MHD generator system to complete the conversion process from thermal to electrical energy are discussed. Furthermore, a comparison to an existing thermal to electrical energy conversion device is provided.

6.1   Generator Output Design Considerations

The design target, or targets when using a multi-objective approach, is highly dependent on the application considered for the MHD generator, but commonly, a high power density and efficiency are desired. These two items are measures of how well resources are put to use in the generation process. Power density relates the output power of the generator to its overall size, whereas efficiency considered the output power in relationship to the absorbed input power. Therefore, in this design study, the focus will be solely on the macro-level results of the 3D multiphysics simulations, namely load current and efficiency.

The main goal of the study presented in here is to gain better understanding of the effect that design parameters have on the generator performance, measured in load current output and efficiency. This insight will aid future design efforts of LM MHD generators, as it identifies the most impactful parameters, as well as their effect on the generator output. The design parameter can be divided into three categories related to: geometry, working fluid, and excitation. Table 6.1 contains the base values used for all model variables. This base model represents the 3D multiphysics model used in Chapter 4 to illustrate the simulation process, and follows all physics implementations described there. All comparisons are conducted for three average inlet speeds: 0.1, 0.5, and 1 m/s.

Table 6.1. Base parameter values for sensitivity study

d [mm]	δ [mm]	w [mm]	l [mm]	ρ [kg/m^3]	σ [S/m]	μ [Pa s]	R_L [Ω]	R_H [Ω]	B_r [T]
38.1	1.4	5	19.05	6087.66	$3.579 \cdot 10^6$	0.00194	0.5	0.137	1.23

6.1.1 Generator Geometry

This Section considers the channel width and height design variables. Change in channel dimensions has an impact on flux density distribution which is impossible to model using the mathematical method, as latter considers an average value within the channel.

Change in channel width is implemented with the following considerations. Channel width changes from 4.5 to 5.5 mm with a 0.5 mm increment. The distance between magnets and channel is maintained at 1 mm as in the original model. This means that the magnets are moved in each simulation further away from each other, affecting the intensity of the excitation. Another change that channel width variation brings along is a change in the hydraulic diameter of the flow problem. Fig. 6.1 illustrates the change in load current and efficiency of the generator model with changing channel width.
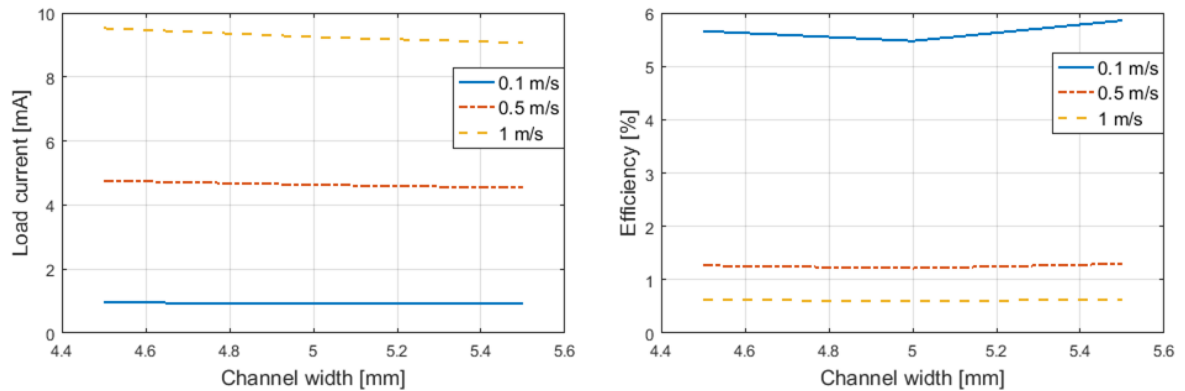
Figure 6.1. Change in load current and efficiency with variable channel width

It can be noticed that an increase in channel width decreases load current. This is due to the reduction in excitation, as the remanent flux density of the magnets is kept constant, but the distance increased. The drop in load current is more pronounced at higher flow speeds. In the case of efficiency, the increase in width initially causes a drop, but after a threshold, efficiency

increases again. This is mostly visible at lower speeds. This nonlinear behavior can be lead back to the fact that channel width affects all elements of the efficiency equation: output power, induced power, and mechanical input power.

Channel height is analyzed by simulating several generators of various channel heights (19.05, 28.58, and 38.1mm), but maintaining the magnet height constant at 38.1 mm. This has the results that, even though a channel is shorter than the respective excitation, it is located in a more advantageous position regarding flux density distribution uniformity. As the channel width before, the channel height also affects all three of the power elements considered in the efficiency derivation: electric output power, induced power, and mechanical input power. The results are of the height variation can be seen in Fig. 6.2.
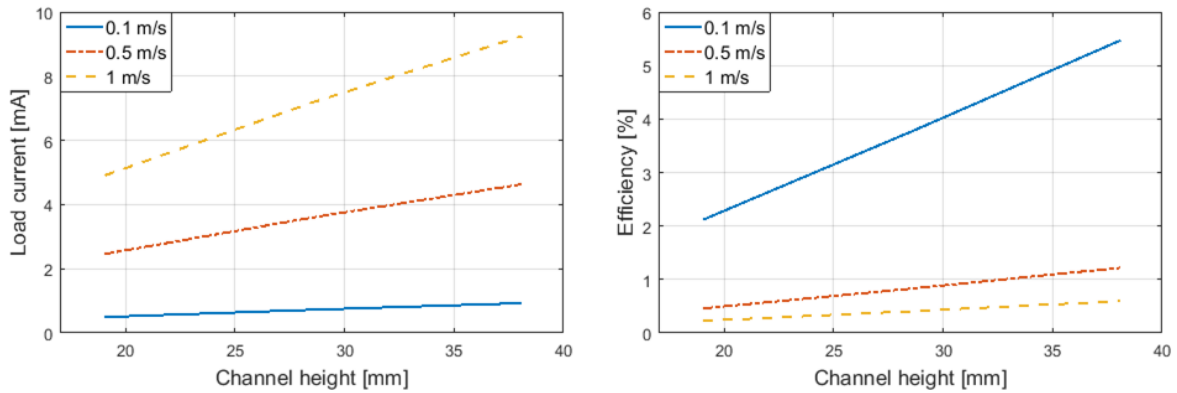
Figure 6.2. Change in load current and efficiency with variable channel height

Both efficiency and load current rise as channel height increases. Electrode distance, which is directly related to the channel height, has a big impact on the induced electric field in the generator, as it results in more moving fluid being exposed to the excitation. The increase in efficiency indicates that the gains in electric output power are larger than the rise in mechanical input power caused by the channel height increase. In comparison to the channel width, channel

length is a better choice when optimizing the geometry of the generator, as it has a more profound effect on efficiency.

6.1.2 Working Fluid Properties

Studying the effects of working fluid properties is useful when selecting a working fluid for the generator. The properties analyzed in this Section are fluid density and electric conductivity. It can be seen from Fig. 6.3 that density has no effect on generator current output. This is due to the simulation settings. The average inlet velocity is fixed, regardless of the generator properties. And because density does not have an effect on the electrical physics, output current does not change. Nonetheless, it has to be kept in mind density does affect the Reynolds number which dictates the physics selection of the flow problem: laminar or turbulent. Because all densities considered are smaller or equal to the density of Gallium, all Reynolds numbers are below the threshold, maintaining the flow laminar in nature. With a constant current output it is expected that efficiency drops, as illustrated in Fig. 6.3. Density has a significant impact on the mechanical energy needed to maintain the fluids speed. Mechanical input power increases as density increased. Therefore, with a constant induced and electric output power, efficiency drops.

When analyzing the changes caused by variations in electric conductivity, only electrical physics are affected. An increase in electric conductivity results in a decrease of internal resistance. Lower voltage drops on the internal resistance cause a higher generator output voltage, even when velocities are constant, and thus an increase in load current. As observable in Fig. 6.4, after a certain point, the internal resistance becomes negligible and the output current stops to increase. The conductivities used in this study are the conductivity of Gallium and its 10 and 100 times multiples ($3.579 \cdot 10^6$, $3.579 \cdot 10^7$ and $3.579 \cdot 10^8$ S/m respectively). Generally

speaking, selecting materials with higher electrical conductivities is beneficial to increase the generators current output, but only up to a certain point. This point will critical value depends on the geometry of the generator channel as this influences the internal resistance.
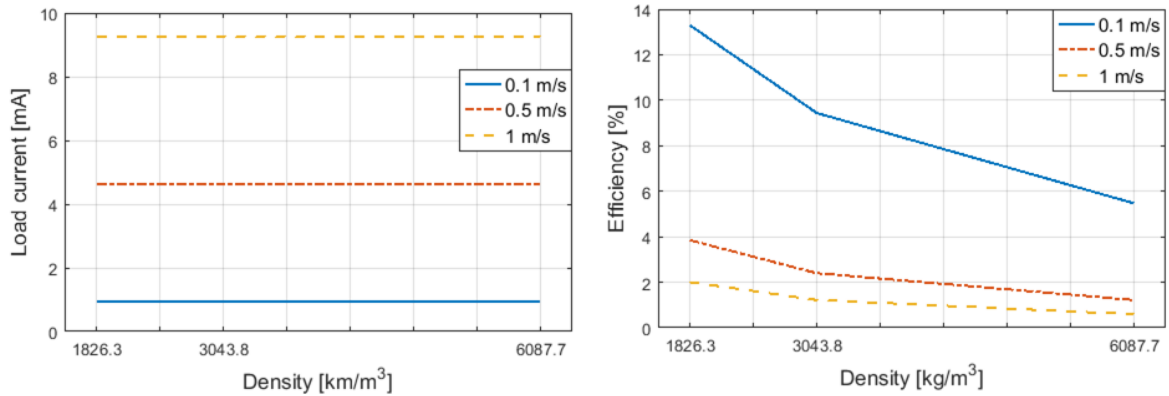
Figure 6.3. Change in load current and efficiency with working fluid density
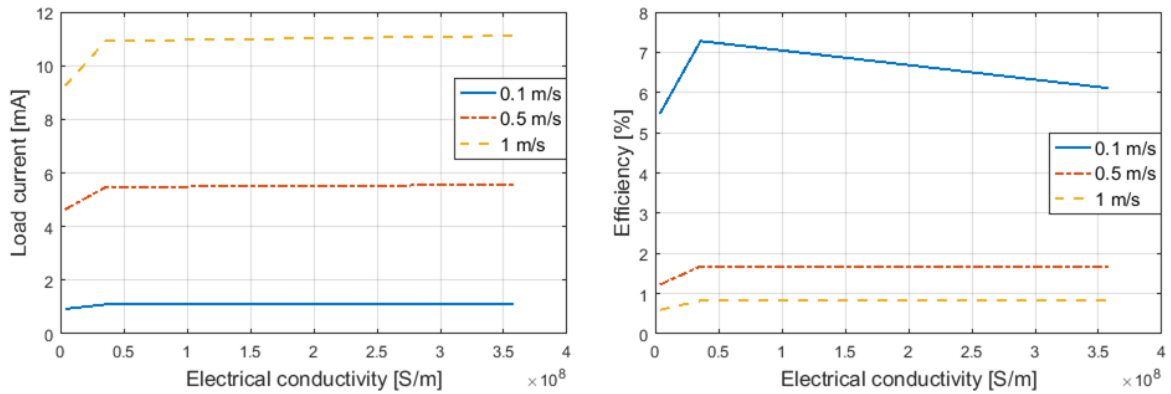
Figure 6.4. Change in load current and efficiency with working fluid electric conductivity

When looking at efficiency, a similar pattern is noted, as the mechanical input is unaffected by the changes in electric conductivity. Efficiency increases until the output voltage saturates. Additionally, an efficiency drop is notable for 0.1 m/s flow. This is due to the increase in induced power, which reduces efficiency. Due to the nature of the generator, electric current output of the generator cannot increase without an increase in induced power. As induced power is the

opposing force to the flow, an increase in output current leads to an increase in mechanical input power. Therefore, after the electrical output saturates, efficiency drops.

6.1.3 Excitation

The possibility to modeling of excitation using the remanent flux density of the magnets, provided by manufacturers, and not by relying on an average value assigned to the generator channel, is a significant advantage of the 3D multiphysics simulation. To take advantage of this possibility, two design parameters are studied in this Section. Firstly, the impact of magnet strength on the generator performance is analyzed. Secondly, the effect of magnet thickness with maintained remanent flux density.

The strength of a magnet in simulation is given by their B_r remanent flux density. Simulations are conducted with magnets for 0.615, 1.23 and 2.46 T B_r respectively. It is obvious that an increase in excitation will increase the current output, as induced electric field is directly depended on the flux density within the channel. Fig. 6.5 illustrates this fact. It can be observed that the rate of load current increase is larger when fluid velocities are higher. Efficiency also increases with excitation, because the mechanical input needed to maintain the fluid in motion does not change with the increasing load current.

Moving on to the variations induced by magnet thickness, it becomes clear that to achieve realistic simulation results it is imperative to consider magnet dimensions, alongside with magnet strength. This detail of modeling is impossible to be captured with a solely mathematical approach. The B_r used is 1.23 T and magnet thicknesses explored are 2.175 mm, 3.175 mm, and 4.175 mm respectively. Channel width and distance between channel and magnet are kept constant. The load current and efficiency results can be seen in Fig. 6.6.
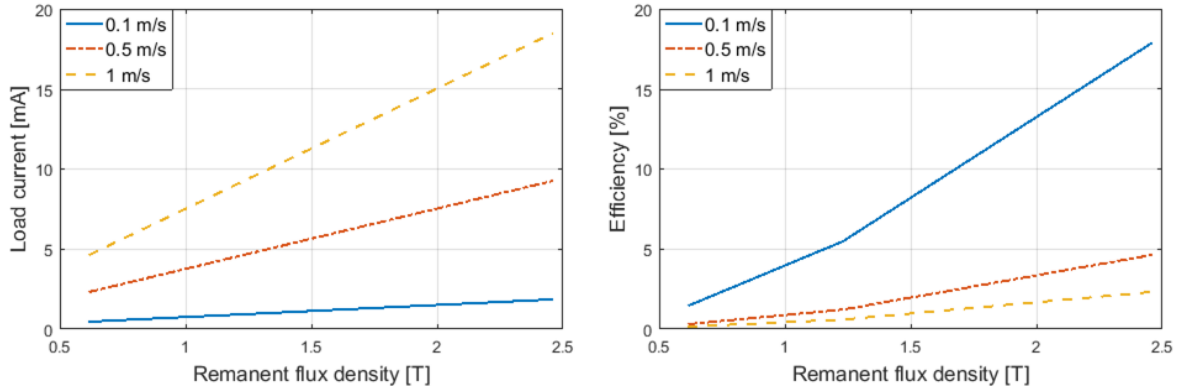
Figure 6.5. Change in load current and efficiency with remanent flux density

Both current and efficiency increase with the increase in magnet thickness. This indicates that the flux density values in the channel increase. Current increases due to the rise experienced in the induced electric field caused by higher average flux density and efficiency increases because the mechanical input power needed to maintain the fluids speed is constant whereas the output power increases. It is true that the induced power increases as well, but this power is one or two orders of magnitudes smaller than the mechanical input, dependent on simulation conditions and has therefore a smaller impact overall on efficiency.
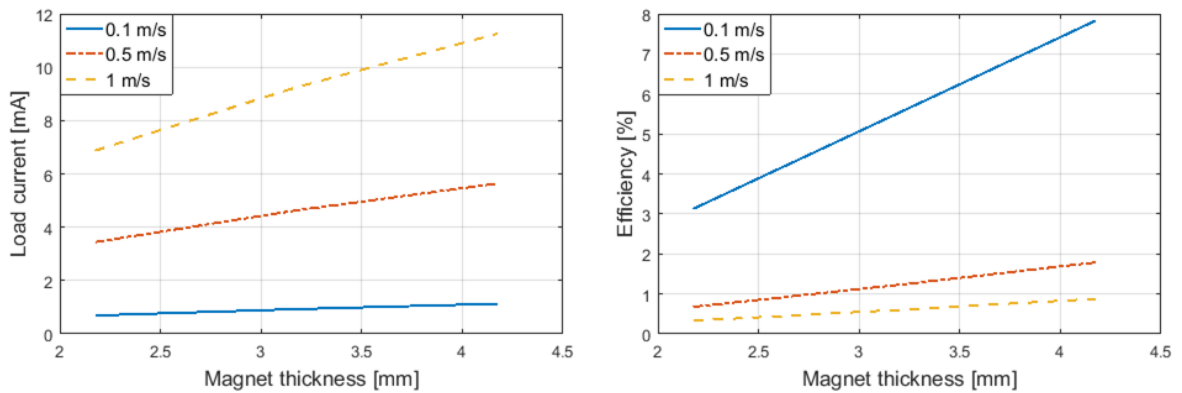
Figure 6.6. Change in load current and efficiency with magnet thickness

6.2   Design Guidelines

From the studies conducted and analyzed in the previous Section, conclusions can be formed which will act as design guidelines for future prototype designs. A trend visible in all results is that an increase in fluid velocity always increases the generators current output but decreases efficiency. This is because on one hand, an increase in fluid velocity increases the induced electric field, but on the other hand, it also requires a higher mechanical power input to maintain this velocity, therefore causing the efficiency to drop. This has to be kept in mind during the optimization process, when assigning priority to one gain (power output) over the other (efficiency) in the selection of the operating point.

For the fluid channel design, it is recommendable to maintain channel width constant or as small as possible, to take full advantage of the available excitation. Channel height can be increases as it has a positive effect on current and efficiency output, but should not exceed the height of the available magnets. Theoretically, channel height can be extended even further then shown in these simulations, but when designing a permanent magnet excited LM MHD generator, the designer has limited option in permanent magnet dimensions.

When selecting the working fluid, density and electric conductivity have to be carefully considered. A low fluid density is best, as it increases efficiency of the generator, without deteriorating the electrical performance (i.e. electric current output) of the generator. Higher electric conductivity is generally beneficial to both electrical current output as well as efficiency, until a certain value which is geometry depended.

Lastly, from this study it becomes obvious that both remanent flux density and magnet thickness increases result in a rise of output current and efficiency of the generator. The selection

of the excitation will therefore depend on the intended power density of the generator as well as availability of permanent magnets on the market and design cost constraints.

6.3 Application Case Study: Thermal to Electrical Energy Conversion

6.3.1 Motivation

The demand for diversification of electrical energy sources increases as more reliability and flexibility are expected from the electric grid, especially micro-grids. Furthermore, the socio-economic climate is driving research towards renewable and sustainable methods of electrical power generation. Liquid metal magnetohydrodynamic power generation can be a part of this energy mix, because it has no exhaust gases and the metal is recirculated in the generator system.

In its current form, the MHD generator described in the previous Chapters, is a mechanical to electrical energy converter. Natural mechanical power sources, such as ocean currents, river streams, and geothermal turbines can be used to drive the Gallium through the channel. Ocean currents for instance, can reach speeds between 0.05 and 0.61 m/s [31], dependent on depth and season of the measurement as well as geographic location. These speeds are within the rage of the simulations conducted in this work.

To maintain the Gallium liquid with minimal additional energy input, it is advisable to immerse the generator in warm ambient such as inside of data centers, cooling towers of power plants or simply outdoors in generally warm climates. This will increase the efficiency, as no external thermal energy is needed. Because of this immersion, the generator will be in close proximity to low temperature waste heat sources such as exhaust gasses from other energy conversion processes or HVAC systems, and capturing this thermal energy is a potential niche

for MHD power generation. Because the liquid metal flow circuit it is closed circulation, and no moving mechanical components are involved, the generator system can be built ruggedly and will need minimal maintenances. It becomes a practical solution to harvest waste heat from locations which are difficult to access. But, in order to complete the thermal to electrical energy conversion cycle, the MHD generator presented in this work has to be combined with a thermal to mechanical conversion device.

6.3.2   Thermal to Mechanical Energy Converters

Two possible candidates for thermal to mechanical energy converters are identified: steam turbines and Stirling engines. In order to use these devices for low temperature waste heat harvesting, adaptations are necessary. The steam turbine has to be designed to operate with fluids which have a low temperature vaporization temperature, such as Butane instead of the more commonly used water vapor.

The other device for the thermal to mechanical energy conversion is the Stirling engine, which generates mechanical power through the compression of gas between a hot and cold plate of a piston cylinder. Low temperature difference Stirling engines have been researched [32], [33] and show potential. However, because the thermal to mechanical energy conversion efficiency is limited by the Carnot cycle, a higher temperature difference would yield better efficiencies. Stirling engine efficiency is given by (6.1), where T_h and T_c are the temperatures of the hot and cold plate in degree Kelvin. Fig. 6.7 illustrates efficiency curves for potential low temperature difference plate temperatures.

$$\eta = \frac{T_h - T_c}{T_h} \ 100\%$$
(6.1)
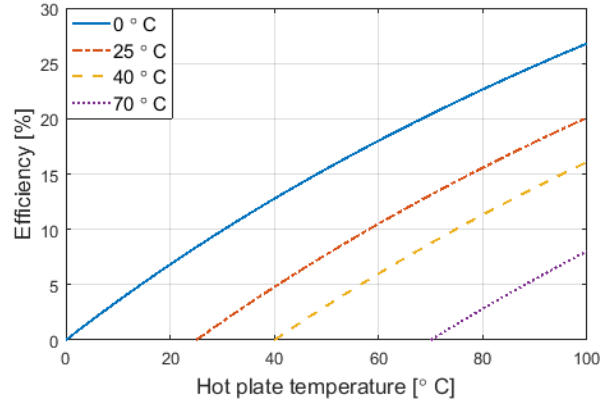
Figure 6.7. Efficiency lines for various hot and cold plate temperatures

Varying the hot plate temperature between 0°C and 100°C, Fig. 6.7 shows the positive efficiencies reached for four different cold plate temperatures: 0°C, 25°C, 40°C, and 70°C respectively. It can be clearly seen that efficiency will vary with ambient conditions. Furthermore, efficiencies are higher for lower hot plate temperatures compared to higher hot plate temperatures, when the temperature difference $(T_h - T_c)$ is the same.

6.3.3 Overall Efficiency and Comparison to Other Technologies

As seen in Chapter 3 and 4, efficiency of the MHD generator is dependent on many factors such as fluid speed, excitation strength, material properties, and generator geometry. The efficiency of the Stirling engine is contingent on the available thermal potential, i.e. the temperature on the hot and cold plate. Nonetheless, Table 6.2 illustrates the overall efficiency for multiple cold and hot plate temperatures as well as excitations. The hot plate as well as the generator channel are exposed to the waste heat, and have therefore the same temperature. MHD efficiencies in the table are taken from Table 4.6, and determined with the simulation model described there. The overall efficiency is calculated with (6.2).

93

$$\eta_{overall} = \frac{\eta_{MHD}*\eta_{Stirling}}{100} \qquad (6.2)$$

Table 6.2. Overall efficiency of the thermal to electrical energy conversion process

Cold plate temperature [°C]	Waste heat and hot plate temperature [°C]	Remanent flux density [T]	MHD efficiency [%]	Stirling efficiency [%]	Overall efficiency [%]
-10	40	1.35	6.12	15.97	0.98
-10	100	6.75	52.19	29.48	15.38
-10	150	13.5	68.17	37.81	25.78
0	40	1.35	6.12	12.77	0.78
0	100	6.75	52.19	26.80	13.99
0	150	13.5	68.17	35.45	24.17
10	40	1.35	6.12	9.58	0.59
10	100	6.75	52.19	24.12	12.58
10	150	13.5	68.17	33.09	22.55

The resulting overall efficiencies are between 0.59 and 25.78%, dependent on cold plate and waste heat temperatures and excitation. The hot and cold plate temperatures illustrate that this device is versatile, as even a waste heat of 40°C can be harvested by the Stirling engine with 9.58 to 15.97% efficiency. For instance, the overall efficiency of data centers can be raised, when installing MHD-Stirling systems, especially during winter time. The cold plate is placed outside the center whereas the hot plate and MHD channel are placed inside, with the goal to harvest the thermal energy emitted by the resistive losses of the datacenter switches. Instead of losing all of the thermal energy, the MHD-Sterling system can recuperate and feedback electric energy into the datacenter grid.

The thermocouple, a thermal to electric energy conversion device, displays efficiencies between 2 and 5% [34]. The MHD-Stirling system presents higher efficiencies and is furthermore designed for power generation. Thermocouples are mostly used for sensor applications. Therefore, if designed appropriately for the specific application,

magnetohydrodynamics is a good candidate for renewable energy diversification and waste heat harvesting.

6.4   Summary

In this Chapter, the sensitivity analysis was conducted to assess the impact of design parameters on the output current and overall efficiency of the liquid metal MHD power generator multiphysics simulation. The multiphysics model was used for this study, as it allows for more accurate simulation results as well as the ability to model permanent magnets through remanent flux density, permitting the inclusion of realistic magnetic field distributions in the generator analysis. The conclusions are summarized to a set of design guidelines which will prove beneficial in future attempts of optimal design of PMLM MHD or simply LM MHD generators.

This Chapter furthermore illustrated possible applications for the MHD power generation and its use together with Stirling engines, to complete the thermal to electrical energy conversion process. Harvesting energy from waste heat can be useful to increase the overall energetic efficiency of buildings and power plants. It was shown that a well-designed MHD-Sterling system is more efficient than the commonly used thermal to electrical energy converters, the thermocouples.

CHAPTER 7

CONCLUSIONS

7.1   Summary

The overarching idea conveyed by this work is that liquid metal magnetohydrodynamic generator is a feasible renewable energy solution. To illustrate this point, after the general introduction to the work in Chapter 1, a detailed description of the generators components was given in Chapter 2. Chapter 3 provided the physical background of the MHD generation phenomenon as well as a mathematical model describing the PMLM MHD generators behavior under various conditions. A comprehensive 3D multiphysics simulation was provided in Chapter 4, which included a comparison to the mathematical modeling results as well. To validate the simulation method, Chapter 5 modeled a PMLM MHD generator prototype. Modeling and experimental results of the prototype were compared and found to be a good match. Therefore, the modeling process was successful. Then, Chapter 6 analyzed the effect of design variables on the simulation model output and provides guidelines for future optimal design of the LM MHD generator. Additionally, Chapter 6 demonstrated how MHD can be used to harvest waste heat.

The following conclusions can be drawn. Magnetohydrodynamic power generation is a complex technology, as multiple branches of physics are involved, but has high potential for renewable energy applications. The mathematical model is less accurate compared to the 3D multiphysics simulation, due to the assumed simplifications. Multiphysics simulation proved to be an indispensable tool in MHD generator design, as many factors interplay in the generation

process, affecting both current output and efficiency. The use of MHD in thermal to electrical energy conversion applications is an attractive solution for waste heat harvesting.

7.2 Contributions

The contributions of this work are summarized in the points below.

- Display of possible implementations of the main generator elements and their attached advantages and disadvantages.

- Derivation of a mathematical model of a liquid metal magnetohydrodynamic power generator.

- Construction of a comprehensive multiphysics model of the LM MHD generator.

- Experimental verification of the multiphysics model through comparison to results obtained by the first prototype of a permanent magnet excited liquid Gallium MHD power generator.

- Study of the model sensitivity to design parameters as well as the observation and summary of design guidelines.

- Proposition and efficiency analysis of a thermal to electrical energy conversion system, which includes MHD as a component, for waste heat harvesting.

7.3 Future Work

Valuable future work can be divided into three types: theoretical, modeling, and experimental improvements and addition. Firstly, to add to the theoretical section of the PMLM MHD study, the mathematical model can be improved. Such improvements would include the introduction of

an accurate description of flow and flux density distribution, providing a more realistic analytical model.

Secondly, on the modeling side of this study, it will be beneficial to study the effect of connecting multiple loads to one generator, using distinct sets of electrode pair. This study can include for instance the connection of different sized loads and their effect on the micro-level behavior of the generator.

Lastly, experiments can be improved by building a prototype with tighter quality control on the permanent magnets as well as the inclusion of pressure measuring devices, for a more accurate efficiency.

REFERENCES

[1] R. R. Bennett, "Planning for power – a look at tomorrow's station sizes," *IEEE Spectrum,* vol. 5, no. 9, pp. 67-72, 1968.

[2] R. Hawley, "Magnetohydrodynamic power generation," *Students' Quarterly Journal,* vol. 31, no. 122, pp. 63-69, 1960.

[3] D. H. Marquis, "Potential industrial application of magnetohydrodynamics," *IEEE Transactions on Industrial Electronics,* vol. 1, no. IE-10, pp. 85-90, 1963.

[4] G. Lipscombe, J. Penny, R. Leyser and H. J. Allison, "Water under the bridge," *Journal of Physics Special Topics,* vol. 13, no. 1, 2014.

[5] W. D. Jackson, "Magnetohydrodynamic power generation - a status report," *Electronics and Power,* vol. 10, no. 8, pp. 258-263, 1964.

[6] W. D. Jackson and E. Levi, "Magnetohydrodynamic power generation: program planning and status," *IEEE Transactions on Power Apparatus and Systems,* vol. 6, no. PAS-98, pp. 2022-2029, 1979.

[7] A. R. Kantrowitz, T. R. Brogan, R. J. Rosa and J. F. Louis, "The magnetohydrodynamic power generator-basic principles, state of the art, and areas of application," *IRE Transactions on Military Electronics,* Vols. MIL-6, no. 1, pp. 78-83, 1962.

[8] M. W. Thring, "Magnetohydrodynamic power generation," *Journal of the Institution of Electrical Engineers,* vol. 8, no. 89, pp. 237-241, 1962.

[9] A. Geri, G. M. Veca and A. Salvini, "Performance evaluation of MHD generators: the lumped parameter model and its validation," *IEEE Transactions on Energy Conversion,* vol. 14, no. 4, pp. 1224-1229, 1999.

[10] X. Wang, D. Ye and F. Gu, "Inverstigation of the characteristics of MHD power generation by a corona jet across a magnetic field," *IEEE Transactions on Plasma Science,* vol. 36, no. 1, pp. 299-304, 2008.

[11] T. Zhu, Y. Li, Y. Li, B. Zhang and F. Chen, "Supersonic magnetohydrodunamic power generation system and its preliminary experiment," in *International Conference on Intelligent System Design and Engineering Application*, Sanya, 2012.

[12] M. Tanaka, Y. Aoki, L. Zhao and Y. Okuno, "Experiments on high-temperature Xenon plasma magnetohydrodynamic power generation," *IEEE Transactions on Plasma Science,* vol. 44, no. 7, pp. 1241-1246, 2016.

[13] E. S. Pierson, H. Herman and M. Petrick, "Conceptual design of a coal-fired retrofit liquid-metal MHD power system," in *Third Beer-Sheva International Seminar in Magnetohydrodynamic Flows and Turbulence*, Beer-Sheva, 1981.

[14] X.-D. Niu, H. Yamaguchi and X.-J. Ye, "Characteristics of a MHD power generator using a low-melting-point Gallium alloy," *Electrical Engineering,* vol. 96, no. 1, pp. 37-43, 2014.

[15] S. C. Kaushik, S. S. Verma and A. Chandra, "Solar-assisted liquid metal MHD power generation: A state of the art study," *Heat Recovery Systems and CHP,* vol. 15, no. 7, pp. 675-689, 1995.

[16] E. S. Pierson and H. Herman, "Solar-powered liquid-metal MHD performance and cost studies," in *Proceedings of the Third Beer-Sheva International Seminar on Magnetohydrodynamic Flow and Turbulence*, Beer-Sheva, 1981.

[17] W. Fietz and C. Rosner, "Advances in superconductive magnets and materials," *IEEE Transactions on Magnetics,* vol. 10, no. 2, pp. 239-259, 1974.

[18] J. Gieras, "Permanent magnet materials and circuits," in *Permanent magnet motor technology*, Boca Raton, CRC Press, Taylor & Francis Group, 2010, pp. 45-58.

[19] R. R. Miller and R. Lyon, "Physical properties of liquid metals," in *Liquid-Metals Handbook*, University Microfilms International, 1978, pp. 40-48.

[20] ASM Handbook Committee, "Metals Handbook, Volume 2 Properties and Selection: Nonferrous Alloys and Pure Metals, Ohio: American Society for Metals, 1978.

[21] Chemical Rubber Company, "Properties of solids," in *Handbook of chemistry and physics*, Boca Raton, CRC Press, Taylor & Francis Group, 2014, pp. 12-41-45.

[22] H. Branover, A. El-Boher, A. Yakhot and S. Claesson, "An operating model of two-phase heavy-metal MHD power systems," in *Proceedings of the Third Beer-Sheva International Seminar on Magnetohydrodynamic Flow and Turbulence*, Beer-Sheva, 1981.

[23] Y. Fujii-e, K. Miyazaki, S. Inoue and N. Yamaoka, "Experimental studies on liquid-metal two-phase MHD flow in traveling and dc magnetic fields," in *Proceedings of the Third Beer-Sheva International Seminar on Magnetohydrodynamic Flow and Turbulence*, Beer-Sheva, 1981.

[24] E. Cosoroaba and B. Fahimi, "Temperature dependence of efficiency in renewable magnetohydrodynamic power generation systems," in *IEEE Energy Conversion Congress and Exposition (ECCE)*, Milwaukee, 2016.

[25] L. S. Frost, "Conductivity of seeded atmospheric pressure plasma," *Journal of applied physics,* vol. 32, no. 10, pp. 2029-2036, October 1961.

[26] R. Hawley, "Magnetohydrodynamic power generation," *Journal of the Institution Electrical Engineers,* vol. 7, no. 83, pp. 667-669, 1961.

[27] Y. Deng and J. Liu, "Corrosion development between liquid gallium and four typical metal substrates used in chip cooling device," *Applied Physics Material Science & Processing,* vol. 95, no. 3, pp. 907-915, 2009.

[28] N. Bogoevici and D. Toader, "Câmpul Electromagnetic," in *Bazele Electrotehnicii, Teorie şi Aplicaţii*, Timişoara, Editura Politehnica Timişoara, 2010, pp. 200-208.

[29] H. H. Woodson, "AC power generation with transverse-current magnetohydrodynamic conduction machines," *IEEE Transactions on Power Apparatus and Systems,* vol. 84, no. 11, pp. 1066-1072, 1965.

[30] M. J. Duggin, "The thermal conductivity of liquid gallium," *Physics Letters,* vol. 29A, no. 8, pp. 470-471, 1969.

[31] A. J. Chapman, "Fluid Mechanical Aspects of Forced Convection," in *Fundamentals of Heat Transfer*, New York, Macmillan Publishing Company, 1987, pp. 244-255.

[32] A. Fischer, C. L. d'Elia Machado, L. E. Brito de Almeida and A. and Beluco, "Energetic potential and variability of ocean currents on the sourhtern coast of Brazil," *IEEE Latin America Transations,* vol. 13, no. 5, pp. 1369-1375, 2015.

[33] I. Kolin, S. Koscak-Kolin and M. Golub, "Geothermal electricity production by means of the low temperature difference Stirling engine," in *World Geothermal Congress Proceedings*, Kyushu, 2000.

[34] M. He, N. Beutler, D. Loeder and S. Sanders, "Testing of 2.5 kW low temperature Stirling engine for distributed solar thermal generation," in *Energytech*, Cleveland, 2012.

[35] BCS, Incorporated, "Waste heat Revovery: Technology and Opportunities in U.S. Industry," 2008.

BIOGRAPHICAL SKETCH

Eva-Marie Cosoroabă was born in 1990 in Orăştie, spending most of her youth in Sibiu, Romania. She attended the German-language high school "Samuel von Brukenthal" with a focus on natural sciences starting fall of 2005. She then earned her Baccalaureate and enrolled at the Universitatea Politehnică Timişoara for a degree in Electrical Engineering in 2009. During her time at UPT she participated in several internship programs, in and outside of Romania, at multinational companies such as Continental Automotive and Bosch Solar Energy. She received her Bachelor of Science and Engineer title in 2013, with her thesis "The Double Stator Switched Reluctance Machine: Electromagnetic Studies and Controlled Dynamics," work guided by Dr. Ion Boldea. Eva continued her education the same year, starting the PhD program in Electrical Engineering at The University of Texas at Dallas, Richardson, USA. At this time she also became a research assistant at the Renewable Energy and Vehicular Technology Laboratory. She furthermore held multiple teaching assistant positions throughout these years and discovered her passion for engineering education. She earned the Graduate Teaching Certificate in 2016 and her PhD in Electrical Engineering in 2017, with the dissertation "Multiphysics Simulation, Analysis, and Design of a Permanent Magnet Excited Liquid Metal Magnetohydrodynamic Power Generator," under the guidance of Dr. Babak Fahimi. Ms. Cosoroabă has authored and co-authored six journal and magazine publications and eleven conference papers so far.

<div align="center">

CURRICULULM VITAE

Eva-Marie Cosoroabă

</div>

Address: 800 West Campbell Rd., EC33, Richardson, Texas 75080
Email: exc131430@utdallas.edu

EDUCATION HISTORY

- **Doctor of Philosophy, Electrical Engineering,** The University of Texas at Dallas, Richardson, TX, December 2017

- **Graduate Teaching Certificate,** The University of Texas at Dallas, Richardson, TX, December 2016

- **Bachelor of Science, Electrical Engineering,** Universitatea Politehnică Timişoara, Timişoara, Romania, June 2013

- **Baccalaureate,** The "Samuel von Brukenthal" High School, Sibiu, Romania, June 2009

- **German Language Certification,** The Education Ministers Conference, Sibiu, Romania, May 2009

WORK EXPERIENCE

- **Teaching and Research Assistant,** The University of Texas at Dallas, Richardson, TX, August 2013 to December 2017

- **Intern,** Intelligent Buildings, Timişoara, Romania, July to August 2012

- **Engineering Intern,** Bosch Solar Energy AG, Arnstadt, Germany, June to October 2011

- **Engineering Intern,** Continental Automotive, Sibiu, Romania, July to September 2010

- **Visitor Guide,** Lutheran Church of Cisnădie, Romania, May 2006 to September 2008

PUBLICATIONS

- M. Wu, J. Pacheco, **E. Cosoroaba**, and B. Fahimi, "Multiphysics simulation of pulsed cold plasma arc rotation for enhanced hydrogen harvesting" *International Journal of Hydrogen Energy,* accepted for publication September 2017

- Y. Li, L. Maharjan, **E. Cosoroaba**, and B. Fahimi, "Comparative study of a new coil design with traditional shielded figure-of-eight coil for transcranial magnetic stimulation," *IEEE Transactions on Magnetics,* accepted for publication September 2017

- **E. Cosoroaba**, E. Bostanci, Y. Li, and B. Fahimi, "Comparison of winding configurations on double stator switched reluctance machines," *IET Electric Power Applications,* accepted for publication May 2017

- W. Cai, F. Yi, **E. Cosoroaba**, and B. Fahimi, "Stability optimization method based on virtual resistor and nonunity voltage feedback loop for cascaded DC–DC converters," *IEEE Transactions on Industry Applications*, vol. 51, issue 6, December 2015

- **E. Cosoroaba**, "Five reasons why you should attend conferences as a student," *IEEE Potentials,* vol. 34, issue 3, June 2015

- W. Wang, M. Luo, **E. Cosoroaba**, B. Fahimi, and M. Kiani, "Rotor shape investigation and optimization of double stator switched reluctance machine," *IEEE Transactions on Magnetics,* vol. 51, issue 3, March 2015

- Y. Li, **E. Cosoroaba**, and B. Fahimi, "Comparative study of a new coil design with traditional shielded figure-of-eight coil for transcranial magnetic stimulation," *Compumag,* Daejeon, Korea, June 2017

- S. Jayasankar, L. Maharjan, **E. Cosoroaba**, E. Bostanci, and B. Fahimi, "On the proximity effects of high-energy magnets on M-19 magnetic steel core," *IEEE International Electric Machines & Drives Conference, IEMDC,* Miami, May 2017

- **E. Cosoroaba** and B. Fahimi, "Magnetohydrodynamics in thermal to electric energy conversion," *The 17th Biennial Conference on Electromagnetic Field Computation, IEEE CEFC,* Miami, November 2016

- E. Bostanci, L. Gu, **E. Cosoroaba**, M. Moallem, and B. Fahimi, "Performance improvement and comparison of concentrated winding segmental rotor and double stator switched reluctance machines," *The 17th Biennial Conference on Electromagnetic Field Computation, IEEE CEFC,* Miami, November 2016

- **E. Cosoroaba** and B. Fahimi, "Temperature dependence of efficiency in renewable magnetohydrodynamic power generation systems," *IEEE Energy Conversion Congress & Expo, ECCE,* Milwaukie, September 2016

- **E. Cosoroaba** and M. Wu, "Magnetohydrodynamic power generation – a renewable, emission free energy solution," *MMM-Intermag Joint Conference,* San Diego, January 2016

- M. Wu and **E. Cosoroaba**, "Electromagnetic valves via volumetric energy conversion," *MMM-Intermag Joint Conference*, San Diego, January 2016

- L. Gu, D. Patil, and **E. Cosoroaba**, "Core loss estimation of SPMSM based on field reconstruction method," *18th International Conference on Electrical Machines and Systems, ICEMS,* Thailand, October 2015

- **E. Cosoroaba** and B. Fahimi, "Efficiency oriented design guidelines for a magnetohydrodynamic generator system," *IEEE International Electric Machines & Drives Conference, IEMDC,* Coeur d'Alene, May 2015

- W. Cai, F. Yi**, E. Cosoroaba**, and B. Fahimi, "Stability analysis and voltage control method based on virtual resistor and proportional voltage feedback loop for cascaded DC-DC converters," *IEEE Energy Conversion Congress & Expo, ECCE,* Pittsburgh, September 2014

- **E. Cosoroaba**, W. Wang, and B. Fahimi, "Comparative study of two winding configurations for a double stator switched reluctance machine," *21st International Conference on Electrical Machines, ICEM,* Germany, September 2014

HONORS AND AWARDS

- Merit Scholarship of Universitatea Politehnică Timişoara, 2009-2013

LANGUAGES

- German

- Romanian

- English

PROFESSIONAL MEMBERSHIPS

- Institute of Electrical and Electronics Engineers (IEEE)

- IEEE Young Professionals

- IEEE Women in Engineering

- IEEE Education Society

- American Society for Engineering Education (ASEE)